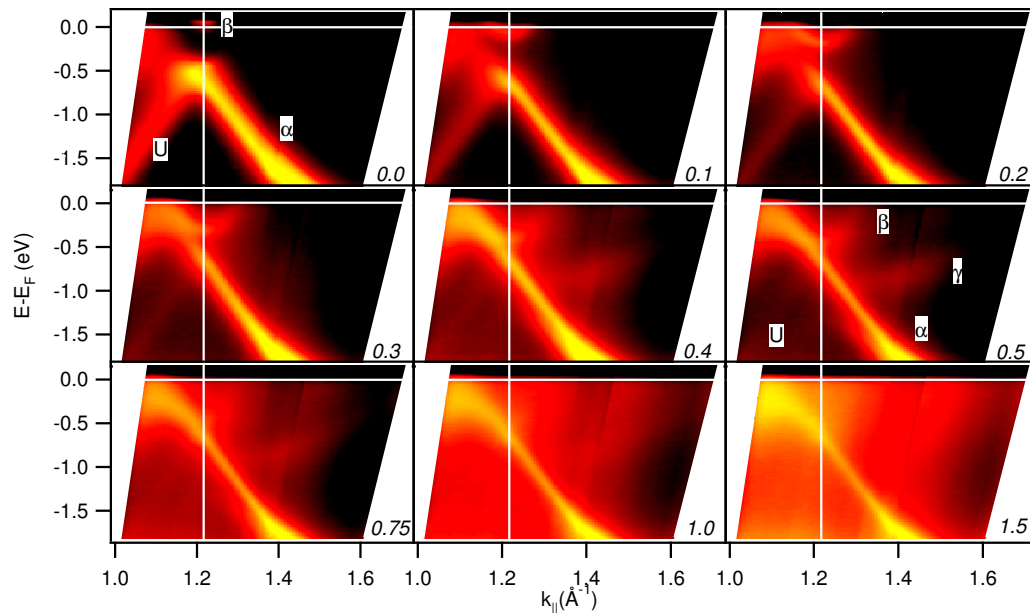


Two dimensional magnetic surface compounds: The $c(2 \times 2)$ Mn-induced superstructures on the fcc-(001) surfaces of Cu, Fe, Co, and Ni



Dissertation

zur Erlangung des akademischen Grades

Doktor rerum naturalium

(Dr. rer. nat)

vorgelegt von

Frederik Schiller

geboren am 21. 10. 1971 in Zwickau/Sachsen

Institut für Oberflächen- und Mikrostrukturphysik

Fachrichtung Physik

Fakultät Mathematik und Naturwissenschaften

Technische Universität Dresden

2001

1. Gutachter: Prof. Dr. C. Laubschat
2. Gutachter: Prof. Dr. W.-D. Schneider
3. Gutachter: Prof. Dr. E. García Michel

Tag des Einreichens der Arbeit: 25. Oktober 2001

Kurzfassung

In der vorliegenden Dissertation werden die elektronischen Eigenschaften der $c(2\times 2)$ MnCu/Cu(001) Oberfläche untersucht. Es wird eine Möglichkeit vorgestellt, unter Nutzung verschiedener Symmetrien der Brillouinzonen, Photoemissionsspektren voneinander zu trennen und damit die energetische Position des Majoritätsspinbandes von Mangan in der $c(2\times 2)$ Überstruktur zu bestimmen. Es konnte mittels Vergleich zu Rechnungen der Bandstruktur außerdem festgestellt werden, daß Teile des Minoritätsspinbandes besetzt werden. Die Fermioberfläche des $c(2\times 2)$ MnCu/Cu(001) Systems wurde mittels Photoemission untersucht. Es konnte weiterhin gezeigt werden, daß Kupfer epitaktisch auf dieser Oberfläche aufwächst und weitere $c(2\times 2)$ MnCu Sequenzen gewachsen werden können, wobei sich auch hier die Manganatome in einem magnetischen Grundzustand befinden. Es wird das Wachstum von Mangan auf Eisen, Kobalt und Nickel analysiert. Dafür werden dünne Eisen-, Kobalt- und Nickelschichten auf einem Kupfer-(001)-Einkristall präpariert und damit eine metastabile flächenzentrierte Oberfläche geschaffen, die wiederum als Substrat für das Mangan dient. Alle diese Zwischenschritte werden von Untersuchungen der elektronischen Eigenschaften mittels Photoemissionsmessungen begleitet, die dazu dienen, Aussagen über die Bandstruktur und die Fermi-Oberfläche zu erhalten. Diese experimentellen Daten werden anschließend mit theoretisch berechneten Daten verglichen und daraus Schlußfolgerungen für den Magnetismus in den einzelnen Systemen getroffen.

Abstract

This thesis deals about the electronic properties of the $c(2\times 2)$ MnCu/Cu(001) surface. Under use of different symmetries in the Brillouin zones, a possibility for the separation of photoemission spectra is presented and the energy position of the manganese spin majority band is determined. Furthermore, a comparison with theoretic studies found part of the spin minority band occupied. The Fermi surface of the $c(2\times 2)$ MnCu/Cu(001) system was analysed. It could be shown, that copper grows epitaxially on top of this surface and a further growth of $c(2\times 2)$ MnCu sequences is possible with the manganese atoms in a high spin ground state.

Further, the growth of manganese on iron, cobalt, and nickel will be investigated. For this purpose thin iron, cobalt, and nickel films are prepared on a copper-(001) crystal and the resulting metastable face centred surface can be used as a substrate for the manganese. All these intermediate steps are accompanied by investigations of the electronic properties using photoemission, that give an insight in the band structure and the Fermi surface. The experimental data will be compared to theory and some conclusions about the magnetism of the systems can be drawn.

Contents

Kurzfassung/Abstract	3
Introduction	9
1 Experimental details	11
1.1 Scienta 200 spectrometer	11
1.2 Experimental techniques	12
1.2.1 Principles of valence band photoemission	13
1.2.2 Photoelectron diffraction	18
1.2.3 X-ray absorption	19
1.2.4 Low energy electron diffraction	20
2 Photoemission experiments of Cu(001)	23
2.1 Reasons for measurements	23
2.2 Photoemission experiments on the Cu(001) surface: bulk states .	23
2.2.1 Results and their interpretation	23
2.2.2 Umklapp processes	30
2.2.3 Polarisation effects	33
2.3 Surface states at Cu(001)	34
2.3.1 Aim of the study	34
2.3.2 Surface states in the Shockley-inverted bulk gaps: the Cu(001) \bar{X} surface state	36
2.3.3 Cu(001) Tamm surface state near \bar{M}	40
2.3.4 Results of calculation of photoemission spectra	42
2.4 Fermi surface investigations	42
2.5 Conclusions	49
3 Majority and minority states in $c(2\times 2)$MnCu/Cu(001) measured by photoemission	51
3.1 Introduction	51
3.2 Band structure analysis of $c(2\times 2)$ MnCu	52
3.2.1 Photoemission measurements of $c(2\times 2)$ MnCu	52
3.2.2 LKKR-based photoemission calculation of the $c(2\times 2)$ MnCu/Cu(001) surface compound	52

3.2.3	Method for the determination of the Mn spin majority band	54
3.2.4	Mn-induced magnetic surface states near the $\bar{X}_{p(1\times 1)}$ point	60
3.2.5	Quenching of the Cu(001) Tamm state upon Mn deposition	68
3.3	Fermi-surface changes after formation of the $c(2\times 2)$ structure	69
3.4	Conclusions	72
4	Growth and magnetic properties of Mn/Cu multilayers	73
4.1	Aim of study of Mn/Cu multilayers	73
4.2	Synthesis of MnCu/Cu Multilayers	73
4.2.1	Growth of Cu on $c(2\times 2)$ MnCu/Cu(001)	73
4.2.2	Mn-Cu multilayers	78
4.3	Magnetism of the system	78
4.4	Photoemission results	80
4.4.1	Core-level photoemission	80
4.4.2	Valence-band photoemission	84
4.4.3	Fermi surface analysis	87
4.5	Conclusions	90
5	The electronic structure of Mn overlayers on ferromagnetic films of Fe, Co, and Ni epitaxially grown on Cu(001)	91
5.1	Synthesis of the fcc-(001) surfaces	91
5.1.1	Fe/Cu(001)	91
5.1.2	Co/Cu(001)	94
5.1.3	Ni/Cu(001)	95
5.2	Manganese exposure to the pseudomorphic grown ferromagnetic fcc Fe, Co, and Ni thin films: spin majority bands	96
5.2.1	Theoretical considerations	96
5.2.2	Growth and structure of Mn on the ferromagnetic fcc (001) surfaces of Fe, Co, and Ni metal	98
5.2.3	Electronic structure of 0.5 ML manganese deposited on the fcc (001) surfaces of Fe, Co, and Ni	102
5.3	Fermi surface investigations for pseudomorphic grown $c(2\times 2)$ Mn/-X/Cu(001) structures (X=Fe, Co, Ni)	109
5.3.1	$c(2\times 2)$ Mn/Fe/Cu(001)	110
5.3.2	$c(2\times 2)$ MnCo/Cu(001)	113
5.3.3	$c(2\times 2)$ MnNi/Ni/Cu(001) and MnNi/Ni(001)	117
6	Summary and Outlook	121
A	The Mn/Cu(001) overlayer system	123
A.1	Manganese	123
A.2	The Mn/Cu system	124
A.2.1	Historical remarks about the Mn/Cu compounds	124
A.2.2	Investigations in the Mn/Cu surface structure	124

A.2.3	Experimental results from literature	125
A.3	The $c(2\times 2)$ CuMn/Cu(001) surface alloy	125
	Bibliography	129
	Acknowledgements	141
	Curriculum vitae	145

Introduction

Magnetism is one of the most prospering fields in modern physics. The high demand of the industry for stronger magnets is only one field. Another reason of the scientific activity arises from the fact that the information technology (IT) branch has to store the strongly increasing data volume in the same geometrical dimensions as before. While 5 years ago a normal computer hard disc could store about 500 Mbyte, nowadays this amounts 50 Gbyte in less geometric space. This extreme increase is based on several new inventions developed by fundamental research in the last years. The reading device is built up from magnetic multilayer systems using the giant magnetoresistance (GMR) effect. Examples for such materials are Cr/Fe or Co/Cu. The GMR effect is based on a large decrease in electrical resistivity that occurs when the magnetisation of two layered samples is aligned by an external magnetic field. In an easy model on the contact between a magnetic and a nonmagnetic material, e.g. Co and Cu, exist an equal number of, e.g., spin up electrons but a different number of spin down electrons. When, in the case of Co/Cu, the cobalt layers are ferromagnetically aligned by an external field, spin up electrons can travel through the copper layer as the potentials are very similar. Spin down electrons, however, are scattered at the interphase. An antiferromagnetic alignment of the cobalt layers, on the other hand, scatter both spin sort electrons and the resistivity increases strongly. This model is, however, too simple to understand all effects involved in GMR, a better understanding could lead to the development of increased data storage density on magnetic disk drives and nonvolatile thin film magnetic storage devices for computer operating memory (RAM) whose data would not be destroyed by ionising radiation or power outages. Electronic properties, that cause the effect, give inside into the physical processes that occur on the interphase and will be studied in the present work. The key making the new type of memory work efficiently is the deposition of high-quality magnetic films of a specified thickness carried out here for several overlayer systems.

One aspect is how to read and write from a computer hard disc, another important point is the material itself. The ferromagnetic material that is used up to now uses several 10000 atoms per bit. If one can establish materials that decrease this storage density to atomic scale, data volume of some orders of magnitude higher can be stored in the same place. One of the promising candidates in the recent years for this task was the $c(2\times 2)\text{MnCu}$ surface compound structure that

is formed, when half a monolayer of manganese is deposited on a Cu(001) surface leading to a MnCu surface compound of a checkerboard structure. Since the Mn-Mn distances are increased with respect to their bulk distances, the Mn atom can carry a high magnetic moment - magnetism at atomic scale. Reason for the magnetism is the electronic structure of the surface compound that was studied in detail in the present work. The aim of the work was to elucidate how the Mn electrons interact with the surrounding copper atoms, and what is the final electronic structure of the whole system. The work was extended in two directions, *(i)*: the $c(2\times 2)$ MnCu surface compound would be exposed to environmental conditions such as contamination of the surface by reactive gases. A protection of the compound layer by another copper overlayer would passivate the system, but what happens with the magnetic and electronic properties? Furthermore, if it would be possible to grow a second compound layer on top, coupling between the two magnetic layers can be expected and can then be used for further application like the GMR materials. *(ii)*: Surface compounds may be stabilised on a magnetic substrate. If such $c(2\times 2)$ surface compounds could be established, how would the Mn atoms interact with the surrounding magnetic material? Would it be possible to build new magnetic materials based on two-dimensional surface compounds?

The main experimental method used during this work is photoemission spectroscopy that first has been applied to pure Cu(001) where some new results have been obtained. The present work focuses particularly on aspects that are related to the later measured $c(2\times 2)$ MnX systems for X=Cu, Fe, Co, and Ni. Methods include angle resolved photoemission spectroscopy and Fermi surface analysis based on the same technique. If possible, the results are compared to theoretic investigations. Other experimental methods such as photoelectron diffraction, low energy electron diffraction and soft X-ray absorption are explained only very shortly. In the following the $c(2\times 2)$ MnCu/Cu(001) system was studied in detail and compared to literature results and layered Korringa-Kohn-Rostoker photoemission calculations that can be used to interpret the obtained results. The same methods are then used for the other $c(2\times 2)$ surface compounds formed on ferromagnetic thin films. Here, for the first time the $c(2\times 2)$ Mn/Fe/Cu(001) structure was observed and characterised. It was tried to search for similarities or differences in the investigated systems by comparing the results. Finally some basic conclusions are drawn and an outlook is given for further investigations in these and similar systems.

Chapter 1

Experimental details

1.1 Scienta 200 spectrometer

As most of the work was done with a Scienta 200 spectrometer, this experimental station shall be described briefly. Fig. 1.1 shows the hemispherical electron

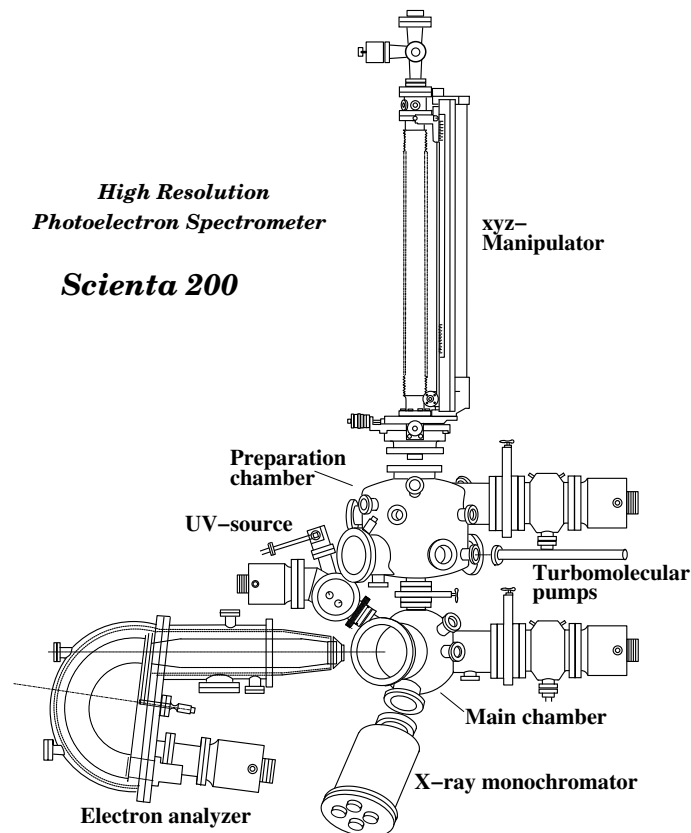


Figure 1.1: Scienta 200 spectrometer as used in most of the experiments.

energy-analyser that is connected to a μ -metal chamber. Such a μ -metal chamber is used to protect the analysing system from external magnetic fields that would deviate the electrons on their way to the analyser. The sample is transferred from the preparation chamber into the μ -metal chamber by means of a 6-axes sample

manipulator. When the sample is in the measuring position it can be either illuminated by X-rays or ultraviolet light. The X-ray tube emits mainly Al K_α light that is further monochromatised allowing an overall system resolution of approx. 400 meV (FWHM) at a pass energy of 75 eV. Ultraviolet light is emitted from a microwave supported gas discharge lamp (Gammadata VUV 5000) and then monochromatised by a toroidal grating monochromator (TGM) optimised in the energy range between 20 and 40 eV to discriminate different discrete lines of the noble gas (here: He) spectrum. Particularly due to the large exit slit that was used to increase photon flux the resolution of the monochromator was restricted to approx. 1 eV in this energy range. This value is derived from the fact that HeI β ($h\nu=23.1$ eV) and HeI δ ($h\nu=24.1$ eV) light could be monitored at the same time. In contrast to conventional analysers the Scienta 200 is equipped with a position-sensitive detector consisting of a channelplate, a fluorescence screen and a video-camera that allow parallel recording of electrons emitted with different energies in different directions. The large radius of the hemisphere assures high electron transmission, and a highly stabilised spectrometer control electronics allows electron-energy resolution down to 5 meV. The sample manipulator was specially designed for this spectrometer and was built in the IFW Dresden. On the manipulator, 6 axes can be moved, 3 translations (x, y, and z) and 3 rotations (polar, azimuthal, and tilt angle). Computer-controlled stepper-motors manoeuvre the rotation axes achieving a highly accurate sample positioning with an adjustment precision better than 0.5°. The sample can be cooled down to 25 K by a helium cryostat. A specially designed flapping mechanism can separate the sample from the manipulator in order to heat samples up to 2000°C in cleaning process, if necessary.

These details characterise this spectrometer as one of the world leading devices. As an example: with conventional analysers a Fermi surface mapping that includes measurement at approx. 3000 \vec{k} points takes usually about 6 hours. Applying a Scienta 200 analyser this time can be reduced to approx. 1 hour with the advantage of clean surfaces and less cleaning cycles.

The sample is prepared in the preparation chamber that is equipped with a four grid LEED optics, micro-quartz balances, sample cleaning facilities such as ion gun and heating station. The sample can be inserted into the chamber by a fast entry lock system to prevent the chamber from bake-outs. The sample is transferred by a linear transfer mechanism directly to the main manipulator.

1.2 Experimental techniques

The main experimental technique used during this study is photoemission spectroscopy that will be described in the following and is probed on the Cu(001) surface in the next chapter. Further experimental techniques used are photoelectron diffraction, X-ray absorption, and low energy electron diffraction.

1.2.1 Principles of valence band photoemission

Photoemission

The photoemission technique (photoemission spectroscopy [PE or PES]) is based on the photoelectric effect discovered by HERTZ in 1887 [Her87] and explained by EINSTEIN in 1905 [Ein05]. The process is schematically described in Fig. 1.2. Absorption of a photon of energy $h\nu$ leads to emission of an electron with the

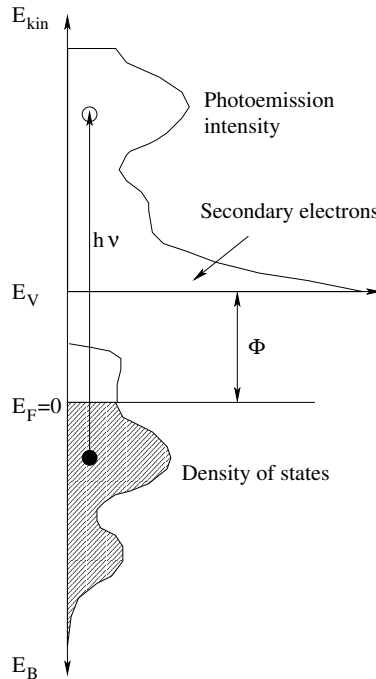


Figure 1.2: Schematic description of photoelectron spectroscopy.

kinetic energy E_{kin} , which is given by

$$E_{kin} = h\nu - E_B - \Phi \quad (1.1)$$

where E_B denotes the binding energy and Φ the work function of the material. Emission from energetically lower lying levels is usually called core level photoemission and requires photons of higher energies (X-ray photoemission spectroscopy [XPS]), valence band emission is also observed at lower photon energies (ultraviolet photoemission [UPS]). As the binding energies of the core levels differ for the elements the XPS technique is also called electron spectroscopy for chemical analysis [ESCA] and can be used to determine the chemical composition of samples. Further overall description of the technique is given, e.g., in [Hüf96, Zan92].

The binding energy E_B is the difference of the total energies E_i and E_f of the initial $|\psi_i\rangle$ and final $|\psi_f\rangle$ state, where the initial state is given by a N -electron and the final state by a $(N-1)$ -electron system. Assuming that the removal of an electron does not affect the energies of the remaining states (frozen-orbital-approximation) allows a direct interpretation of binding energies in terms of

single-particle energies that are, e.g., obtained as results from band-structure calculations. In valence-band photoemission, the presence of conduction electrons leads usually to an effective screening of the potential of the photohole, so that the “frozen-orbital-approximation” is fulfilled and PE may be used for band structure mapping. For localised states, however, the hole potential cannot be screened completely by the valence electrons and the atomic system relaxes. In this case E_B can no longer be identified with a single-particle energy, but the whole many-body-problem has to be considered properly.

Valence band photoemission

For an infinite solid the transition probability of a PE process w is proportional to:

$$w(E_f, \vec{k}_f) \propto \int_{E_f} \int_{\vec{k}_f} |M|^2 \cdot \delta(E_f - E_i - h\nu) \cdot \delta(\vec{k}_f - \vec{k}_i - \vec{k}_{ph}). \quad (1.2)$$

Hereby, the two δ -functions ensure energy and momentum conservation. $\vec{k}_{i,f}$ denote the wave vectors in the initial and final state, $h\nu$ and \vec{k}_{ph} energy and wave vector of the photon while M denotes the matrix-element

$$M \propto \langle \psi_i | \vec{A}\hat{p} + \hat{p}\vec{A} | \psi_f \rangle \quad (1.3)$$

where \vec{A} represents the vector potential of the electromagnetic wave and \hat{p} the electron momentum-operator. Taking $\vec{A} \propto \vec{A}_0 \cdot \exp(i\vec{k}\vec{r})$ with $|\vec{k}_{ph}| \ll 1/d$, where d represents the atomic radius, $|\vec{A}|$ is almost constant and $\vec{A}\hat{p} + \hat{p}\vec{A}$ becomes proportional to the dipole-operator \vec{r} .

The wave-functions $|\psi_{i,f}\rangle$ are represented in an infinite solid by Bloch-functions. In the more realistic case of a semi-infinite solid $|\psi_{i,f}\rangle$ may be described by Bloch-waves inside the material that couple to an exponential decay or free electron state in the vacuum region, respectively. Since the translation symmetry perpendicular to the surface is broken, $\vec{k} = \vec{k}_{\parallel} + \vec{k}_{\perp}$ is no longer a good quantum number since \vec{k}_{\perp} changes upon transition through the surface¹.

For many applications, however, this so called “one-step” model of PE is too complicated and, therefore, replaced by the “three-step” model, where the PE process is artificially divided into three subprocesses, namely (i) photoexcitation within an (quasi-) infinite solid, (ii) transport through the solid, and (iii) transmission through the surface. With $|\vec{k}_{ph}| \ll \pi/a$, where a denotes the lattice constant, follows $\vec{k}_f \sim \vec{k}_i$ and step (i) is described by vertical interband transitions. The finite lifetime of the photohole leads to Lorentzian-lineshapes in the spectra that may become asymmetrically broadened if electron-hole-pair excitations are taken

¹For parts of the present work $w(E_f, \vec{k}_f)$ has directly be calculated by means of a LKKR approach, where particularly $|\psi_f\rangle$ is described by a time-reversed LEED wave function and both real structure and diffraction effects are considered.

into account. Step (ii) includes inelastic processes within the transport that are related to the small mean-free path of the excited electrons in the solid (see Fig. 1.3 for the inelastic mean free path in bulk materials) and are responsible for

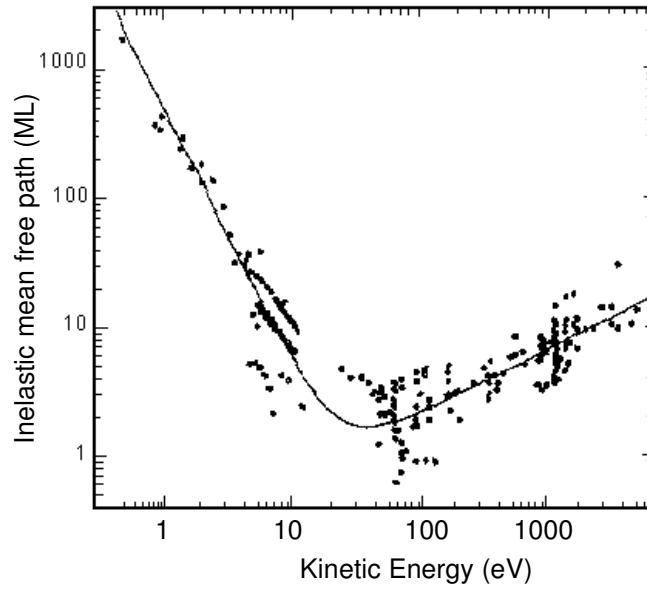


Figure 1.3: Inelastic mean free path in monolayers (ML) of electrons in bulk materials [Den79].

the background of inelastically scattered electrons in the spectra. Assuming that the probability of an energy loss ΔE is independent from the magnitude of ΔE if $\Delta E \ll E_{kin}$ leads to a background, that is proportional to the integral of the ideal spectral function. Step (iii) describes the relation between the wave vectors \vec{k}_f inside the solid and \vec{k}'_f measured in the vacuum in analogy to the well-known phenomenon of refraction in optics. Fig. 1.4 sketches the refraction of the wave

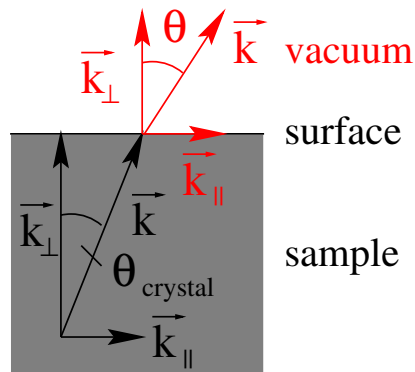


Figure 1.4: Refraction of the wave leaving the solid: the wave vector parallel to the surface is unchanged, while the perpendicular component shrinks. The angle of detection θ is, therefore, larger than $\theta_{crystal}$ in the solid.

vector at the surface. The wave vector parallel to the surface remains unchanged:

$$\vec{k}_{\parallel,crystal} = \vec{k}_{\parallel,vacuum}, \quad (1.4)$$

while the perpendicular component of \vec{k} becomes smaller in the vacuum.

Inside the crystal the momentum-energy relation

$$E_{crystal} = \frac{\hbar^2(\vec{k}_{crystal} - \vec{G})^2}{2m_{eff}} = E_{vacuum} + V_0 \quad (1.5)$$

can be applied where \vec{G} denotes a reciprocal lattice vector, V_0 the inner crystal potential, and m_{eff} the effective mass of the electron. The reciprocal lattice vector \vec{G} is necessary in (1.5), since the solutions of the Schrödinger equation are not only valid in the first but also in higher order Brillouin zones. The effective mass of the electron contains the bonding of the electron to the atoms inside the solid. Considering only solutions in the First Brillouin zone ($\vec{G}=0$)² and a separation of the wave vector $\vec{k}=\vec{k}_{\parallel}+\vec{k}_{\perp}$ in its parallel and perpendicular component transform (1.5) in

$$\frac{\hbar^2 k_{\perp,crystal}^2}{2m_{eff}} + \frac{\hbar^2 k_{\parallel,crystal}^2}{2m_{eff}} = \frac{\hbar^2 k_{\perp,vacuum}^2}{2m} + \frac{\hbar^2 k_{\parallel,vacuum}^2}{2m} + V_0. \quad (1.6)$$

Here, the momentum-energy relation $E_{vacuum} = \hbar^2 k_{vacuum}^2/2m$ was included. This inclusion is the free electron final state approximation, that is not always valid for the final state of the electron³. Together with (1.4) and the approximation of $m=m_{eff}$, (1.5) yields

$$\frac{\hbar^2 k_{\perp,crystal}^2}{2m} = \frac{\hbar^2 k_{\perp,vacuum}^2}{2m} + V_0. \quad (1.7)$$

In the experiment, however, only the intensity-energy distribution and the emission angles are detectable. The angles involved in the photoemission transition of an angle resolved experiment are sketched in Fig. 1.5. They can be changed depending on the experimental setup either by the movement of the analyser or a rotation of the sample manipulator. The parallel component of the wave vector derived from (1.4) is hence:

$$k_{\parallel,crystal}^2 = k_{\parallel,vacuum}^2 = \frac{2m}{\hbar^2} \cdot E_{vacuum} \cdot \sin^2 \theta, \quad (1.8)$$

and can be calculated using the values of the natural constants as

$$\vec{k}_{\parallel,crystal} [\text{Å}^{-1}] = 0.512 \cdot \sqrt{E_{vacuum} [eV]} \cdot \sin \theta \cdot \begin{pmatrix} \cos \varphi \\ \sin \varphi \end{pmatrix}. \quad (1.9)$$

²Later, it will shown that an inclusion of \vec{G} yield to additional solutions of the Schrödinger equation, the *umklapp-processes*.

³A more appropriate approximation is to use the final states from band structure calculations, however, interpretation is much more complicated.

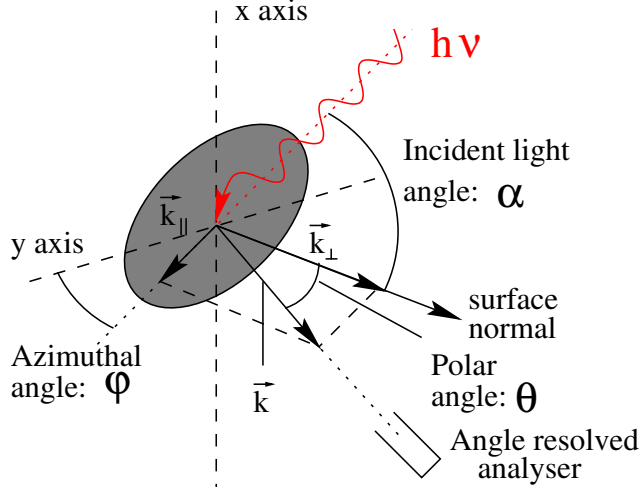


Figure 1.5: Angles involved in a photoemission experiment.

The perpendicular component is expressed by

$$k_{\perp,crystal}^2 = \frac{2m}{\hbar^2} \cdot (E_{vacuum} \cdot \cos^2 \theta + V_0) \quad (1.10)$$

or again using the the values of the natural constants to

$$k_{\perp,crystal} [\text{\AA}^{-1}] = 0.512 \cdot \sqrt{E_{vacuum} [eV] \cdot \cos^2 \theta + V_0 [eV]}. \quad (1.11)$$

The solution of the energy- \vec{k} relation is therefore the surface of a sphere with the radius $k_{crystal}$ originated in $\sqrt{2m/\hbar^2} \cdot (E_{vacuum} + V_0)$, depending on the vacuum energy E_{vacuum} . That in turn is related to the photon energy by

$$E_{vacuum} = h\nu - E_i - \Phi. \quad (1.12)$$

It should be mentioned again that the equations given above for the wave vector perpendicular to the surface are only valid considering free electron final states, whereas those for the parallel component are universally valid. To obtain better approximation of k_{\perp} values more complicated studies involving non-free final states may be used. A more detailed description of experimental methods of determining \vec{k} is given in [Cou84].

The surface terminates the periodic lattice of the material and the crystal potential originating from the atoms leading to a potential step at the surface of solids. Solutions of the Schrödinger equation for such a potential are called surface states and usually occur in energy regions, where bulk band states are forbidden. They are predominantly localised within the outermost atomic surface layer and the amplitudes of their wave functions decrease into the bulk. Due to this property k_{\perp} of these states is zero and the dispersive behaviour of these states can exactly be determined by means of photoemission. A more detailed description of surface states in the case of the Cu(001) surface will be given in the next section.

Two main experimental geometries are used for band-mapping by means of photoemission. The first are measurements in normal emission geometry ($\vec{k}_{\parallel} = 0$).

Such experiments are usually restricted to be performed at synchrotron radiation facilities since the photon energy must be tuned. However, under laboratory conditions there exists also the possibility for such kind of measurements using discharge lamps operating with different gases providing respective light emission lines, that can be separated by a monochromator⁴. The second geometry for angle resolved photoemission that works with constant photon energy and variation of the emission angle easily can be carried out in laboratory.

1.2.2 Photoelectron diffraction

Photoelectron diffraction [PED] is a tool to analyse the crystallographic structure of a material. While low energy electron diffraction is used to determine the long range order (see section 1.2.4), PED gives information about the short range order in the material. Scattering of emitted photoelectrons by neighbouring atoms leads to interference effects that can be monitored by recording *photoemission intensities* at constant emission angle as a function of photon energy or at a constant photon energy as a function of the emission angle. At high kinetic energies of the photoelectrons ($E_{kin} > 400$ eV), PED is dominated by single-scattering processes in forward direction (see Fig. 1.6 [WE90]) so that intensity maxima in the angular photoelectron distribution may directly be related to the relative positions of atomic neighbours. For lower kinetic energies (back

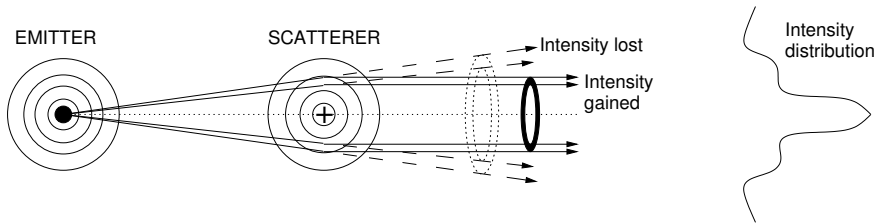


Figure 1.6: Schematic diagram of the semiclassical model indicating the forward scattering caused by the attractive ion core potential [WE90].

scattering mode) multiple scattering processes have to be considered that make the interpretation of PED data more complicated. The usual way to analyse the data is a trial and error procedure where for a supposed structure multiple scattering is simulated and the results are compared to the experiment. An optimal fit is obtained by varying the structural parameters. The advantage of low kinetic energy photoelectron diffraction in a back scattering mode is that information about bond distances and ad-atom locations may be derived that are difficult to obtain by other methods. Further information about photoelectron and the related Auger electron diffraction can be found in [WE90, Cha91, Fad90].

⁴In the present work only He light was used with its respective lines HeI α =21.2 eV, HeI β =23.1 eV, HeI γ =23.7 eV, HeI δ =24.1 eV; and HeII α =40.8 eV, HeII β =48.4 eV, HeII γ =51.0 eV, HeII δ =52.2 eV. Note that the intensity decreases strongly for the β to δ lines. The photon energies and typical intensities at the sample are compiled together in [Sie82].

1.2.3 X-ray absorption

Photon absorption is related to electron excitation from occupied to unoccupied states, particularly to photoionisation of certain core states. These absorption processes can be monitored as jumps in the absorption versus energy curve indicated in Fig. 1.7. The phenomenon may simply be visualised by monitoring the

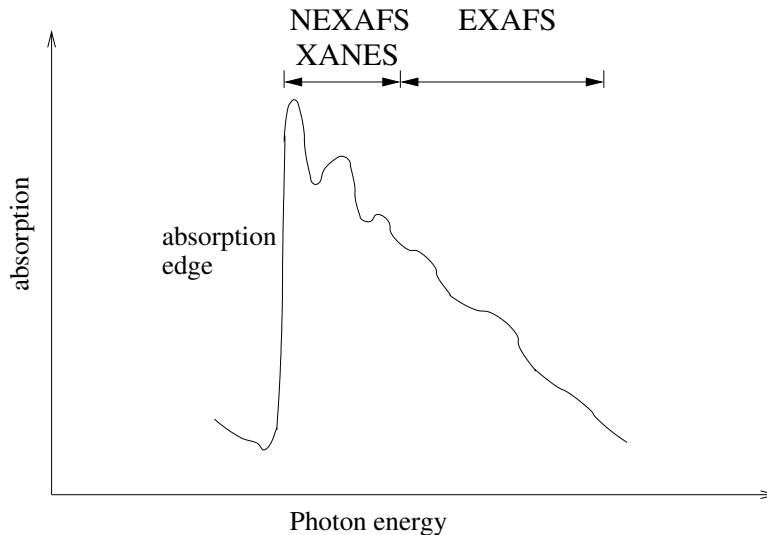


Figure 1.7: Typical absorption spectra of a solid; the distinct energy regions with their names are given.

total electron yield emitted from the sample as a function of photon energy that is proportional to the photoionisation cross-section. Peaks or step-like features in the total-yield spectra indicate the energy position of the respective absorption edges, oscillating intensity variations behind the edge (i.e., at higher photon energies) are caused by diffraction of the excited electrons by scattering from neighbouring atoms. The spectrum is, therefore, usually divided into two main areas: the structures up to several 10 eV above the absorption edge are called near edge X-ray absorption fine structure (NEXAFS, XANES), and at higher energy extended X-ray absorption fine structure (EXAFS). While the EXAFS region gives information about interatomic distances, NEXAFS may provide information about chemical bonding (e.g. density of states). Here we will concentrate only on the NEXAFS part of the spectrum.

In a first approximation a one-electron model may be considered, where relaxations of the electronic system upon core-hole creation are neglected. In this model the absorption coefficient is proportional to the photoionisation cross-section and can be expressed by

$$\mu(E) \propto |\langle \psi_f | \vec{r} | \psi_i \rangle|^2, \quad (1.13)$$

where $\langle \psi_f | \vec{r} | \psi_i \rangle$ denotes the dipole transition matrix element between initial $|\psi_i\rangle$ and final $|\psi_f\rangle$ states. Therefore the dipole selection rules of the orbital

(l), the magnetic (m_l), the spin (m_s) and the total magnetic quantum number (j) have to be fulfilled:

$$\Delta l = \pm 1; \left\{ \begin{array}{c} \Delta m_l \\ \Delta j \\ \Delta m_j \end{array} \right\} = \left\{ \begin{array}{c} -1 \\ 0 \\ +1 \end{array} \right\}; \Delta m_s = 0. \quad (1.14)$$

For example, for a $2p$ state two transitions are possible: A transition ($\Delta l = +1$) into the $3d$ band and into the $4s$ band ($\Delta l = -1$). Transitions into the $3d$ band, however, have 98% probability, whereas for the $4s$ level only a probability of 2% is obtained [Hea77]. A $2p \rightarrow 3d$ transition ($L_{2,3}$) results in a doublet peak dominated by the dipole transition from the $2p_{3/2}$ and $2p_{1/2}$ core level into an empty $3d$ state that is energetically lowered under the influence of the core hole. Since both the initial and the final states are strongly localised at the atomic site, the transition process depends critically on the local electronic structure. Deviation from the statistical intensity relation of 1:2 for the $2p_{1/2}$ - and $2p_{3/2}$ -derived features is mainly due to local magnetic moments. The intensity relation is found to be larger than the statistical value for a high-spin ground state [Tob92].

1.2.4 Low energy electron diffraction

One of the most frequently used techniques for structure determination in surface science is low energy electron diffraction [LEED]. A focused and accelerated electron beam is elastically scattered at the sample surface. The back scattered electrons interfere and yield maxima and minima in the intensity distribution that can be visualised on a fluorescent screen. If multiple-scattering is neglected, the resulting intensity distribution is the Fourier transform of the real surface lattice. Positions of high intensity are attributed to lattice points of the reciprocal lattice. Treating the surface as an ideal two-dimensional lattice, the Ewald construction for diffraction in the reciprocal lattice of bulk materials (see e.g., [Kit85]) is still valid, if a transformation of the reciprocal lattice points into rods perpendicular to the surface is considered. The intersection of Ewald's sphere with the rods defines the directions, where intensity maxima are observed. The limitation of electron interaction to the outermost atomic surface layer is, however, only an approximation. Depending on their energies electrons can penetrate deeper into the solid. The universal curve shown in Fig. 1.3 is valid for electron interaction with solids and, hence, also valid for LEED. Since the electrons stem partly from the bulk, it is not possible to observe an ideal Fourier transform of only the surface lattice, but bulk diffraction of the electrons also contributes to the signal. Variation in the (ideally constant) spot intensity as a function of electron energy is the consequence that may be described within the Ewald construction by an intensity modulation of the "rods" (see Fig. 1.8). These variations are used to analyse atomic positions perpendicular to the surface (the technique is then named dynamic LEED or I-V-LEED).

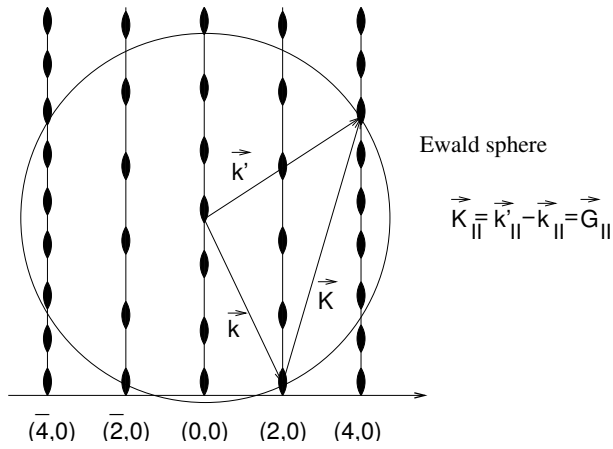


Figure 1.8: Ewald construction of a 2 dimensional lattice.

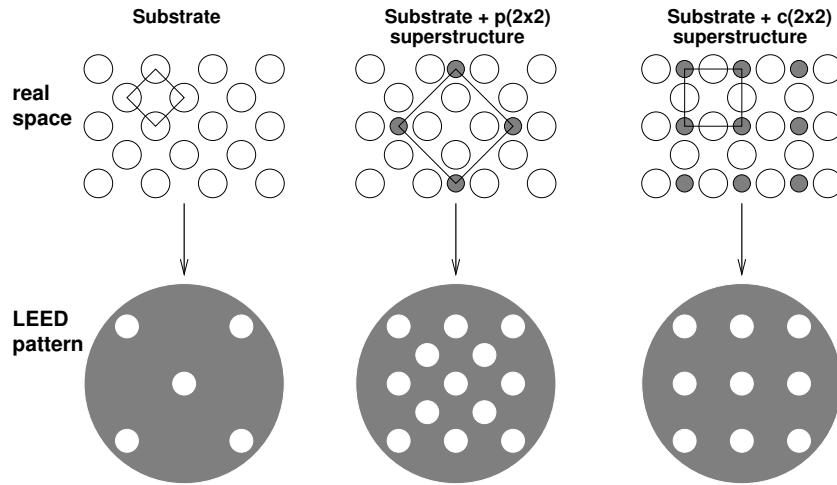


Figure 1.9: Some superstructures and the corresponding LEED patterns: $p(1 \times 1)$, $p(2 \times 2)$, and $c(2 \times 2)$.

Even without consideration of these effects, a simple LEED pattern provides useful information about the surface lattice and LEED is, therefore, widely used in surface science. Some LEED patterns that were observed during this work are illustrated in Fig. 1.9⁵.

⁵The name of the superstructures is the multiple of the superstructure in respect to the underlying substrate in the substrate lattice directions. (p) signifies a primitive, while (c) a centred unit cell.

Chapter 2

Photoemission experiments of Cu(001)

2.1 Reasons for measurements

Copper is one of the best studied materials by photoemission spectroscopy¹. From this point of view the question arises why again measurements have been performed on clean Cu? Cu is the substrate for the surface compounds considered in the present work, and in order to understand the electronic properties of the latter it is necessary to see how the electronic structure of the Cu substrate is modified by Mn adsorption. This demands angle-resolved PE with identical experimental conditions that cannot be found in literature. Additionally, the principles of photoemission and limits of the method will be given in this chapter.

Copper is a fcc metal with the electronic configuration [Ar] $3d^{10}4s^1$. The d band is nearly full, so the d bands shift away from the Fermi level and are found between 2 eV and 5 eV binding energies. The band formed by the s electron (due to its band hybridisation called the sp band) disperses stronger than the d bands and is responsible for the Fermi surface formation.

2.2 Photoemission experiments on the Cu(001) surface: bulk states

2.2.1 Results and their interpretation

As it is possible to calculate the \vec{k} vector inside the solid using the methods described in the last chapter, measurements at specified points in the 3 dimensional (3-D) Brillouin zone (BZ) of a material can be performed. Fig. 2.1 shows, which \vec{k} points can be reached using different photon energies and polar and azimuthal angles taken as an example the Cu(001) surface in the ΓXWK ([01] or $\bar{\Gamma}\bar{M}$

¹See, for example, COURTHS and HÜFNER [Cou84] about earlier results up to 1984.

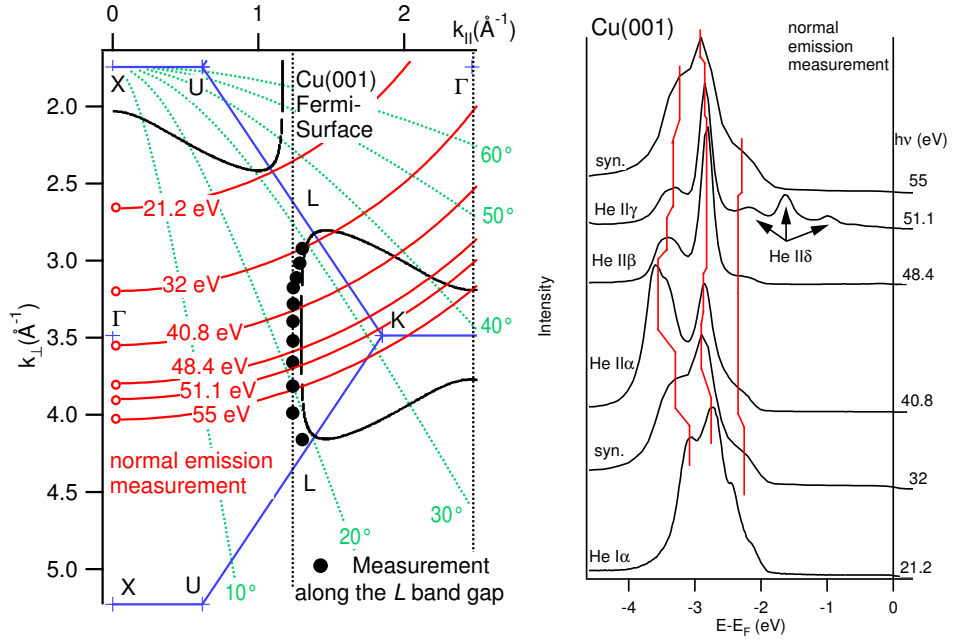


Figure 2.2: Constant k_{\parallel} measurement of Cu(001). Left hand side: visualisation of the measured \vec{k} region for two different experiments: measurement along normal emission (open circles) and for constant k_{\parallel} but with different photon energies and emission angles along $L-L$ in the L band gap (solid circles), right hand side: Normal emission spectra were taken at different photon energies with synchrotron radiation ($h\nu=32$ eV, 55 eV) and a He lamp ($h\nu=21.2$ eV, 40.8 eV, 48.4 eV, 51.1 eV) source. The spectrum measured at $h\nu=51.1$ eV (He II γ) contains also a contribution from He II δ ($h\nu=52.2$ eV) that could not be suppressed due to the finite resolution of the monochromator in this range of photon energies.

states in this \vec{k} region and reveal usually much less pronounced signals. There is a weak dispersion for three main peaks, that can be used to map the band dispersion. Note, that all spectra except the ones at $h\nu=32$ eV and 55 eV were taken by means of a laboratory source. The spectra at $h\nu=32$ eV and 55 eV were taken with synchrotron radiation and appear broadened as compared to the laboratory data. This is mainly due to the monochromator resolution of the SU6 beamline of LURE, where these spectra were acquired, that is much worse than the line width of the gas source.

Measurements along other directions in the Brillouin zone that are perpendicular to the surface but characterised by $\vec{k}_{\parallel} \neq 0$ require a simultaneous change of the photon energy and the emission angle. As an example Fig. 2.2 indicates the \vec{k} positions along $L-L$ in the L band gap (solid circles). This measurement is interesting mainly by two reasons: (i): for the study of a surface state that is situated in the band gap and (ii): to study the copper sp band that crosses here the Fermi edge. Corresponding photoemission results are displayed in Fig. 2.3. All spectra were taken at the TGM 3 beam line at the synchrotron radiation facility BESSY I

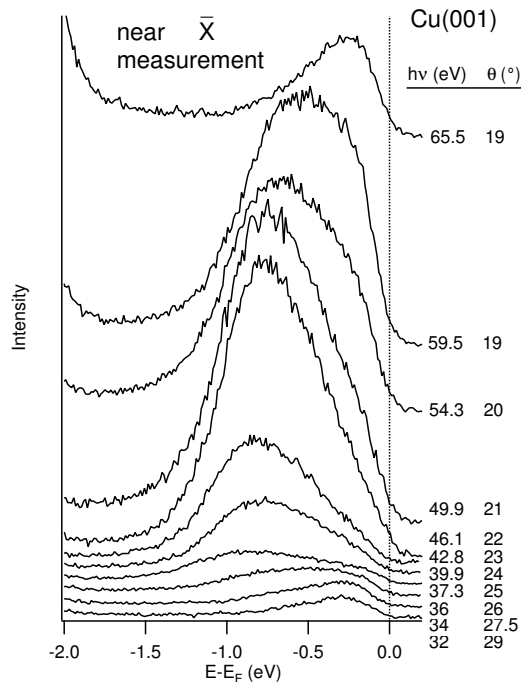


Figure 2.3: Photoemission measurement along $L-L$ in the L band gap (perpendicular to the \bar{X} point). The peak corresponds to the copper sp that crosses here the Fermi edge. The Shockley surface state is not resolved in the experiment.

in Berlin. The spectra were normalised to the emission intensity above the Fermi energy. Here, the signals originate from higher order monochromatised light and are nearly proportional to the photon flux. As seen in Fig. 2.3 the signal of the monitored band is largest at photon energies between 46 and 50 eV and decreases strongly both at higher and lower photon energies. There are several reasons for this intensity variation. First of all the angular momentum character of the band changes: the often used notation as the copper sp band is slightly misleading at least for the spectra shown here in this figure. In most parts of the Brillouin zone the sp band has mainly d character near the Fermi edge. A LCAO calculation (linear combination of atomic orbitals) along the $L-L$ direction where the measurements were carried out, reveal that at the L point the band has 100% of p character. On half way from L to L (at the crossing with the ΓK or Σ direction), however, it reveals 70% of d , 15% of s , and 15% of p character. The cross-section for the $3d$ wave function at the photon energies used is approx. two orders of magnitude higher than for the $4s$ wave functions. Therefore, almost exclusively the d contribution is observed being mainly responsible for the obtained intensity variation.

Another reason for such drastic changes in intensity may be related to crystal symmetry selection rules for optical interband transitions at the individual points of the Brillouin zone that depend on light polarisation. Allowed and forbidden transitions between bands of different symmetries are published in tables

that can be found in [Ebe80] compiled by EBERHARDT and HIMPSEL for fcc and bcc lattices. For the present case, the symmetry of the bands can be derived from band structure calculations, e.g., those published by PAPACONSTANTOPOULOS [Pap85]. The band considered here has a $L_{2'}$ symmetry. In the D_{3d} symmetry group, to which the L point belongs, two possible transitions for $L_{2'}$: $L_{2'} \rightarrow L_1$ and $L_{2'} \rightarrow L_3$ are allowed depending on the polarisation of the light. However, since the L_1 is spherically symmetric the transition should be observed for any polarisation and cannot be the reason for the intensity decrease near the L point seen in the spectra.

Since most of the experiments of this work were carried out in the laboratory, we will focus on laboratory results in the following. The data of a typical laboratory angle resolved photoemission measurement on Cu(001) for several emission angles along the [10] and [11] high symmetry directions are given in Fig. 2.4. For each emission angle PE spectra were taken in the binding energy range from 0 to 7 eV. Several bands are seen that disperse as a function of the emission angle. From (1.9) the k_{\parallel} -energy dispersion relation can be calculated and then compared to results of band structure calculations in order to analyse the character of the bands. Results of band structure calculations published in literature are usually restricted to high symmetry directions and, therefore, not very suitable for comparison with experiments performed with constant photon energy by varying the emission angles. Therefore, in the framework of the present work new calculations have been performed in order to derive the energy eigenvalues just for those \vec{k} -points that were sampled by the experiment. As already mentioned, the problem consists in a correct determination of k_{\perp} that depends on the form of the final state assumed. Usually, the final-state dispersion is approximated by free electron like parabola. This assumption, however, is not justified in all \vec{k} points. Particularly, close to Brillouin-zone boundaries derivations from this simple approximation may be expected.

In this work several programs for the band structure calculations were used: a linear combination of atomic orbitals program (LCAO) originated from RICHTER and ESCHRIG [Ric89], a full-potential nonorthogonal local-orbital minimum-basis band-structure scheme (FPLO) developed by KOEPERNIK and ESCHRIG [Koe99], as well as a tight binding approximation (TB) written by PAPACONSTANTOPOULOS [Pap85]. Further theoretical approach used in this work is based on the layered Korringa-Kohn-Rostoker method (LKKR) that in contrast to the former mentioned band structure programs treats the final state as non-free electron like and will be discussed in section 3.2.2. Fig. 2.5 compares the experimental dispersion relation with two conventional band structure approaches: LCAO and tight binding theories calculate bands in a perfect infinite crystal, not considering the surface. Photoemission as the used experimental tool to measure this band structure, on the other hand, is a very surface sensitive method often sampling only the first few atomic layers of a sample. Nevertheless the used theoretical models are well suited as first approximations for explaining the experimental

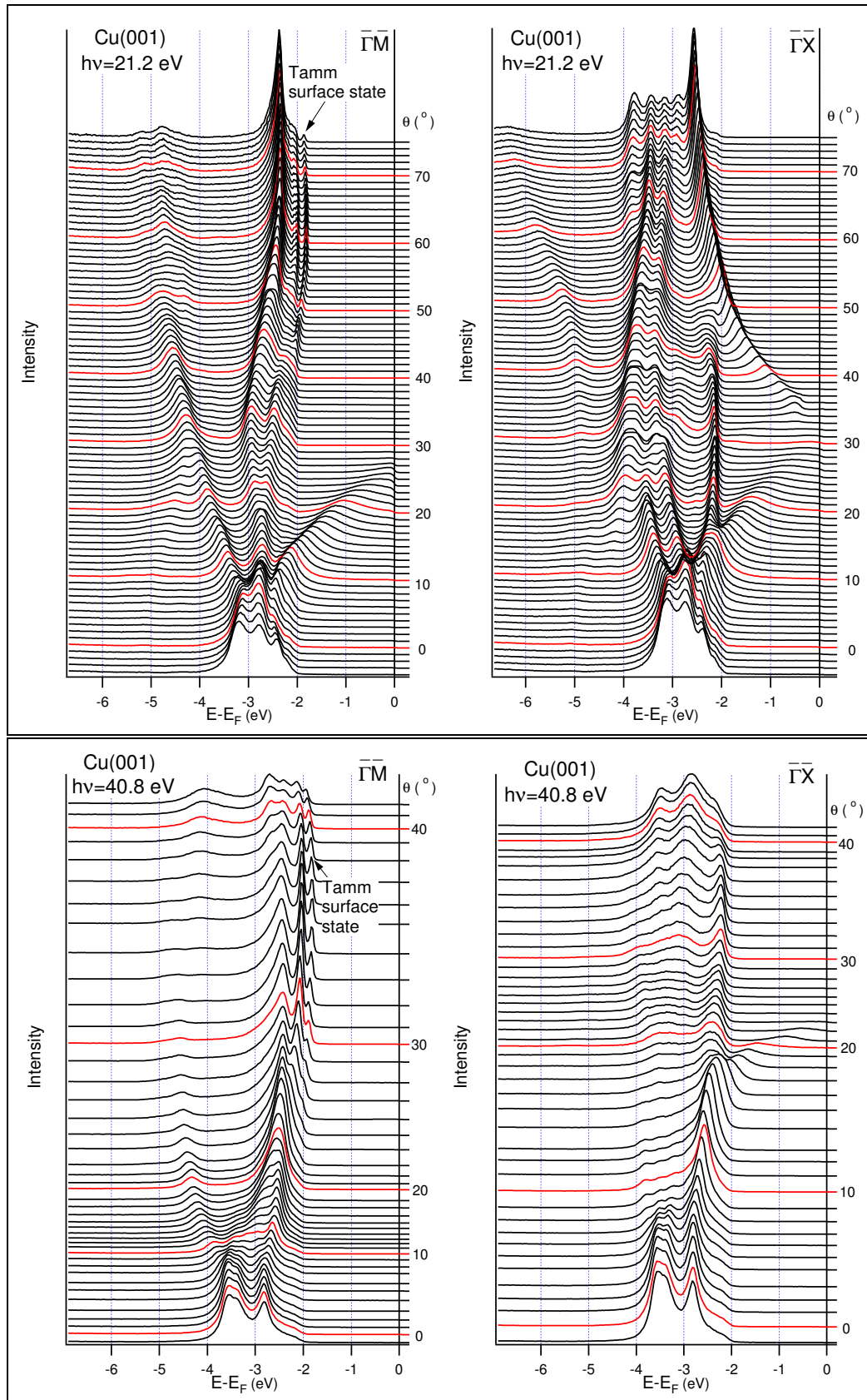


Figure 2.4: Angle resolved photoemission spectra taken with a constant photon energy of 21.2 eV (top) and 40.8 eV (bottom) for the two high symmetry directions of the surface Brillouin zone $[01]=\bar{\Gamma}\bar{M}$ (left) and $[11]=\bar{\Gamma}\bar{X}$ directions (right), respectively.

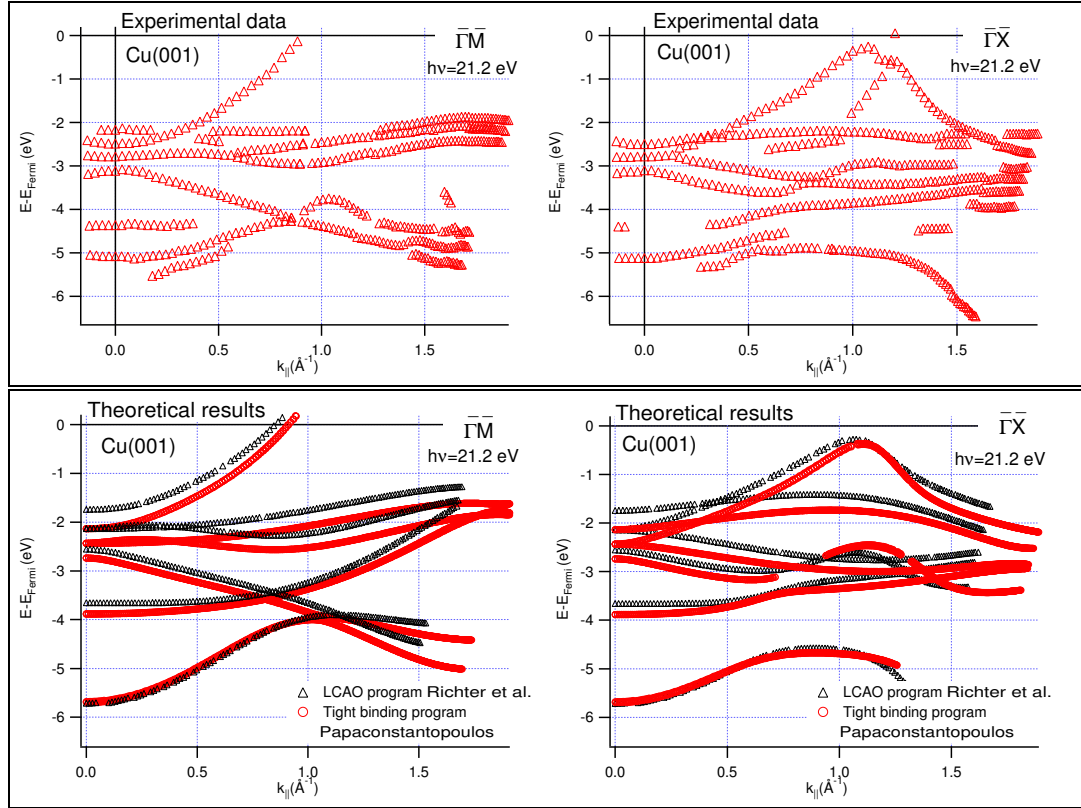


Figure 2.5: Experimental (top) and theoretical (bottom) dispersion relations for the two high symmetry directions of the Cu(001) surface. The theoretical bands were calculated using the LCAO approach by RICHTER and ESCHRIG [Ric89], the tight binding approach by PAPACONSTANTOPOULOS [Pap85].

dispersion relation. The general form of the dispersion relations obtained in the experiment and by the theory is similar (Fig. 2.5). The strong dispersing bands are the so-called copper *sp* bands, that have a nearly free electron like behaviour. The weak dispersing bands are the copper *d* bands originating from atomic *d* orbitals. These orbitals are tightly bound to the atom cores what leads to a large effective electron mass and, consequently, a weaker dispersion than the *sp* ones. In the $\bar{\Gamma}\bar{X}$ direction of the surface Brillouin zone (SBZ) the copper *sp* band disperses toward the Fermi level, but does not cross it. This is due to fact that the \vec{k} -point reached with this photon energy lies inside the band gap around the *L*-point that is related to the Fermi surface bridges between the Brillouin zones in the ΓL directions, causing the famous “dog bone” shape of the noble metal Fermi surfaces. A more detailed comparison, however, reveals small differences between theory and experiment: *(i)*: For some bands calculated and experimental energy positions are different, *(ii)*: Some obtained bands by the calculation are not observed in the experiment, and *(iii)*: There exist features in the experiment that are not seen in the theory. There exist several reasons to explain the first point: the already mentioned final state problem, slight shifts due to the surface potential, and calculation details like cut-off radii or compression radii.

All above parameters could be adjusted to the experiment but this was not done here. Another effect is related to the final-state screening: upon photoemission an energy-hole state is created that becomes screened electrostatically by valence electrons. In the spatial distribution of the screening charge differs from the one of the emitted photoelectron. The atom hole relaxes resulting in an energy shift- usually to higher binding energies- in the PE spectrum. As to the second point, photoemission intensities depend on symmetry and angular momentum character of the states, polarisation of the radiation and other parameters. For example, in the experiment with linear polarised light used with synchrotron radiation states of different symmetries can be excited upon variation of the angle of incidence of light. In this way some bands will appear with lower, others with higher intensities. Apart from polarisation effects, cross-section values of the excitation differ strongly for distinct parts of the valence band. For example, the copper valence band is formed by the $3d$ and the $4s$ electrons. For a photon energy of 21.2 eV, that was used in the laboratory experiments, these cross-section differences amount a factor of nearly 200³. Furthermore, there exist crystal symmetry selection rules when measuring in high symmetry directions of single crystalline solids that have to be taken into account [Her77, Ebe80].

Concerning the appearance of more features in the experiment than predicted by the theory, there are mainly two reasons possible: (*i*): at the Cu(001) surface exist several surface states seen in photoemission, (*ii*): reciprocal lattice vectors \vec{G} are involved in the photoemission process leading to so called umklapp processes. The intensity of these umklapp processes is usually lower than that of a direct transition. The determination of the umklapp processes combines k_{\perp} and \vec{k}_{\parallel} making it complicated to give an explicit form of the dispersion relation. However, if \vec{G} is known, such umklapp processes can be considered. An example of such an umklapp process is given in the next section, while the surface states will be discussed in detail afterwards.

2.2.2 Umklapp processes

Umklapp processes are not very well studied in the literature. The main reasons are the already mentioned dependence of k_{\perp} and \vec{k}_{\parallel} from each other and probably also the weak intensity of the relating signals. Although there exist several umklapp features in the spectra shown in Fig. 2.4, here we will focus only one feature that is located close to the Brillouin zone boundary near the L point. Fig. 2.6 shows the copper sp bands near the L point. Apart from the strong intensity variation that is due to the proximity to the high symmetry point L and the crystal symmetry selection rules for such points [Ebe80, Him78], three

³Cross-section values are calculated usually for atoms (YEH and LINDAU [Yeh85]) but are often used also in solid-state physics. The behaviour of the cross-sections in the solid state and the atomic case is, however, different (see, e.g., [Mol00] for cross-section measurements and their comparison to theory).

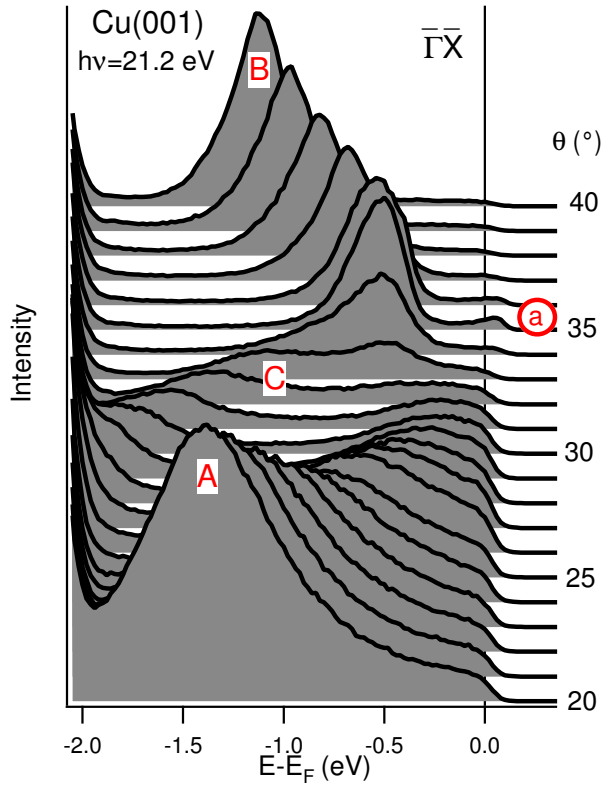


Figure 2.6: Photoemission spectra of Cu(001) along the $\bar{\Gamma}\bar{X}$ high symmetry direction near the L point measured with a photon energy of 21.2 eV.

main features can be distinguished, in the spectra labelled A , B , and C . The broad feature A splits off the main branch of the d bands at about 15° dispersing toward the Fermi level. At around 30° emission angle it becomes very low in intensity at about 250 meV binding energy. A similar dispersive behaviour is observed for feature C . This feature, however, is less intense and split off the d bands at 28° . The third feature, B , disperses to higher binding energies with its intensity growing when leaving the high symmetry point L . A fourth weak feature labelled a is the Shockley type surface state and will be described in the next section. While features A and B were already reported previously [Hei79, Dur81], the band C was theoretically expected, but still not observed [Dur81]. DURHAM and KAR calculated the solutions for different initial states (Fermi energy, E_F ; binding energies 0.6, 1.3, and 2.0 eV [$E_{0.6}$, $E_{1.3}$, and $E_{2.0}$], respectively) throughout the Brillouin zone as seen in Fig. 2.7 [Dur81]. The possible final states, E' , for the corresponding energies $E + \hbar\nu$ are also shown in the figure. The final state contours were derived from a free-electron fit adjusted to the bottom of the lowest lying valence band (Δ_1 band along ΓX direction). This procedure leads not only to the final states shown already in Fig. 2.1, but also to additional final states shifted by reciprocal lattice vectors \vec{G} (here $\vec{G} = [112]$) from the Brillouin zone of higher orders giving rise to umklapp processes. The crossing points of the initial and final state curves of the same energies are the possible solutions causing bands

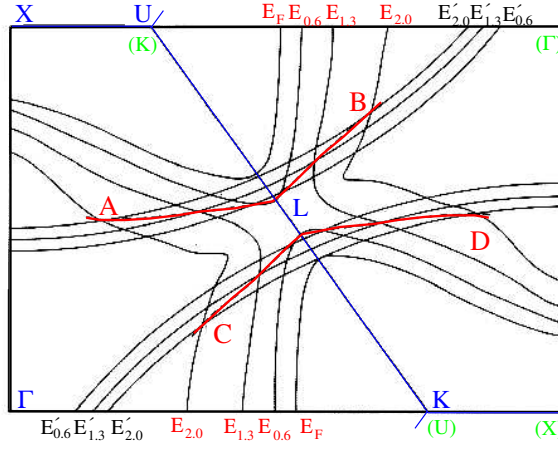


Figure 2.7: Possible initial states E_F , $E_{0.6}$, $E_{1.3}$, and $E_{2.0}$ for the photoemission process near the L point at Cu(001). The corresponding final states are depicted by circular arcs E'_F , $E'_{0.6}$, $E'_{1.3}$, and $E'_{2.0}$. The crossings are the possible solutions seen in the photoemission experiment, which are marked by lines connecting A-B and C-D. To obtain the final states for the labels C and D, a reciprocal lattice vector had to be involved ($\vec{G}=[112]$) to produce the umklapp transition process (Fig. taken from ref. [Dur81]).

seen in photoemission. These solutions are indicated by the lines connecting A-B and C-D. The final state for the energy corresponding to the Fermi energy was not included in the graphics, because the initial state is too far away from the possible final states to produce a crossing. This is consistent with the fact, that near the L point there exists a Shockley-inverted band gap and normal bulk bands are forbidden within this energy- \vec{k} region. The calculated variation of the final state energies with the emission angle as well as the corresponding experimental data taken from [Dur81] and the data measured in the present work are shown in Fig. 2.8. Discrepancies between the two sets of experimental data seen for the curve labelled A are probably due to some alignment errors. Here, the alignment process was done directly by measurements of photoemission spectra on the sample varying the polar emission angle with a step of $\Delta\theta=0.5^\circ$. The error is, therefore, less than 1° . DURHAM and KAR [Dur81] performed photocurrent calculations, the results of which are also included in the figure. It can be noted that the experimental data and both theoretic approaches are in good agreement with each other. The signals A and B are much more intense due to the matrix elements involved in the transition process (direct transitions). The photocurrent calculations show a less intense feature C but no D [Dur81]. The different spectral width of features A and B is explained by differences in life time of the corresponding excited states [Dur81].

⁴Alignment process as follows: (i) alignment to the LEED pattern, (ii) photoemission alignment: searching for symmetric dispersion around $\bar{\Gamma}$ (polar angle), and (iii) around \bar{X} (Shockley surface state) and \bar{M} (Tamm surface state) (azimuthal angle).

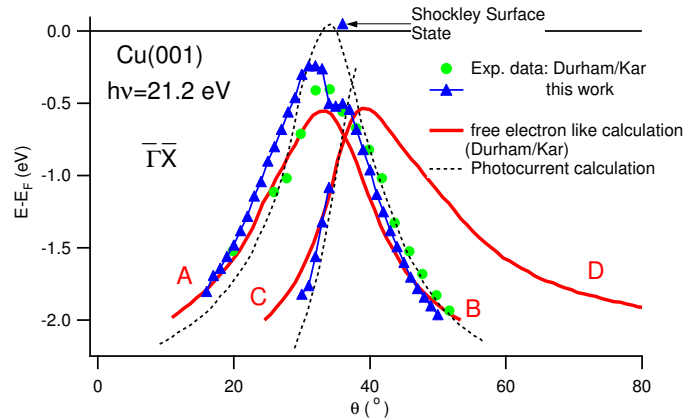


Figure 2.8: Dispersion along the $\bar{\Gamma}\bar{X}$ direction at Cu(001) measured with $h\nu=21.2$ eV. The theoretical curves are derived from Fig. 2.7. Also included is the photocurrent calculation from [Dur81]. While in the experiment DURHAM and KAR do not find evidence for the umklapp derived feature C, its existence is confirmed by the data measured in the present work.

2.2.3 Polarisation effects

Light from laboratory ultraviolet sources is usually “unpolarised”, in the sense that the polarisation vector has no preferable direction. Synchrotron radiation, on the other hand, is usually a mixture of s and p linearly polarised light⁵. The standard example for the use of the different light polarisation is the study of chemisorbed CO on a Ni(001) surface [Smi76]. Depending on the angle between the surface normal \vec{n} and the polarisation vector, σ or π orbitals are emphasised and the binding geometry of the CO molecule (lying or upright) can be obtained. The same effect can be applied to different atomic orbitals. The s orbital for example has a spheric symmetry and does not feel influence of the polarisation vector. On the other hand, to emphasise $d_{xy,yz}$ states, the electric field vector \vec{E} should be entirely in the surface plane while d_{z^2} are emphasised for $\vec{E} \parallel \vec{n}$. Since most results of this work are measured using conventional laboratory light sources, polarisation effects might be important, since a grating monochromator is used in these experiments. After diffraction by the grating the component of the electric vector that is perpendicular to the grating surface is suppressed with respect to the parallel component⁶. In optics, full polarisation can be achieved when the BREWSTER condition for the incidence angle $\tan \alpha = n_1/n_2$ for photons in a medium with the refractive index n_1 that are reflected at the boundary with another medium with n_2 is fulfilled. In the present work the polarisation effect induced by diffraction results in an p -polarisation that is two times higher

⁵Circular polarised light can be provided by specially designed beamlines that give users the possibility to study magnetic structures in details.

⁶The diffraction and reflection angles are very similar, therefore, it is possible to consider only the angle of incidence reflection α that is equal to the angle between the outgoing wave and the surface normal (Snell’s law).

than s polarisation. The corresponding effect on the spectra is displayed in Fig. 2.9. Since the Scienta 200 analyser can simultaneously measure with angular

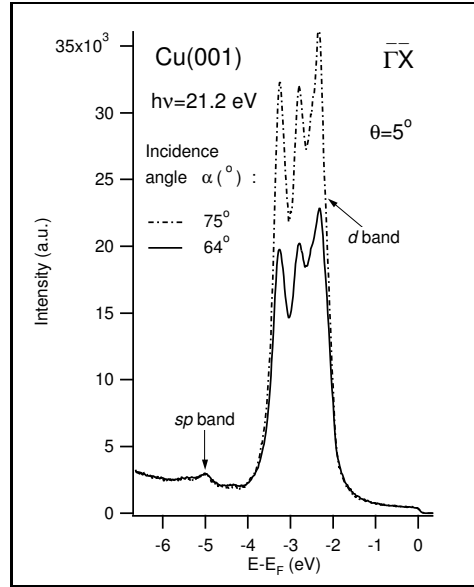


Figure 2.9: Polarisation effects for the $\theta=5^\circ$ off-normal spectrum upon variation of the incident angle α (measurement along $\bar{\Gamma}\bar{X}$ with a photon energy of 21.2 eV).

resolution in a window of polar angles up to 14° the following analysis is possible: Both spectra were measured at $+5^\circ$ off-normal emission. For this purpose the angle between the surface normal and the analyser was adjusted to 0 and 10° corresponding to a change of incidence angle from 75 to 64° , respectively. The total shape of the spectra is almost unchanged. While there is no effect for the almost spherically symmetric sp orbitals that also form the Fermi surface at higher emission angles, the d bands (e.g., $d_{xy,yz}$ and d_{z^2} geometry) with non-spherical symmetry are strongly affected. Peak positions remain constant as the \vec{k} point of the measurement is the same. This effect has two main consequences, (i): discrimination between band symmetries is possible and (ii): measurements, where the intensity distribution is important (constant energy scans such as Fermi surface investigations) can be strongly influenced by polarisation effects. A Fermi surface cut, for example, can be measured using the 14° polar angle window of the analyser that speeds up the measurement by a factor of 10. However, when d like bands cross the Fermi edge a normalisation of the data in this case become very complicated (see section 5.3).

2.3 Surface states at Cu(001)

2.3.1 Aim of the study

In the projected band structure of most solids there exist gaps where bulk electronic states are forbidden. At the surface the crystal potential is truncated and

surface states originating from the bulk bands can be formed inside the band gap. Such states can extend also outside the band gap and are then called surface resonances. Usually in surface science the surface states will be classified as Shockley or Tamm ones named after their discoverers. The appearance of Tamm states (“dangling bonds”) and the related phenomenon of surface band-narrowing are caused by the reduced atomic coordination at the surface that modifies the local density of states (DOS) with respect to the DOS of the bulk. Shockley states, on the other hand, are completely new states formed by matching an exponentially damped solution of the Schrödinger equation in the gap - that is forbidden in the bulk - to an exponentially decaying function in the vacuum region. The condition that the new function has to be continuous and differentiable at the matching point demands that the amplitude of bulk-solution is close beyond a maximum at the surface. This situation may only occur close to the bottom of the gap if the latter is Shockley-inverted, i.e. if the bulk band states at the bottom of the gap are characterised by nodes of the wave-function at the atomic cores. Shockley states are intimately related to the so-called image-states formed by electrons in the vacuum region that are trapped in the potential of their own image-charge. However, while image-states lie far outside the bulk in the vacuum region and reveal energies close to the vacuum energy, Shockley states are localised around the outermost atomic surface layer and frequently found below the Fermi level. SMITH successfully used a combination of elementary multiple-reflection theory and elementary nearly-free-electron theory to account for both image-states as well as Shockley states, that are described both as part of the image-potential Rydberg series with quantum numbers $n=1,2,3\dots$ for the image-state series and $n=0$ for the Shockley state (see [Smi85] and references therein).

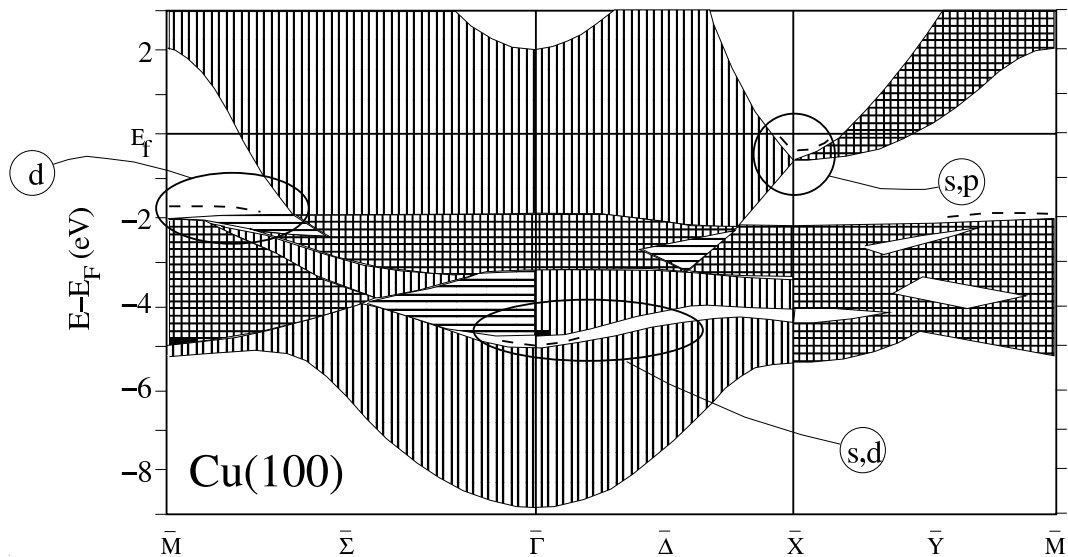


Figure 2.10: Projected band structure normal to the Cu(001) surface with gaps where surface states are expected. The character of the surface states is marked in the figure (taken from [Thi81]).

In Fig. 2.10 the calculated projected band structure of Cu(001) is shown together with the regions, where surface states are expected from theory [Thi81]. The three indicated surface states were confirmed by experiments: a d -type Tamm state near \bar{M} by HEINMANN *et al.* [Hei79] and two Shockley-type surface states: one in the sd band gap at $\bar{\Gamma}$ by WU *et al.* [Wu89], the other one in the sp band gap close to the Fermi level at \bar{X} by KEVAN [Kev83] using photoemission and by DOSE *et al.* [Dos86] using inverse photoemission. There exist additional surface states located in a spin-orbit gap near the already mentioned Tamm surface state [Win86] as well as surface resonances, e.g. at $\bar{\Gamma}$ [Wu89]. While the Tamm surface state region is studied very well and the state is often mentioned in photoemission textbooks, the Shockley-type surface states are not well investigated. In this work, the Shockley state at the \bar{X} -point will be studied due to two main reasons: (i) The state is located very close to the Fermi level and an influence of this state on the results of the Fermi surface measurements presented in the next section should be accounted for, (ii) after manganese deposition, the state still exists and shifts in energy, a behaviour that is unusual for a surface state.

Furthermore, some data will be presented for the Tamm surface state, since it is one of the sharpest solid-state features easily accessible by photoemission that can be used, e.g., to characterise the resolution of the spectrometer for solid-state measurements.

2.3.2 Surface states in the Shockley-inverted bulk gaps: the Cu(001) \bar{X} surface state

In 1983 KEVAN found the previously predicted Shockley surface state in the Shockley-inverted $L_{2'} \rightarrow L_1$ band gap around the \bar{X} -point using high-resolution angle-resolved photoemission [Kev83]. In this work it was reported that the state was visible with ArI ($h\nu=11.8$ eV), NeI ($h\nu=16.8$ eV), and HeI α ($h\nu=21.2$ eV) photons, but the close proximity of the broader bulk feature in the last two cases makes studies with ArI more accurate. This is somewhat puzzling since the effective width of the L band gap observed by photoemission becomes largest at approx. $h\nu=24$ eV. This situation is illustrated in Fig. 2.11. In the figure the $\Gamma XULK$ photoemission plane perpendicular to the Cu(001) surface is presented together with possible free-electron final \vec{k} -positions for the photon energies $h\nu=11.8$ eV, 16.8 eV, 21.2 eV, and 23.1 eV. Also included is the calculated cut through the copper Fermi surface. From this figure it can be derived that the bulk sp band, that is also responsible for the Fermi surface formation, must be much closer to the energy position of the surface state for ArI, and NeI than for HeI α or HeI β ($h\nu=23.1$ eV). This point of view is supported by the results of the same author presented in Fig. 2.14, where a series of spectra including the sp bulk and the surface state taken at different photon energies is presented.

The binding energy of the surface state was determined by KEVAN to be 58 ± 5 meV (see Fig. 2.12) [Kev83]. Fig. 2.8 displays already our results collected

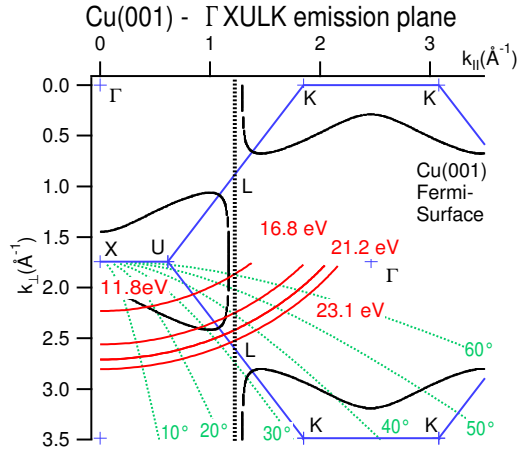


Figure 2.11: Free electron final state \vec{k} -positions (circular arcs) for different photon energies for measurement on Cu(001) in the $\Gamma XULK$ emission plane (calculated for $E_B=0$, high symmetry points given for the first Brillouin zone). The L point and gap is best accessed at $h\nu=24$ eV.

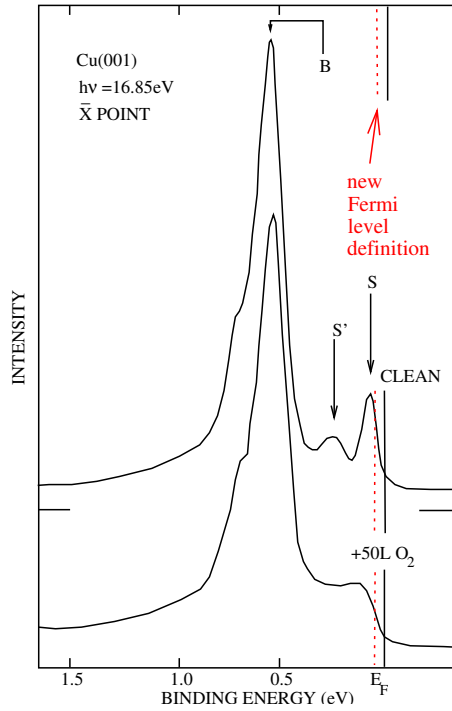


Figure 2.12: Original figure from KEVAN: the Cu(001) Shockley surface state in the region of the \bar{X} point [Kev83]. It should be noted that the originally used Fermi-level position differs from the one conventionally used nowadays (dotted line). A correction applied to the 50 L O_2 /Cu spectrum leaves the peak near the Fermi level (Shockley surface state) at 25 meV binding energy, almost within the thermal broadening of the Fermi edge. The labels B and S are used to describe the bulk sp and the surface state, respectively. The peak S' originates from the $NeI\beta$ satellite at slightly higher photon energy.

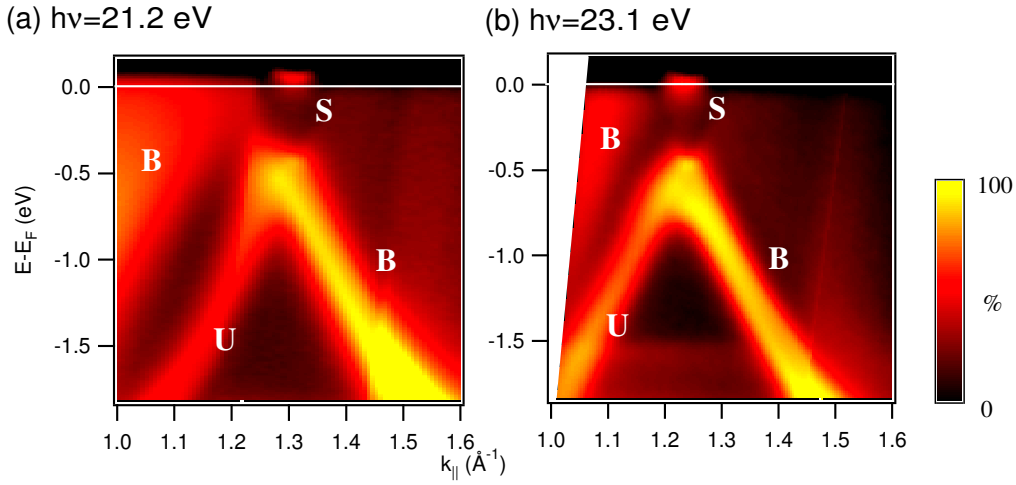


Figure 2.13: Intensity distribution in the near- \bar{X} -region in the $\bar{\Gamma}\bar{X}$ direction of Cu(001) measured by photoemission with HeI α ($h\nu=21.2$ eV) and HeI β ($h\nu=23.1$ eV). The intensity is presented in a logarithmic scale in order to emphasise minor features. The colour scale is shown on the right hand side and is used for all following image plots. B , S , U denote bulk, surface, and umklapp bands, respectively.

with an angular resolution of 1° , while data shown in Fig. 2.13 were measured in a different experiment with 0.3° angular resolution taking advantage from the fact that the dispersion of the copper sp band is quite strong and the peaks can be better resolved. Fig. 2.13 displays the dispersion relation for the bands in the near surface state region. A colour map represents the intensities in a logarithmic scale to strengthen minor features. The spectra were taken here with two different photon energies: HeI α (21.2 eV) and HeI β (23.1 eV). The reason for using the less intense HeI β line is mainly because at this photon energy one comes closer to the L point, where the bulk sp band is more separated from the Fermi level. Furthermore, the cross-section of the surface state is higher at this photon energy [Kev85]. This is seen in the Fig. 2.14 where the surface state region was measured for a series of photon energies [Kev85]. It should be noted that in both figures of our experiments (conventional PE plot in Fig. 2.8 and colour plot in Fig. 2.13) the highest intensity of the surface state peak is found *above* the Fermi edge while KEVAN obtained a positive binding energy. The reason is that the Fermi edge is thermally broadened, making observation of peaks above the Fermi energy possible. Since the Fermi function cuts the peak within a quite narrow energy range as compared to characteristic widths of photoemission features, such a peak should be extremely sharp and of high intensity above the Fermi edge to be detected by PE. Such an effect was first reported for some features of the partially unoccupied spin minority d band of Ni(111) by GREBER *et al.* [Gre97]. This band was observable at room temperature although it lies 125 meV *above* the Fermi edge position. Since the observed peak in the present study is cut by the Fermi level, its exact position cannot be easily determined since

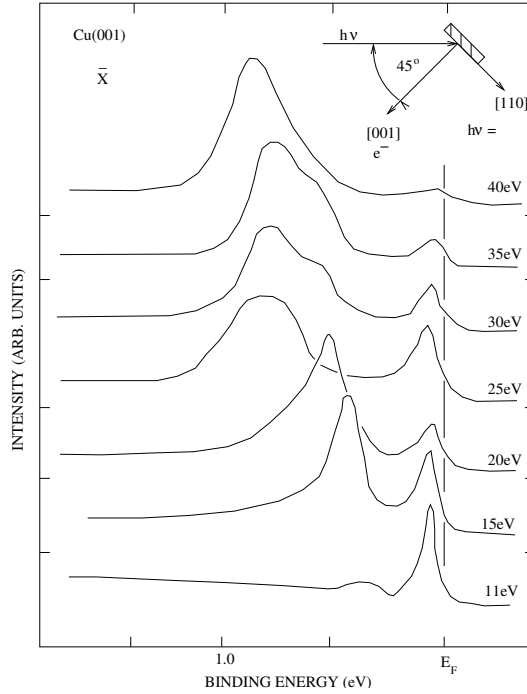


Figure 2.14: Cu(001) photoemission spectra close to the \bar{X} point of the surface Brillouin zone in the L band gap. The structure near E_F is the Shockley surface state, the others are the bulk sp band and its respective umklapp features seen at higher photon energies (figure taken from [Kev85]).

its width and line-shape is unknown. Apart from that the question arises, why KEVAN found the state below the Fermi level while it is found here above E_F ? A first answer can be given on the basis of his original spectra displayed in Fig. 2.12. After quenching of the surface state by oxygen adsorption the Fermi edge is not longer masked by the surface-state emission. Its position may be determined from the point of inflection of the leading edge of the spectrum, whereas in “earlier” works the Fermi level position was considered to be at an energy where the photoemission intensity becomes nearly zero. With the new Fermi-level position, the original binding energy of 58 meV would change to approx. 25 meV, a binding energy value that is located well inside the width of the thermally broadened room-temperature Fermi edge. Furthermore, if the surface state is not fully quenched, the Fermi level position even in the O/Cu(001) spectrum is still too high, so the surface state binding energy might be even smaller. This shows, that the Fermi level definition is a very important problem. It should be taken at \vec{k} points, where no narrow bulk bands cross E_F and no surface states close to E_F occurs. Another possibility is to measure E_F for polycrystalline metals with sp bands only crossing the Fermi edge (e.g., Au, Ag, Cu). In the data presented here, the Fermi-edge position was obtained from spectra taken at large emission angles, where no direct band crossing occur (see Fig. 2.13, Fermi level taken at approx. 1.5 \AA^{-1}). Apart of the wrong calibration of the Fermi energy, there exist further possibilities to explain the observed differences in the surface state position. A

very important point is the cleanliness of the sample. Deterioration of the sample surface is probably the reason, why the surface state is only rarely mentioned in literature. The Cu(001) crystal should have a very good quality and should be very clean. Here, the surface state was obtained after several sputtering/heating cycles (about 30). No oxygen had been found with UPS ($h\nu=21.2$ eV), where the oxygen $2p$ cross-section is maximal. Traces of other contaminations were checked by X-ray photoemission and found to be negligible. The LEED indicated a very sharp $p(1\times 1)$ pattern with nearly no background intensity. However, as it will be shown in chapter 3.2.4, this Shockley surface state is very sensitive to the potential barrier at the surface that is related to the work function. Even small amounts of contaminations can change the work function drastically and, hence, shift the position of the Shockley surface states. Such impurities can be, for example, hydrogen atoms which cannot be detected by X-ray photoemission and only with difficulties by UPS. In modern UHV systems the remaining pressure is mainly due to hydrogen, that can be hardly pumped by turbo-molecular pumps usually used. However, as [Kev83, Kev85] did not give any experimental details about working conditions and Fermi level calibration, a comparison with the presented data regarding the origin of this energy shift cannot be done. Furthermore, as the energy position of the surface state is found above the Fermi level, a dispersion relation as given by KEVAN cannot be reliable, since a least-squares fit of the corresponding features requires the knowledge about width and line-shape of the peak.

2.3.3 Cu(001) Tamm surface state near \bar{M}

In contrast to the Shockley surface state, Tamm states are pushed out of the bulk continua by an increased Coulomb repulsion term arising from excess sp electron density at the surface. Therefore they can be found usually very close to bulk states in a band gap as they are split of the same bulk band. In Cu(001) HEINMANN *et al.* first observed such a Tamm surface state in the d -like band gap near the \bar{M} point of the surface Brillouin zone of Cu(001) [Hei79]. In our work, the state was measured with two photon energies: 21.2 eV and 40.8 eV, and was already marked in the spectra presented in Fig. 2.4. The spectra were taken with an angular resolution of 1° . The dispersion of the state is displayed in Fig. 2.15. As surface states do not show dispersion with k_\perp , both dispersion curves taken with HeI and HeII light must be identical. A parabolic fit to the data is also shown. Such a parabolic behaviour is typical for nearly free electron like states. From the slope of the curve an effective mass m_{eff} of the state can be calculated using

$$E_B = E_0 + \frac{\hbar^2}{2m_{eff}}(\vec{k}_\parallel - \vec{G})^2 \quad (2.1)$$

that yield $m_{eff}=(-0.38\pm 0.04)m_e$ with respect to the free electron mass m_e (E_0 is the binding energy at the boundary of the surface Brillouin zone). A lower

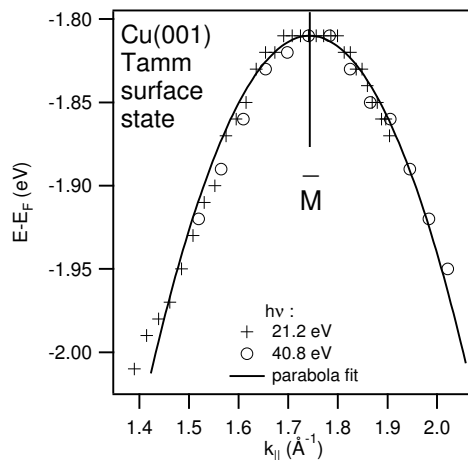


Figure 2.15: Dispersion of the Cu(001) Tamm surface state around \bar{M} along the $\bar{\Gamma}\bar{M}$ direction with HeI α and HeII α photons. The least squares fit of the data resulted in an effective mass of $(-0.38 \pm 0.04)m_e$.

absolute value of the effective mass signifies a stronger dispersion as compared to the free-electron like dispersion.

The linewidth of the peaks in a photoemission experiment depends on several parameters like the lifetime of the state, the resolution of the analyser - energy as well as angular resolution are important for dispersing features -, and the thermal broadening of the state. The width of the peak can be decreased improving the resolution of the spectrometer, but also by cooling the sample to lower temperatures. The energy resolution of the Scienta 200 spectrometer, that was used here, amounts to approx. 10 meV at the pass energy of 5 eV applied during this measurement. At room temperature the Tamm surface state has a width of 40 meV⁷. Fig. 2.16 shows the spectra taken at temperatures of 100 K and 30 K. Since the room temperature spectrum is nearly identical to the spectrum obtained for 100 K, the former is not shown. However, already a very slight sharpening of the peaks takes place, the width of the surface state decreases to 35 meV. Surprisingly further decrease of the temperature does not show the expected effect, the Tamm surface state decreases in intensity and the peak becomes broader. Furthermore, the spectral feature at 2.05 eV binding energy that was identified as a surface state located in a spin-orbit gap [Win86] disappears totally. The reason of this behaviour is still far from clear. Apart from physical reasons like surface-phase transitions, lattice constant changes or surface relaxation, the effect may be caused by experimental artefacts, e.g., (i) a slight sample movement due to tensions during cooling, (ii) a surface damage created by UV irradiation as observed in the 4*f* signal of Ce based systems [Gar98], or most probably (iii) freezing/adsorption of rest gases (e.g., N_2 , CO) on the sample surface causing a quenching of the surface state.

⁷Note that the width of occupied peaks does *not* depend in the same way on the temperature as the Fermi function.

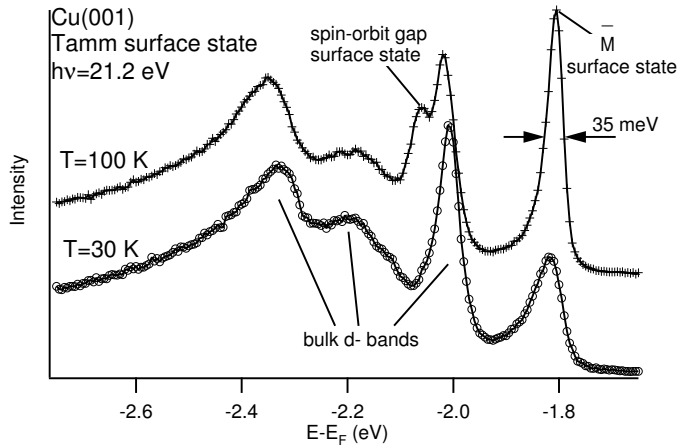


Figure 2.16: Decrease of the intensity of the Tamm surface state at lower temperature. While the feature should become sharper with lower temperature, in this measurement the contrary occurs. Spectra were taken with HeI α light along the $\bar{\Gamma}\bar{M}$ direction at an emission angle of 63 $^\circ$.

2.3.4 Results of calculation of photoemission spectra

Photoemission spectra were calculated using a LKKR (Layered Korringa-Kohn-Rostoker) approach that will be described in details in chapter 3.2.2. Here only the results for the Cu(001) surface are given in order to prove the reliability of the approach. Fig. 2.17 compares the calculated and the measured spectra of Cu(001) in the $\bar{\Gamma}XW\bar{K}$ plane ($\bar{\Gamma}\bar{M}$ high symmetry direction) for a photon energy of 21.2 eV. In general, theory and the experiment coincide quite well. While the experimental *sp* band positions are the same as in the theory, the *d* bands are shifted to lower binding energy in theory. This is due to the calculation method used: the potentials are calculated by local spin density approximation (LSDA or LDA) for a single Cu atom and these values are then used for the LKKR formalism. LSDA, however, does not take relaxation effects caused by PE into account. This problem was already discussed in the previous section.

Furthermore, the Tamm surface state is not seen in the results of the calculations. This can be understood by the fact that the energy position of the surface states depends strongly on the surface potential used in the model. Here the form and amplitude of the surface potential were adjusted in such a way that the Cu *Shockley* type surface state in the *L* band gap is found at the same energy position as in the experiments. It seems, however, that the potential used is not suitable for the *Tamm* surface state.

2.4 Fermi surface investigations

The Fermi surface is one of the most important properties of metals. Apart from electric conductivity it defines several other properties of solids. The form of

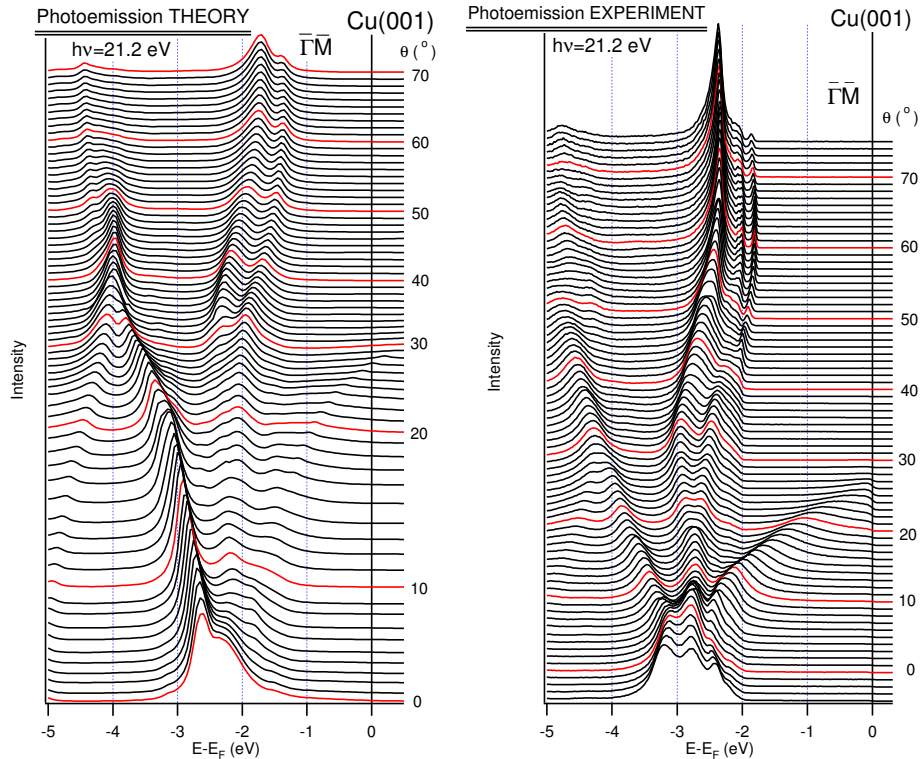


Figure 2.17: Comparison between the LKKR calculated Cu(001) photoemission spectra in the ΓXWK plane ($\bar{\Gamma}\bar{M}$ direction) and the experimental data. Theoretical and experimental peak positions as well as the intensity distributions are in fair agreement with each other. While the sp band position is exactly the same in the left and right panel, the calculated d band position should be shifted to higher binding energies by 0.6 eV to coincide with the experimental ones. This shift is probably explained by the fact that the theory considers the ground state while the photoemission process in the final state deals with a screened Cu^+ atom.

the Fermi surface is important. It is usually measured applying the de Haas-van Alphen effect, where the electron tracks are monitored via oscillations of the magnetic moment of the sample as a function of the external magnetic field applied. Further details about the relevance of the Fermi surfaces and their determination using the de Haas-van Alphen effect are given, e.g., in [Kit85, Ash76].

In the last years also photoemission is often used to characterise Fermi surfaces. The idea is that the Fermi level defines the energy separating the occupied and unoccupied electronic states. Photoemission samples only the occupied bands. When such an occupied band crosses the Fermi energy E_F an intensity enhancement at E_F is detected in PE. The easiest method to obtain the information on the Fermi surface is, thus, a measurement of the PE intensity at the Fermi level at all possible \vec{k} points of the Brillouin zone. For a 2-dimensional system such experiments can be performed quite easily since only one photon energy is needed. After calibration of the Fermi level position, the intensity distribution

is measured. Thereby the polar and azimuthal angles of either the analyser or the manipulator are changed. To study a 3-dimensional sample, different photon energies have to be used in order to sample the whole Brillouin zone. This task is usually extremely time consuming. There exist already special display-type photoelectron spectrometers [San91, Tho95] that are faster in the data recording than conventional ones. These spectrometers, however, are characterised by a relatively low energy resolution. A further problem of the photoemission based Fermi surface mapping is the normalisation of the data. The need of the normalisation has several reasons: *(i)* at synchrotron sources the electron beam is not stable, e.g., the electron current in the ring continuously decreases with time until the next “injection” reestablishes the photon flux, *(ii)* during the experiment both, manipulator and analyser should be rotated around the same axis or, when the analyser is fixed, the rotation axis should lie in the surface of the sample. Due to the construction of the manipulator used during the laboratory experiments these conditions, however, are not exactly fulfilled. There are further points, which make a normalisation necessary, that will be discussed later. At synchrotron radiation facilities the normalisation due to the beam instabilities can be easily done by a parallel measurement of photon flux. It is more complicated to overcome the problem *(ii)* since the PE intensity depends strongly on the exact position of the sample with respect to the focus of the analyser (for the Scienta 200 analyser about 5 mm×1 mm [Bal]). Conventional electron energy analysers can simultaneously measure only at one specified \vec{k} point (single channeltron mode), while the Scienta 200 analyser equipped with a channelplate is able to monitor at the same time spectra in a window of up to 14° emission angles with a resolution down to 0.1°. The disadvantage is, however, that the transmission function of the analyser (different parts of the channeltron correspond to different positions on the sample surface) depends strongly on the focus and, hence, on the position of the sample relative to the analyser. If, for example, the sample does not rotate exactly around the spectrometer axis, strong intensity changes are obtained. Further disadvantages are polarisation effects, that make a consistent normalisation for both *sp* and *d* bands nearly impossible. Since the normalisation procedure to obtain reliable data is rather difficult it will be discussed in the following with more detail. There are several possibilities to calibrate PE intensities. Nearly all of them gave good results for Cu(001), but none of them was able to account for *sp* and *d* bands crossing the Fermi level as in the cases of the ferromagnetic Fe, Co, and Ni films. The approaches to normalise PE intensities used in the present work are:

- (i)* **Fermi level intensity:** in one high symmetry direction an additional cut of the Fermi surface intensity is measured by rotating the sample every 1°. A normalisation to this cut allows to account for the characteristics of the channelplate. However, since the polar cut spectra are not taken at the same incident angles as in the normal Fermi surface measurement (window mode, here $\Delta\theta=10^\circ$), this normalisation method cannot inhibit

effects induced by the different measuring positions (focus) or polarisation effects.

(ii) **Total band intensity:** Since usually the band structure is measured before or after the Fermi surface mapping at the same polar angle positions (but only for one or two high symmetry directions), the experimentally obtained PE bands can be used to normalise the Fermi surface data assuming that the total signal intensity integrated over the whole photoemission spectra including valence bands emission as well as secondary electrons is constant. Since this band structure investigation is carried out exactly on the same position as in the Fermi surface mapping but on one azimuthal angle only, this integrated value includes focal position as well as channelplate characteristics. However, the assumption of a constant spectral signal is usually not valid since there exist matrix element effects, symmetry selection rules and polarisation effects, that are angle-dependent and affect the signal intensity.

(iii) **Manual method:** Fermi surface data taken in the window mode for the window corresponding to the lowest incidence angle are normalised applying one of the above described method or using the intensities in a region where no direct band crossings of the Fermi edge occur. Then, the factors for each 1° segment of the 10° window are used for the window at the next (higher) incidence angle. In order to achieve again a constant intensity in spectral regions where no spectral features occur these factors usually have to be changed slightly. A further factor for each 10° window, then, is selected to match all windows without steps in the intensity. Finally, this method means that each ring corresponding to a given emission angle is normalised manually. Polarisation effects are still not accounted for by this method. One can try to minimise them manually but usually this leads to a steplike background mainly from the broad *sp* bands (see. Fig. 5.10 in chapter 5.3).

For the majority of the presented Fermi surface data method (ii) was used. Here, the results were usually better than those obtained by method (i). In a few cases of ferromagnetic films, where method (ii) did not lead to reasonable results, method (iii) was applied.

Since the Cu(001) single crystalline surface is relatively easy to prepare and the electronic structure is well studied, this surface was used as “test” material for Fermi surface studies with photoemission. AEBI *et al.* investigated all Cu low index surfaces with HeI light ($h\nu=21.2$ eV) [Aeb94], AVILA *et al.* used additionally synchrotron radiation and different photon energies [Avi95] for the Cu(001) surface only. Fig. 2.18 shows the Cu Fermi surface obtained from a LCAO approach [Leh97]. The amount of *d*-character is indicated by a colour scale, *d*-contributions to the wave function lie usually between 35 and 70%. Also sketched are the final-state \vec{k} positions related to the used photon energies. Noble metals (Cu, Ag, and Au) are monovalent like the alkali metals. While the

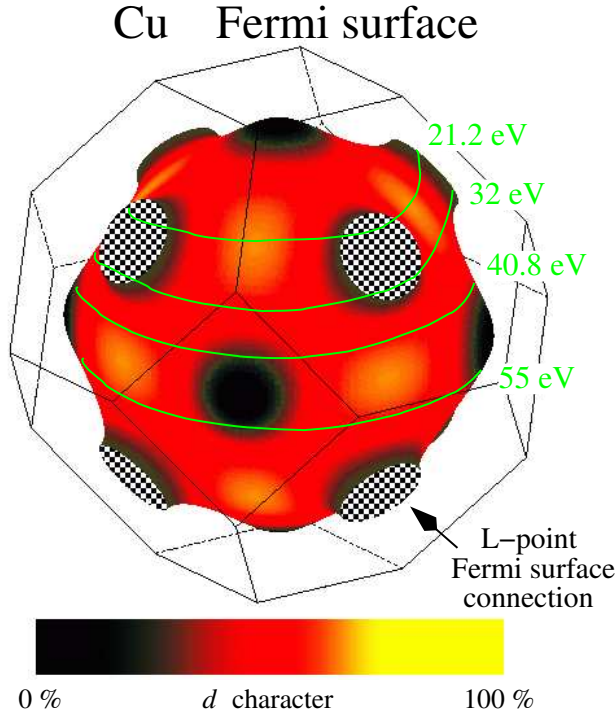


Figure 2.18: Cu Fermi surface calculated by a LCAO approach and shown in the second 3-D Brillouin zone. The colour scale shows the d character of the so called sp band forming the Fermi surface. Also shown are the photon energies that were used for Fermi surface mapping during the present work.

Fermi surfaces of the alkali metals are spherical, the noble metal Fermi surfaces touch the Brillouin zone boundaries around the L -point leading to a connection of neighbouring Fermi spheres via the so-called “dog bones”.

As shown in Fig. 2.18, for photon energies between approx. 20 eV and 33 eV the cut through the Fermi surface touches the “necks of the dog bone” of the Fermi surface while higher photon energies cut the Fermi surface producing a closed curve with circular shape. From the experimental θ , φ values the parallel component of the wave vector can be calculated by (1.9) and the intensity $I(k_{\parallel,x}, k_{\parallel,y})$ can be presented in a parallel projection as a contour plot or as an image using a defined colour scale for the intensity. Fig. 2.19 shows the experimental results for the cuts through the Fermi surface involving the “necks” ($h\nu=21.2$ eV and 23.1 eV) and the “belly” ($h\nu=40.8$ eV). Also presented are the results of a LCAO-calculations for the same energies and free-electron like final states. All details of the calculated structure are observable in the experimental data as intense features. While the coincidence between experiment and theory is very good as far as these main features are concerned, additional structures can be observed in the experimental data. While the intensity variation is mainly due to matrix-element effects and symmetry selection rules, there are two types of additional features. One is located exactly at the \bar{X} point of the surface Brillouin zone and is originating from the Shockley surface state that was discussed in detail in

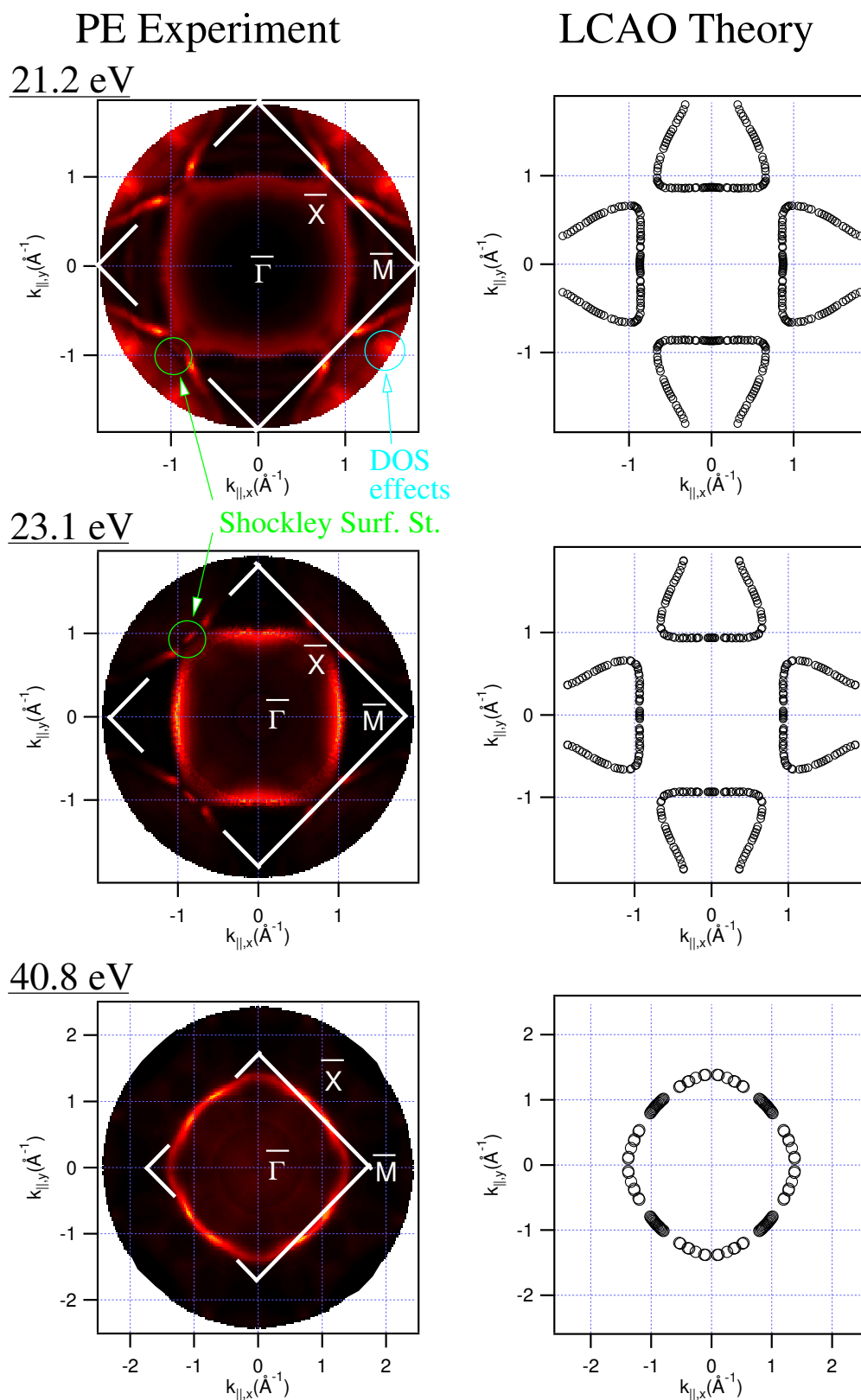


Figure 2.19: Fermi surface investigations of Cu(001) by photoemission: cut through different \vec{k} positions of the 3-D Brillouin zone using different photon energies (left) as compared to the LCAO-calculated Fermi edge crossing positions (right).

Cu(001) constant energy cuts

$h\nu=23.1$ eV

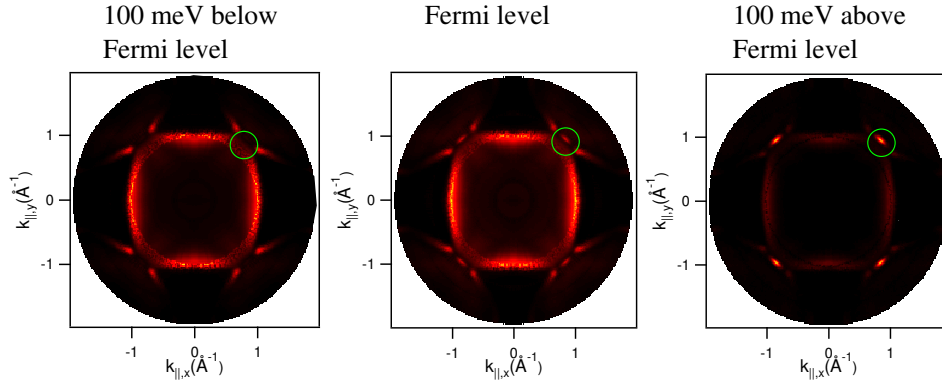


Figure 2.20: Constant energy surfaces of Cu(001) measured at 100 meV below (left) and 100 meV above the Fermi level (right) with $h\nu=23.1$ eV. In the centre the Fermi surface is shown. The position of the Shockley surface state is marked by a circle. The state is already seen at the Fermi level becoming the most prominent feature in the constant energy plot above the Fermi level. The energy position of the state is, therefore, expected above E_F .

section 2.3.2. The other marked feature (DOS effects) is usually of less intensity. There are neither bands crossing E_F nor surface states in this \vec{k} region. AEBI *et al.* [Aeb94] as well as AVILA *et al.* [Avi95, Lin01] present Cu(001) Fermi surface cuts taken at a photon energy of 21.2 eV, but their data do not show indications for the presence of the Shockley surface state or the other mentioned feature. Since the Shockley state has a slightly higher intensity at $h\nu=23.1$ eV, also the Fermi surface cut taken at the less intense HeI β line is given. As expected, the Shockley state is better visible. To obtain the energy position of the Shockley surface state such angular distribution plots can also be used. Such plots have to be measured, however, not only at the energy corresponding to the Fermi level, but also at other constant binding energies slightly deviating from E_F . As an illustration Fig. 2.20 shows constant energy plots of the Cu(001) surface measured with a photon energy of 23.1 eV. On the left hand side the constant energy plot at 100 meV binding energy is plotted, in the middle the Fermi surface (constant energy plot at E_F), and on the right hand side the constant energy plot 100 meV above the Fermi level. The circle denotes the \vec{k} region, where the Shockley surface state touches the Fermi edge. While at 100 meV binding energy apart from bulk features no indication for additional structures are observed, in the Fermi surface cut appears already a new feature. This new feature is even more pronounced in the constant energy cut 100 meV above the Fermi level. In comparison to the bulk-derived features the intensity of the extra feature is rather high above E_F . This observation together with the fact that no hint for the surface state is observed 100 meV below E_F confirm the formerly found energy position of the Shockley surface state *above* the Fermi edge.

The other additional feature seen in the Cu(001) Fermi surface cut at 21.2 eV in

Fig. 2.19 is based on another phenomenon. LINDROOS and BANSIL calculated the Fermi surface of Cu(001) applying a one-step model of photoemission using constant initial energy angle-scanned photoemission [Lin96, Lin01]. Apart from the direct bulk transitions the authors also found additional structures and assigned them to density of states type indirect transitions. The main reason for these effects is a consideration of the real final state in the PE process. While LINDROOS and BANSIL found several of such density of states derived intensity enhancements, in the Fermi surface cuts presented in Fig. 2.19 one of these proposed features becomes visible marked with the label “DOS effects”. A stronger contrast for such low intensity features is obtained by presenting the Fermi surface cuts with a logarithmic intensity scale. An example is shown in Fig. 2.21, where the same Fermi surface cuts as in Fig. 2.19 are shown in a linear (left hand side) and logarithmic intensity scale (right). Not only in the HeI α Fermi surface cut, but also in the other cuts clear differences between the two presentations are seen.

2.5 Conclusions

This introductory chapter should only give some insight into the difficulties of photoemission as a main tool used in this work to obtain band structure information. Even one of the most studied systems like the Cu(001) surface that is characterised by a relatively simple electronic structure is still far from being completely understood. First PE experiments on this surface were carried out between 1975 and 1990, with energy resolutions of an order of magnitude lower than it can be achieved now with state-of-the-art spectrometers. Furthermore, since both the photon flux of light sources and transmission of the analysers were low at this time contamination of sample surfaces during the often very time consuming measurements were a serious problem for the experimentalists.

The available tools for the theoretical description of the systems are still not sufficiently advanced. Most theories are based on the local density approximation (LDA) providing results that differ from the experimental data for the d bands, while the description of the sp bands are in agreement with the experiment. Other theoretical studies, where photoemission spectra are calculated directly, are less common and are usually difficult (see next chapter).

Here, only very few details concerning the Cu band structure were considered. All of them relate to phenomena that will be discussed in the further chapters. A new PE feature, which can be attributed to an umklapp process was found. This umklapp process was predicted by theory but still not observed experimentally. Additionally, the Shockley surface state close to the \bar{X} point was observed for the first time in a Fermi surface cut. Concerning this state further work should include an exact determination of the Shockley surface state position, that can be done, e.g., by lowering the temperature of the sample: If the state is situated

Cu(001) Fermi surface cuts: different presentations

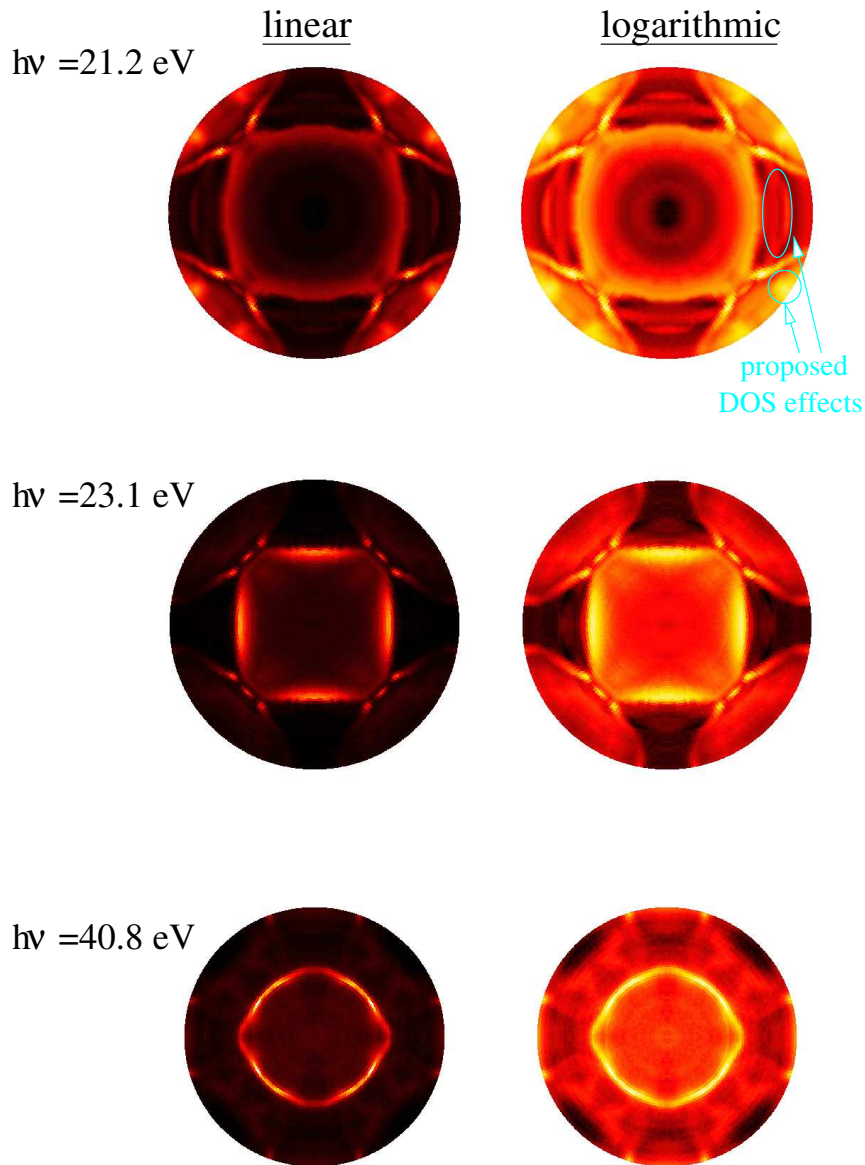


Figure 2.21: Fermi surface cuts of the Cu(001) surface for different photon energies in a linear and in a logarithmic intensity scale. Weak features, not arising from direct transitions, are better resolved with logarithmic presentation.

above the Fermi edge, it should disappear. A further interesting point to be studied is the appearance of additional features in the Fermi surface cuts that are most probably related to density-of-states phenomena or photoelectron diffraction effects.

Chapter 3

Majority and minority states in $c(2\times 2)\text{MnCu}/\text{Cu}(001)$ measured by photoemission

3.1 Introduction

Since the first preparation of the $c(2\times 2)\text{MnCu}$ surface compound in 1982 a lot of work has been performed in order to study the unusual properties of this system. It was regarded as a model system for a new class of surface compounds based on the checkerboard $c(2\times 2)$ structure [Wut93b]. In the meantime this assumption has been confirmed by finding similar $c(2\times 2)$ Mn-derived systems, such as Mn on the (001) fcc surfaces of the $3d$ metals Ni [Wut93a], Co [Cho98], Fe [this work] and on the noble metals Ag [Sch96] and Au [Sch01]. Magnetism was encountered as the driving force for the formation of these surface compounds. The magnetism arises from the Mn atoms that have a larger Mn-Mn nearest neighbour distance in the compound than that in Mn metal and form, therefore, in contrast to Mn metal considerable local magnetic moments.

For the Mn/Cu(001) interface more than twenty publications are available indicating the scientific interest in this system. While the earlier investigations dealt mainly with the structural properties, particularly the unusual buckling of the manganese atoms at the surface, recent work focused on magnetic properties and band structure. The most recent theoretical studies predict different values for the total band splitting that requires further investigations. A detailed summary of previous results about the crystalline structure is given in appendix A.

This chapter will concentrate on photoemission experiments on the $c(2\times 2)\text{MnCu}$ surface and compare the experimental results with those of LKKR calculations. The chapter is divided in two main parts: conventional photoemission measurements and Fermi surface investigations.

3.2 Band structure analysis of $c(2\times 2)\text{MnCu}$

3.2.1 Photoemission measurements of $c(2\times 2)\text{MnCu}$

The $c(2\times 2)\text{MnCu}/\text{Cu}(001)$ superstructure is obtained by depositing half a monolayer of Mn onto clean $\text{Cu}(001)$. Hereby the $c(2\times 2)\text{MnCu}$ surface compound layer is formed on top of a nearly non-affected bulk $\text{Cu}(001)$ substrate [Flo92, Wut93c, Too96]. Valence-band photoemission that was used in the present work to study the surface compound is a technique that is not element specific and can, therefore, not distinguish between the Mn- and the Cu-derived parts of the band structure. Furthermore, theoretical investigations predict strong hybridisation between the manganese and copper bands making a discrimination between them nearly impossible. The obtained signal in a PE experiment stems not only from the top surface layer but also from underlying substrate layers, the contribution of which depend on the actual kinetic energy of the electrons. In Fig. 1.3 the mean free path of electrons in a solid was shown. The lowest electron escape depth of about 1 ML is obtained at kinetic energies around 40 eV. This means that passing 1 ML of the material the number of photoelectrons emitted from the bulk decreases only to $1/e$. For other photon energies the contribution of emitted valence electrons from the substrate is even higher. While photoemission spectra were taken at several photon energies ($h\nu=21.2$ eV, 23.1 eV, 32 eV, 40.8 eV, 55 eV, and 65 eV), Fig. 3.1 shows experimental data only for the most surface sensitive case of $h\nu=40.8$ eV. Even at this photon energy there are almost no differences visible in the spectra between clean $\text{Cu}(001)$ and $c(2\times 2)\text{MnCu}/\text{Cu}(001)$.

3.2.2 LKKR-based photoemission calculation of the $c(2\times 2)\text{MnCu}/\text{Cu}(001)$ surface compound

Calculations of layer-resolved densities of states (LDOS) as well as simulations of photoemission spectra were performed within a relativistic layer-KKR Green function theory. Since details of the method have been given elsewhere (cf. [Hal93], and references therein), only some key aspects are briefly presented here: The method is based on an one-electron Dirac Hamiltonian including an effective magnetic field. It enables in particular description of magnetic dichroism effects in photoemission, since spin-orbit and exchange interactions are included on an equal footing [Hal95]. According to the layer-KKR formalism, the electron-hole multiple inelastic scattering is accounted for by means of relativistic Green functions, proceeding from single-site scattering to intra- and, finally, interlayer multiple scattering, what is particularly suited for treating magnetic thin films and multilayer systems. Electron and hole lifetime effects are modelled by consideration of the space- and energy-dependent imaginary part of the effective inner crystal potential. The real part of the latter inside the muffin-tin spheres was taken from self-consistent linear muffin-tin orbital calculations in the atomic

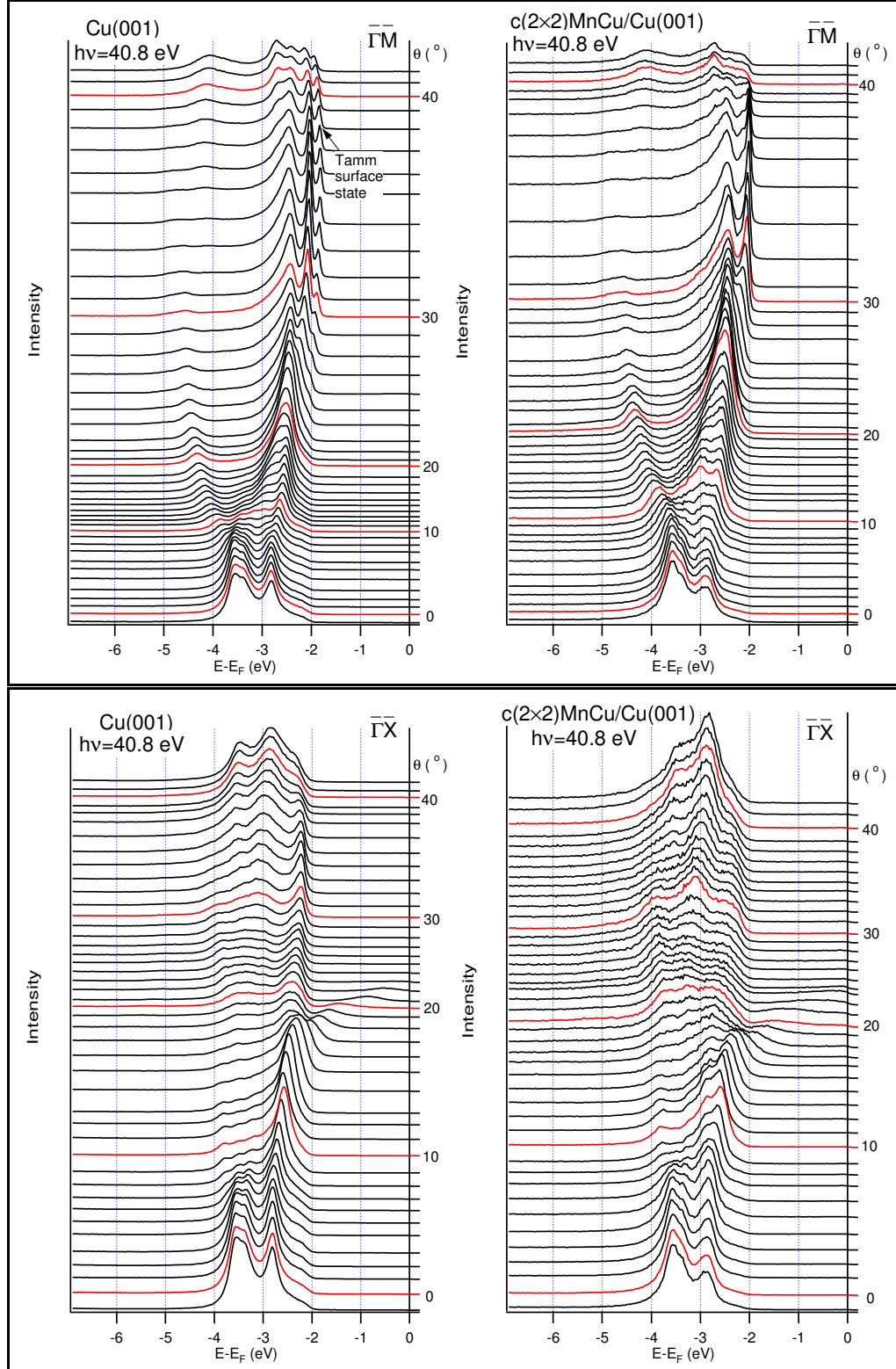


Figure 3.1: Photoemission spectra of Cu(001) (left) and $c(2 \times 2)$ MnCu/Cu(001) (right) in the high symmetry directions $\bar{\Gamma}\bar{M}$ (top) and $\bar{\Gamma}\bar{X}$ (bottom), respectively.

sphere approximation (LMTO-ASA) performed for a $c(2\times 2)\text{MnCu}/\text{Cu}_6$ supercell with empty monolayers at one ('vacuum') side of the MnCu compound layer for better simulation of the near-surface region. Empty spheres in this region are added to improve the ASA-results and thus to account for effects of non-spherical spatial distribution of the charge density, although with limited accuracy. Within the local spin density approximation (LSDA) to density functional theory (DFT), the obtained spin moments are $3.83\mu_B$ and $0.095\mu_B$ for Mn and Cu atoms in the compound MnCu surface, respectively, where a ferromagnetic alignment of the magnetic moments was assumed. Buckling of the Mn atoms within the compound layer of 0.3 \AA , established earlier [Wut93b], was also taken into consideration. Within LKKR, the information about the occupied states is contained in a retarded Green function matrix $G_{N,N'}(\vec{k}_{\parallel}, E)$, where N and N' label the spatial positions (specific atoms and monolayers), and is given in terms of the \vec{k}_{\parallel} -, layer- and symmetry-resolved density of states (LDOS) at energy E as

$$N_{N,S}(\vec{k}_{\parallel}, E) = -\frac{1}{\pi} \text{Tr} \text{Im} \langle S | G_{N,N'}(\vec{k}_{\parallel}, E) | S \rangle,$$

where S stands for given number-projected states, e.g., resolved in angular- and spin-quantum numbers. The same Green function is used for calculations of PE spectra within a one-step model, applying relativistic dipole-transition matrix elements. Final states were treated as time-reversed LEED states (by operator \hat{T}):

$$\Psi_{\vec{k}_{\parallel}, E}^{\tau}(\vec{r}) = \hat{T} G(\vec{k}_{\parallel}, E) \hat{T}^{\dagger} \exp(i\vec{k}_{\parallel} \vec{r}) \chi^{\tau} \delta(z - z_0),$$

describing photoelectrons with spin τ at the detector plane $z = z_0$, with χ^{τ} being the spin wave function of the emitted electron (see, e.g., [Hal93]). Interaction of the electron with a monochromatic electromagnetic field $\vec{A}(\vec{r}) \exp(i\omega t)$ is taken in the dipole approximation, i.e. \vec{A} spatially constant.

For the surface potential barrier we adopted a step function as the simplest approach, adjusting the onset at $d_B = 0.255a$ (where a is the bulk lattice constant) above the topmost internuclear plane in order to achieve an optimal overall fit of the Shockley surface state to the experimental data of Cu(001) (cf. [Loe96] and references therein). Since we are concerned only with the occupied surface states, the asymptotic charge image potentials can safely be neglected. On the other hand, the positions of *magnetic* surface states depend much less on reasonable changes of the surface barrier location than on changes of the surface magnetisation and magnetic configuration [Hal95].

3.2.3 Method for the determination of the Mn spin majority band

Fig. 3.1 shows that the conventional PE results are not very well suited to obtain informations to distinguish Mn and Cu derived bands; consequently other

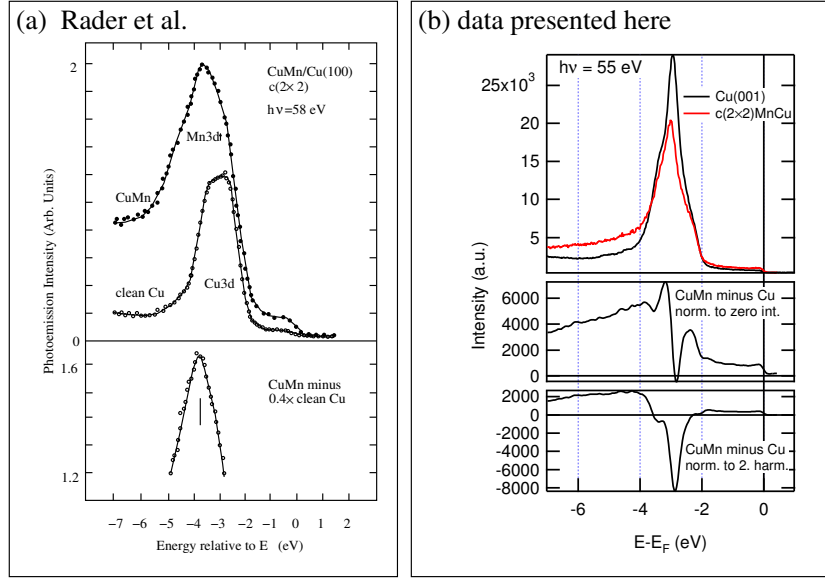


Figure 3.2: Resonant photoemission spectra of $c(2\times 2)\text{MnCu}/\text{Cu}(001)$ taken by RADER *et al* [Rad97a] (left hand side), and the present data normalised in different ways (right).

methods have to be used. RADER *et al.* [Rad97a] used resonant photoemission at the $\text{Mn } 3p \rightarrow 3d$ threshold to enforce the manganese signal. In this way a position of 3.7 eV binding energy for the $\text{Mn } 3d$ spin majority spin band was obtained from the spectral difference of $c(2\times 2)\text{MnCu}/\text{Cu}(001)$ and $\text{Cu}(001)$ (see Fig. 3.2[a]) [Rad97a]. While the $\text{Mn } 3p \rightarrow 3d$ excitation threshold is located at approx. 48 eV photon energy, the authors used a photon energy of 58 eV, quite far away from the threshold where the effect of the resonance is expected to be very low. In the angle resolved experiment performed in the present study the mentioned resonance effect could not be confirmed. Fig. 3.2 compares the data of RADER *et al.* [Rad97a] and the results obtained within this work. The difference spectra of $c(2\times 2)\text{MnCu}/\text{Cu}(001)$ and $\text{Cu}(001)$ in the data presented here (right panel) were obtained in two different ways: (i) normalisation to maximum intensity followed by subtraction and (ii) normalisation to the background intensity at higher harmonics above the Fermi energy followed by subtraction. Neither of these methods gives clear evidence for a new feature at 3.7 eV binding energy. The features obtained in the difference spectra are mainly due to broadening of the main peak, an expected behaviour in a process of multilayer formation where the quality of the surface slightly decreases. The latter is also the reason for the somewhat higher background seen for the $c(2\times 2)\text{MnCu}$ sample. A polarisation effect can be ruled out as a reason for the discrepancy, since a 45° incidence angle (mixture of s and p polarisation) was used here. For all photon energies applied in the present work a shift of the main peak position in normal emission spectra of $\text{Cu}(001)$ by less than 100 meV to higher binding energies is observed. This shift is, however, *not* interpreted as due to the Mn spin majority band, but caused by a weak charge transfer from Mn to Cu . Since there are discrepancies in the data,

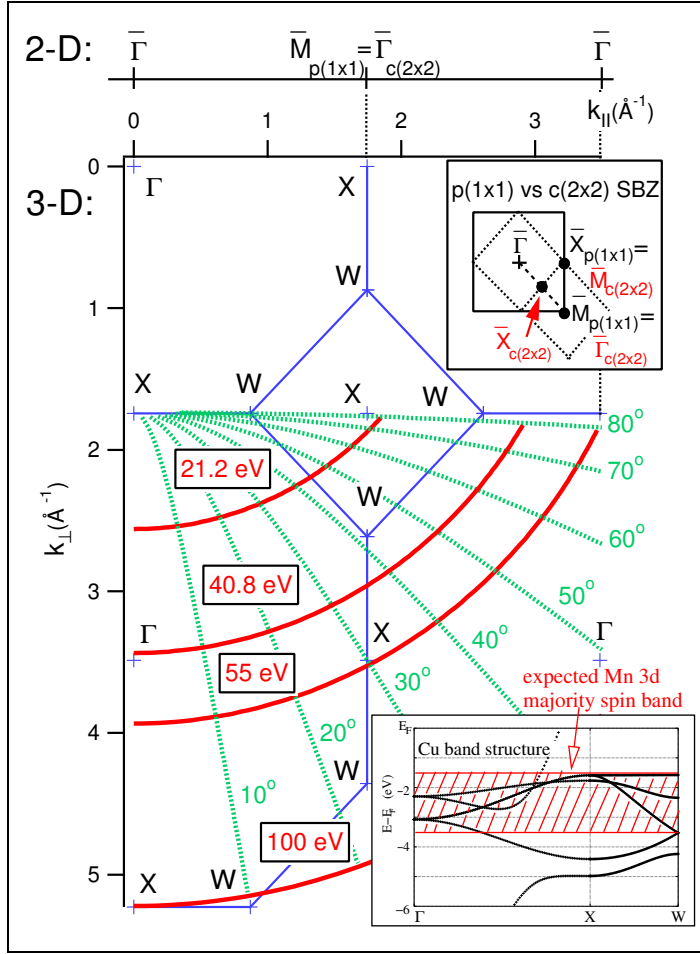


Figure 3.3: ΓXW photoemission plane of Cu(001) ($\bar{\Gamma}\bar{M}_{p(1\times 1)}$ high symmetry direction that transforms into the $\bar{\Gamma}\bar{X}\bar{\Gamma}_{c(2\times 2)}$ direction in the $c(2\times 2)$ surface Brillouin zone as seen in the top inset). Bottom inset: LCAO band structure calculation of Cu for measurements along ΓXW that corresponds to measurements in the $\bar{\Gamma}$ point of the first and the $\bar{\Gamma}_{c(2\times 2)}$ of the second SBZ. The energy region where the Mn 3d spin majority band is expected from the theory is specified (shaded) in the figure.

another method for determining the Mn 3d spin majority band position had to be found.

The $c(2\times 2)$ MnCu surface has a modified symmetry as compared to the $p(1\times 1)$ copper substrate. This is illustrated in the top inset in Fig. 3.3. The $c(2\times 2)$ surface Brillouin zone is not only smaller and rotated by 45° relative to the $p(1\times 1)$ SBZ, but contains also an additional $\bar{\Gamma}_{c(2\times 2)}$ point of the second surface Brillouin zone inside the former $p(1\times 1)$ SBZ (former $\bar{M}_{p(1\times 1)}$ point). Bands corresponding to the $c(2\times 2)$ that are visible in the $\bar{\Gamma}$ point of the first SBZ should be also visible at $\bar{\Gamma}_{c(2\times 2)}$ of the second SBZ. As already mentioned, the underlying Cu substrate contributes to the signal as well. Adopting the easiest model of a superposition of signals from the $c(2\times 2)$ MnCu surface compound and an unchanged $p(1\times 1)$ Cu(001) substrate, emission from the 3-D copper Brillouin zone has to

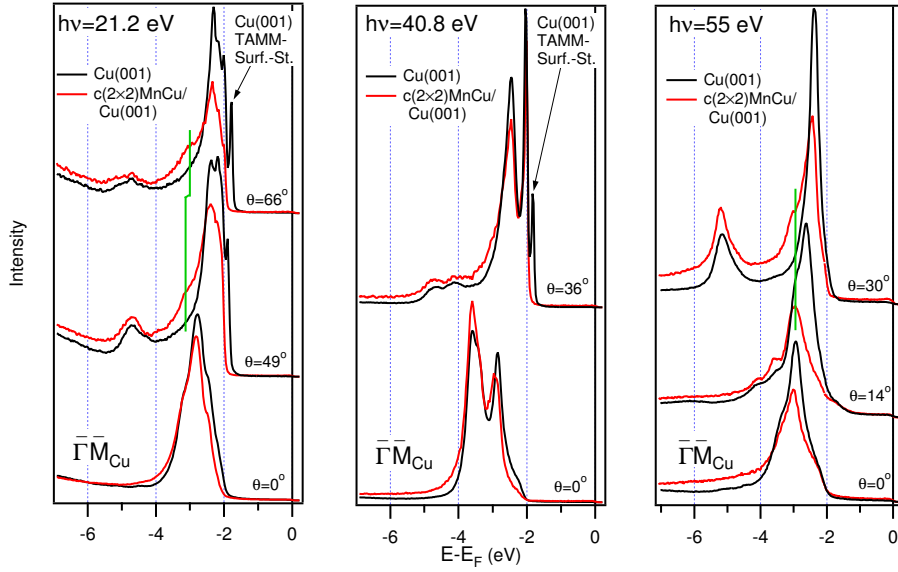


Figure 3.4: PE spectra measured in the $\bar{\Gamma}$ point of the first and the second $c(2\times 2)$ surface Brillouin zone for the photon energies of 21.2 eV, 40.8 eV, and 55 eV. With 21.2 eV and 55 eV the measurement in the $\bar{\Gamma}_{c(2\times 2)}$ point of the second SBZ is close to the Cu(001) 3-dimensional X point, where the band gap in the structure of Cu makes an observation of Mn-derived bands between 2 eV and 4 eV binding energy possible.

be considered. In Fig. 3.3 again the Cu(001) $\bar{\Gamma}XWK$ photoemission plane ($\bar{\Gamma}\bar{M}$ direction) is shown. While copper emissions in the first $\bar{\Gamma}$ point stem from initial states along the bulk $\bar{\Gamma}X$ direction, they originate in the $\bar{\Gamma}_{c(2\times 2)}$ point of the second SBZ from states along the bulk XW direction. The bottom inset of Fig. 3.3 shows results of a LCAO band-structure calculation along these high symmetry directions in copper. The manganese $3d$ spin majority band is expected by theory between 1.55 eV and 3.1 eV binding energy [Rad97a, Fab95, Ede00]. In order to avoid superposition by Cu-bulk derived features, the best measuring position is, therefore, close to the copper bulk X point, since the copper bands reveal there a gap. The X point can be reached with photon energies of 100 eV underneath the $\bar{\Gamma}$ point of the first, and with approx. 20 eV and an emission angle of nearly 80° or 55 eV and 30° underneath the $\bar{\Gamma}_{c(2\times 2)}$ point of the second surface Brillouin zone. The last two possibilities have two major advantages: A better resolution in energy and \vec{k} space due to lower photon energies and higher surface sensitivity due to (i) a kinetic energy of the photoelectrons close to the minimum in the electron mean free path and (ii) by the use of a large emission angle. Fig. 3.4 shows PE spectra taken at 21.2 eV, 55 eV and 40.8 eV photon energy (for comparison) in the $\bar{\Gamma}_{c(2\times 2)}$ point of the first and second surface Brillouin zone. For the normal emission spectra ($\bar{\Gamma}$ of the first SBZ, $\theta=0^\circ$) no differences are seen in the spectra of Cu(001) and $c(2\times 2)$ MnCu/Cu(001) either with direct PE ($h\nu=21.2, 40.8$ eV) or with resonant PE ($h\nu=55$ eV). In the spectra for the higher emission angles (close to the Cu 3-D X point along $\bar{\Gamma}\bar{M}_{p(1\times 1)}=\bar{\Gamma}\bar{X}\bar{\Gamma}_{c(2\times 2)}$) a shoulder

at 3.0 eV can be observed in addition to the copper-derived features¹. Since in clean copper this peak does not exist, it stems from the $c(2\times 2)$ MnCu overlayer and can be interpreted as at least part of the manganese 3d spin majority band when comparing it with the theoretical predictions. A further support of this interpretation can be derived from the dispersion of the new feature, that is very weak, as expected for localised d states. The fact that no 3.0 eV shoulder is observed in the spectra acquired with $h\nu=40.8$ eV (far away from the copper X point) confirms the above analysis. Notwithstanding, the resonant enhancement of the 3.0 eV feature can hardly be recognised in the on-resonance PE spectrum ($h\nu=55$ eV) as compared to the off-resonant one ($h\nu=21.2$ eV). It can be explained, however, by photoexcitation cross-section or final-state effects that can be quite different for the photon energies used. The large difference between the on- and off-resonance spectra is explained, however, by the necessity to compare spectra taken in equivalent points in the 3-D BZ. A weak dispersion of the new peak with the emission angles indicated by a displacement of the vertical bars is seen in the spectra taken with 21.2 eV photon energy. A least squares fit of the overlapping peaks reveals a dispersion from 3.00 eV close to $\bar{\Gamma}_{c(2\times 2)}$ ($\theta=66^\circ$) to 3.04 eV at $\theta=49^\circ$. The corresponding \vec{k} distance is approx. one third of the $c(2\times 2)$ SBZ. However, the error in determination of this shift is quite large, since the exact energy position and intensity of the neighbouring bulk feature is not known. RADER *et al.* [Rad97a] found a dispersion of the *unoccupied* states by 70 meV (half of the SBZ). In difference to the occupied peak dispersion, the unoccupied bands move toward the vacuum level when leaving the $\bar{\Gamma}$ point. Considering the peak position of the spin minority band at 1.85 eV above E_F [Rad97a], a total spin splitting of 4.85 eV can be calculated on the basis of the present results that is in better correspondence with the theoretical values [Rad97a, Ede00] than the 5.5 eV experimental value given in ref. [Rad97a].

Once established, this new method of determining the spin majority peak position can be applied to systems with higher concentration of Mn. FLORES *et al.* [Flo92] showed that a deposition of 1 ML of manganese onto a Cu(001) target heated to approx. 400 K results in a different LEED pattern, that was finally described by VAN DER KRAAN and VAN KEMPEN as a $pgg(4\times 2)$ structure [vdK95]. Fig. 3.5 shows the evaluation of the manganese-derived peak in the PE spectra measured at the $\bar{\Gamma}_{c(2\times 2)}$ point of the second SBZ for Cu(001), 0.5 ML $c(2\times 2)$ MnCu/Cu(001), and 1 ML $pgg(4\times 2)$ Mn/Cu(001) taken at a photon energy of 55 eV and an emission angle of 30° at the TGM 3 beamline of BESSY I in Berlin. The manganese-derived feature at 3.0 eV is unchanged. It seems that it becomes even more intense. This is, however, an artefact due to the intensity loss of the copper bulk emissions which are now superimposed by those of two

¹Note that the copper Tamm surface state that was discussed in sec. 2.3.3 is observed only for the sharp laboratory photon energies $h\nu=21.2$ eV and 40.8 eV but is not resolved in the synchrotron experiment with $h\nu=55$ eV. After Mn deposition the surface state totally disappears.

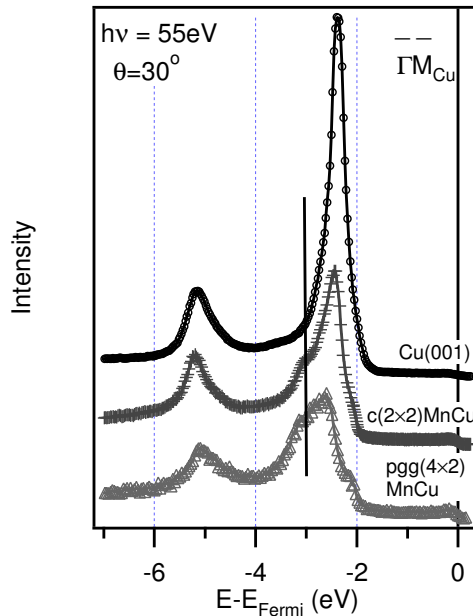


Figure 3.5: PE spectra for clean Cu(001) and for Mn coverages of 0.5 ML ($c(2\times 2)$) and 1 ML ($pgg(4\times 2)$) Mn/Cu(001) in the $\bar{\Gamma}_{c(2\times 2)}$ point of the second SBZ.

compound surface layers². Both theoretical and experimental studies [Rad97a] predict the growth of non-magnetic layers on top of the $c(2\times 2)$ structure. The increased coordination number of Mn should lead to a collapse of the magnetic exchange splitting. Emissions from such a non-magnetic Mn 3d band, however, are expected close to the Fermi edge but is not observed in the spectra presented in Fig. 3.5. EDER *et al.* predicted an antiferromagnetic coupling of two compound $c(2\times 2)$ layers as the most stable configuration with a second layer contribution at 2.0 eV binding energy [Ede00]. There is indeed a slight intensity enhancement at 2.0 eV in the bottom spectrum. Such an enhancement is already seen, however, in the $c(2\times 2)$ spectrum, and can, therefore, not be interpreted as a new feature. Still, we can not rule out the possibility of the two antiferromagnetic aligned $c(2\times 2)$ layers, since the predictions of this model are in much better agreement with the experimental data than those of a non-magnetic scenario. An antiferromagnetic coupling should reveal additional $c(2\times 2)$ spots as compared to the former $c(2\times 2)$ LEED pattern resulting in a $p(2\times 2)$ superstructure relative to Cu(001). Such a LEED pattern was *not* observed. On the other hand, there exist more possibilities for magnetic couplings of the layers, such as a non-collinear

²VAN DER KRAAN and VAN KEMPEN [vdK95] suggested the model of two compound layers, with both of them having mostly a $c(2\times 2)$ structure. The top layer, however, is slightly distorted giving rise to the $pgg(4\times 2)$ LEED pattern. In their STM investigation they observe only every second atom for either the $c(2\times 2)$ as well as the $pgg(4\times 2)$ structures interpreting this atom as a manganese atom in accordance with the large unusual buckling of the Mn atoms in the $c(2\times 2)$ surface compound. A recent theoretical study by WORTMANN *et al.* [Wor00] gives indication for an observation of the copper atoms in $c(2\times 2)$ exploiting of the intense spin minority surface state near \bar{X} .

antiferromagnetic overstructure with the local magnetic moments unchanged. As seen from the data presented here, for the case of the two compound overlayers in the $pgg(4\times 2)$ structure, the local magnetic order is not changed as compared to the $c(2\times 2)$ phase. Also in inverse photoemission data there is nearly no difference between the $c(2\times 2)$ and the $pgg(4\times 2)$ phase [Hay95, Rad97a]. Only at higher coverages with probably pure Mn layers or at least Mn islands indications for non-magnetic behaviour are observed.

3.2.4 Mn-induced magnetic surface states near the $\bar{X}_{p(1\times 1)}$ point

The following chapter will focus on the behaviour of the Cu(001) Shockley surface state near the $\bar{X}_{p(1\times 1)}$ point of the surface Brillouin zone after Mn deposition. The sampled area in \vec{k} -space is shown in Fig. 3.6(b) together with the photoemission spectra of Cu(001) and $c(2\times 2)$ MnCu/Cu(001) taken with $h\nu=32$ eV in the top part of Fig. 3.6(a). Although the PE spectra in Fig. 3.1 do not reveal pronounced differences between Cu(001) and $c(2\times 2)$ MnCu/Cu(001), a detailed analysis of spectra taken close to the $\bar{X}_{p(1\times 1)}$ -point of the SBZ exhibits dramatic changes. In clean Cu(001) the copper sp bulk band (labelled α) does not cross the Fermi energy³, the weak feature (β) stems from the Shockley state. After formation of the $c(2\times 2)$ MnCu/Cu(001) surface three main features can be observed. One shows a very similar dispersion as the copper bulk band and is, hence, assigned to the slightly changed copper bulk band (label α). The other two features (β and γ), on the other hand, are identified as Mn-induced states. Since copper does not reveal any bands in this energy region with such a dispersion, contributions from the Cu-substrate in form of direct as well as umklapp-processes can be ruled out. There are several possibilities to check the surface-state character of these new states. Two of them are shown in Fig. 3.6(a): (*i*) deposition of an adlayer realised by evaporation of 2 ML Cu, and (*ii*) variation of the photon energy. Often reactive gases such as oxygen or carbon monoxide are used to quench surface-derived emission. However, reactive gases can drastically change the surface chemistry and bonding. Therefore, copper overlayers were used here. As it is evident from the analysis of the spectra taken with $h\nu=32$ eV, deposition of 2 ML of Cu leads (*i*) to a shift of the copper bulk band of $c(2\times 2)$ MnCu back to its position in Cu(001), while (*ii*) feature β remains unaffected. The third peak (γ) is quenched by the Cu adlayer. The second possibility to prove a 2-D character of the states is a variation of the photon energy. Signals of 3-D states are usually affected by a variation of photon energy since given values of \vec{k}_{\parallel} correspond now to different points in \vec{k} -space (another k_{\perp} position), while 2-D states (surface states) do not depend on k_{\perp} . In the spectra taken at a photon energy of 65 eV (Fig. 3.6[a]), peak positions are similar to those in the spectra

³With a photon energy of 32 eV one still measures in the neck of the dog bone of the Fermi surface, see chapter 2.3.2 and 2.4.

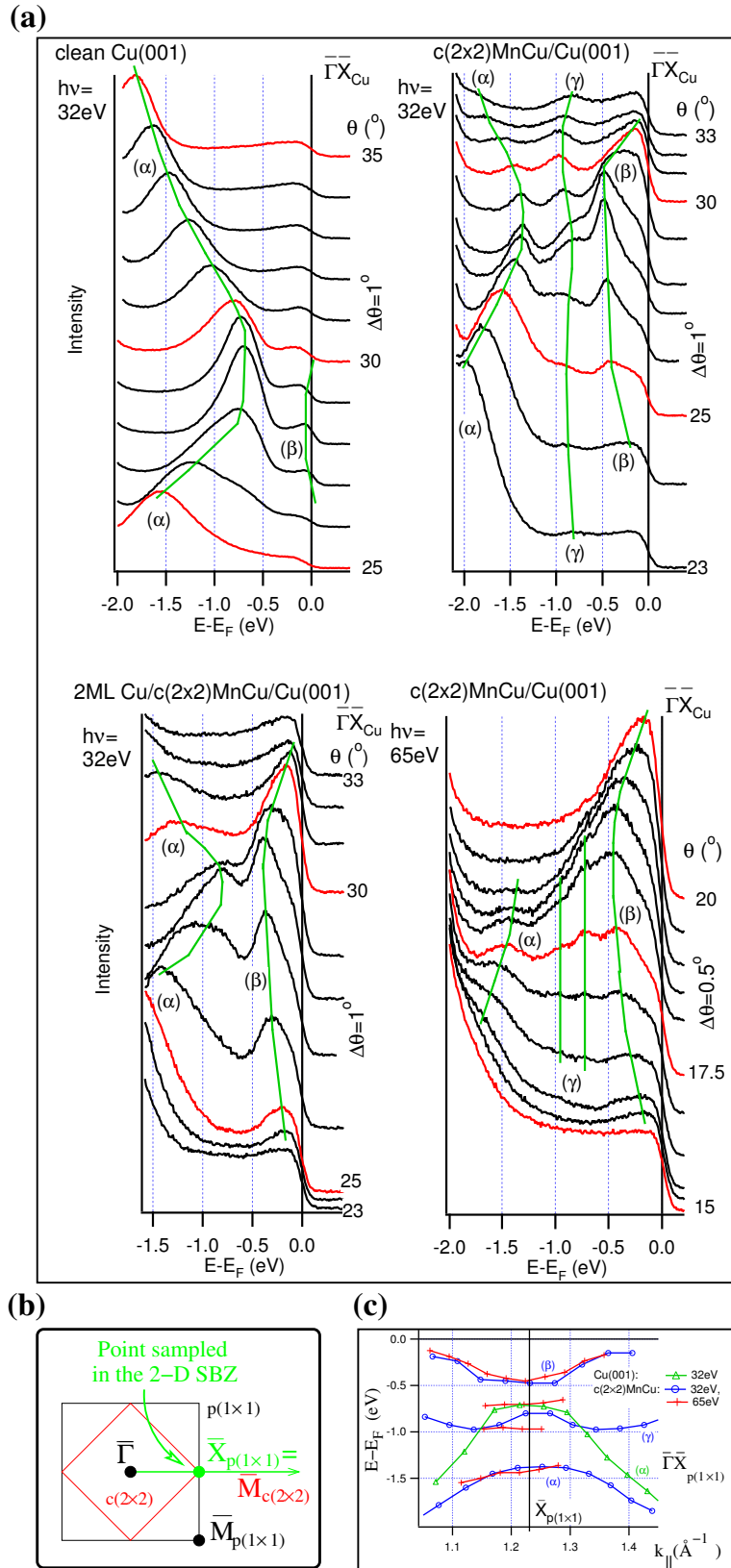


Figure 3.6: **(a)**: Photoemission spectra of Cu(001), $c(2\times 2)$ MnCu/Cu(001), and 2 ML Cu/ $c(2\times 2)$ MnCu/Cu(001) taken at $h\nu=32$ eV as well as the spectra taken at $h\nu=65$ eV near $\bar{X}_{p(1\times 1)}$, **(b)**: comparison of the $p(1\times 1)$ and the $c(2\times 2)$ SBZ, **(c)**: dispersion in Cu(001) and $c(2\times 2)$ MnCu/Cu(001) near $\bar{X}_{p(1\times 1)}$.

obtained with 32 eV, although peak intensities have changed⁴. The measured dispersions at different $h\nu$ are shown in Fig. 3.6(c). In the spectra taken at 65 eV photon energy peak γ is split into two features. A possible explanation of this phenomenon is the better resolution of the SU8 beamline at LURE where the $h\nu=65$ eV spectra were taken as compared to the SU6 beamline (spectra taken at $h\nu=32$ eV). Figs. 3.7(a) and (b) show the band dispersions of Cu(001) and $c(2\times 2)$ MnCu/Cu(001) at a photon energy of 21.2 eV and taken with the Scienta 200 spectrometer in a larger \vec{k} range. Logarithmic intensities are shown in a colour scale as a function of E_B and k_{\parallel} . For comparison, the dispersion of the Cu(001) bands are indicated in the $c(2\times 2)$ MnCu image by white lines. As seen in Fig. 3.7(b) the γ band crosses the Fermi energy at a large emission angle corresponding to $k_{\parallel}=1.65 \text{ \AA}^{-1}$ that is located in the third surface Brillouin zone. The dispersion toward $\bar{\Gamma}$ cannot be followed due to the high intensity of the copper bulk bands masking the Mn-derived features. Results of a LKKR simulation of photoemission spectra analysis for the $c(2\times 2)$ MnCu(001) surface are shown in Fig. 3.7(c). All experimental details can be recognised also in the calculated data for the $c(2\times 2)$ MnCu/Cu(001) surface. The theoretically predicted bands are only slightly shifted as compared to the experimental ones. To interpret the results of the calculations, part (d) of Fig. 3.7 shows the layer, atom, and spin resolved density of states at the Mn site for two emission angles, 39° and 46° , respectively. Vertical broken lines denote peak positions of the maxima observed in the photoemission calculation of Fig. 3.7 (c). Using the same notation as in the experiment, we can conclude the following: feature α corresponds to a hybridised pd band of spin up (majority) character, β is a spin up (majority) state with slightly larger d than p character. Since in the LDOS of Cu surface atom (not shown) the same peaks of nearly the same intensity are found, a strong Mn-Cu hybridisation of the corresponding states can be concluded. The γ feature is characteristic for the LDOS at the Mn surface sites and correspond to spin down (minority) and d character.

A more detailed analysis was carried out for the photoemission spectra taken at 32 eV photon energy. Corresponding to the experimental data presented in Fig. 3.6(a), Fig. 3.8 shows calculated photoemission spectra of Cu(001) (left) and $c(2\times 2)$ MnCu/Cu(001) (right), respectively⁵. Apart from additional features between 1 eV and 2 eV that are mainly due to bulk Cu-derived d states found at slightly different energy positions than in the experiment due to final state effects, the observed experimental details are in accordance with the theory. Corresponding states at the Mn and the Cu sites of the outermost atomic surface layer are shown in Fig. 3.9(a) for several emission angles. The former discussed behaviour of features β and γ can be observed here: While β is a MnCu hybrid state, γ is

⁴The $\bar{X}_{p(1\times 1)}$ point of the SBZ is reached at 18° using a photon energy of 65 eV.

⁵Note, that Cu(001) was calculated in a $c(2\times 2)$ CuCu structure in order to be able to compare directly the results with $c(2\times 2)$ MnCu. Afterwards it was checked that the $p(1\times 1)$ structure calculation resulted in exactly the same PE spectra.

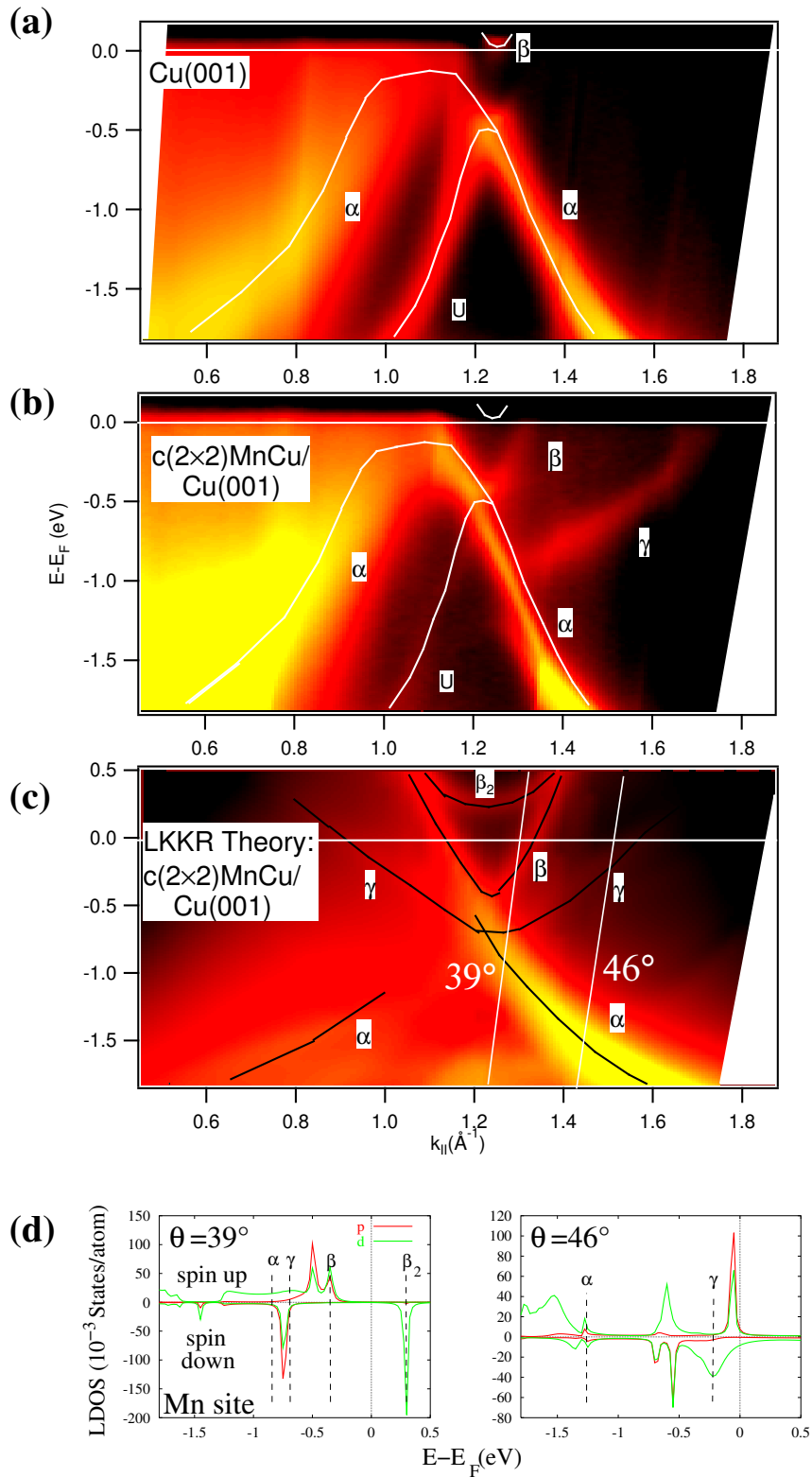


Figure 3.7: Experimental band dispersion of (a): Cu(001) and (b): $c(2 \times 2)$ MnCu/Cu(001) around $\bar{X}_{p(1 \times 1)}$ ($h\nu = 21.2$ eV). Part (c) shows the LKKR calculated photoemission intensity for $c(2 \times 2)$ MnCu. The LDOS along the straight lines of the calculated intensities corresponding to 39° and 46° emission angles are shown in (d).

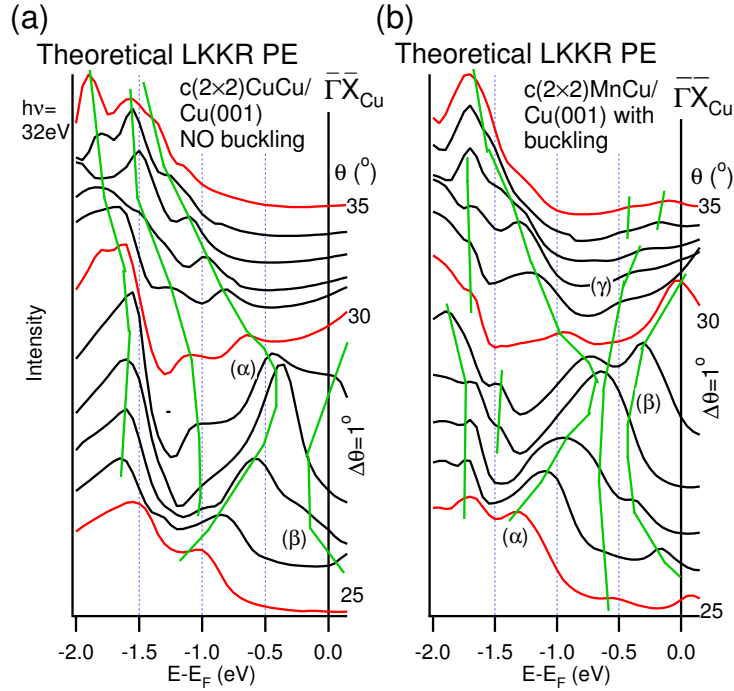


Figure 3.8: Theoretical LKKR one-step PE spectra calculated for (a) Cu(001) and (b) the buckled $c(2\times 2)$ MnCu/Cu(001) surfaces ($h\nu=32$ eV), respectively.

localised only at the Mn atom. Light lines in Fig. 3.9 (a) are used for p , black ones for d character. Since PE signals stems not only from the surface, but also from underlying layers, contributions of these layers to the spectra cannot be neglected. Part (b) of Fig. 3.9 shows the LDOS for different layers in the area of the Mn sites (Mn on the top of the surface, Cu atoms in a four-fold hollow site [odd layers] or Cu atoms [even layers] underneath the surface). The energy positions of the peaks in the calculated photoemission spectrum for this emission angle (31°) are shown by vertical dotted lines: feature α , β , and γ have their origin at the outermost surface layer.

The above experimental findings were recently reported by HUTTEL *et al.* and theoretically explained based on the surface Green's-function matching-technique [Hut01]. At the $\bar{X}_{p(1\times 1)}$ -point peak α was assigned to a superposition of states of both spin up and down-character localised mainly within the surface layer and the two layers underneath. At a k_{\parallel} position corresponding to only 0.16 \AA^{-1} away from the $\bar{X}_{p(1\times 1)}$ -point these states, however, should lose totally their surface localisation. Peak β is interpreted as a spin down surface state and peak γ as the reminiscent contribution of the Cu(001) sp band. It is obvious, however, that this interpretation cannot be correct since peak γ reveal an electron like dispersion while the Cu sp bulk band dispersion behaves hole-like. Since the interpretation of all three peaks are in contradiction to our findings, the physical origin of the new states has been investigated in more detail.

It was concluded that there exist different spin states in the vicinity of the $\bar{X}_{p(1\times 1)}$ -

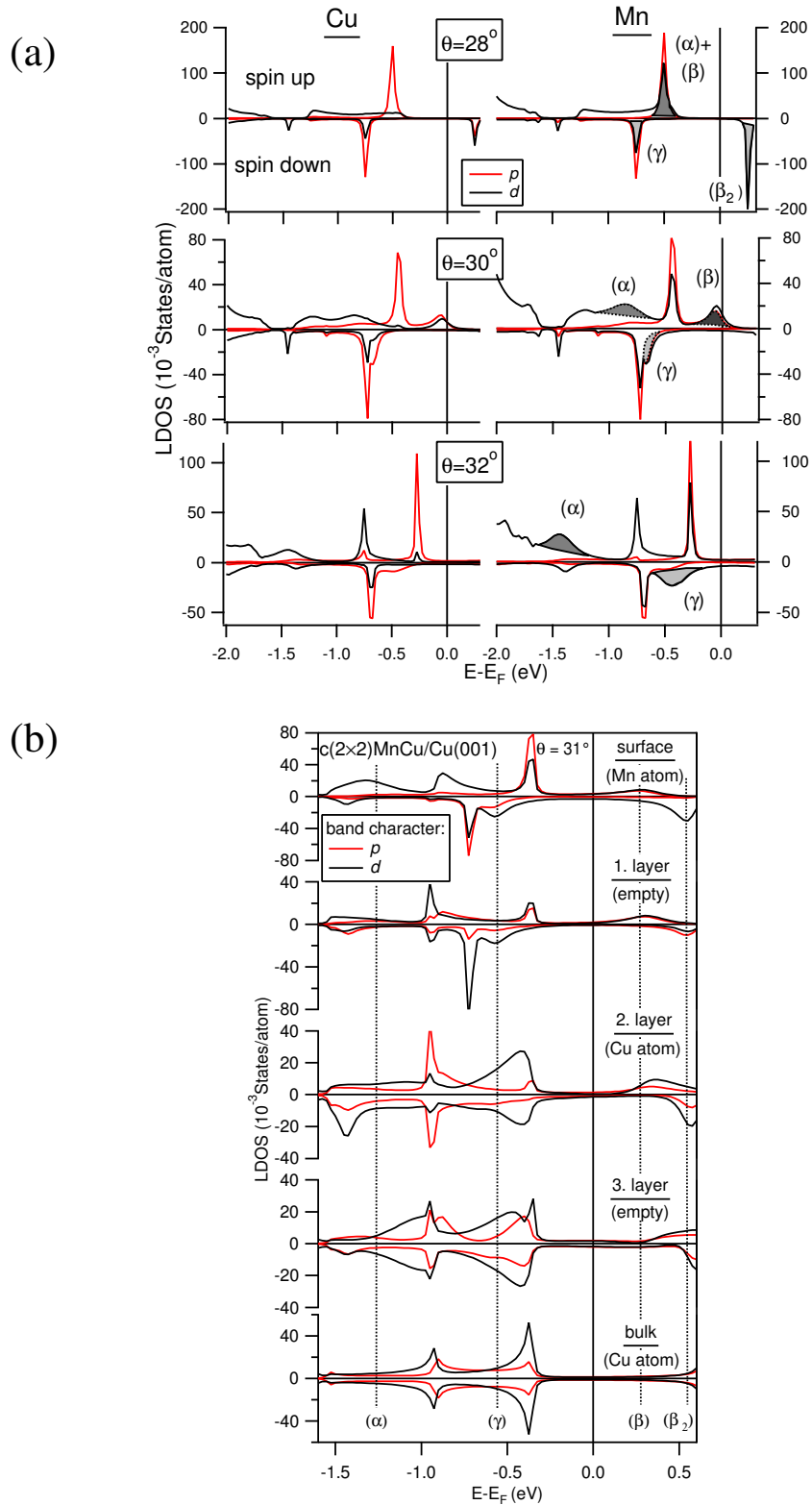


Figure 3.9: Layer-resolved density of states (light lines denote p , black lines d character) (a): for the top surface layer for the Cu and Mn site of the $c(2\times 2)\text{MnCu}/\text{Cu}(001)$ with a Mn buckling of 0.3 \AA for different emission angles, (b): at and below the Mn site in different layers at $\theta=31^\circ$. The shaded areas and dotted lines are used to indicate the positions of peaks of highest intensity in the calculated PE spectra, respectively.

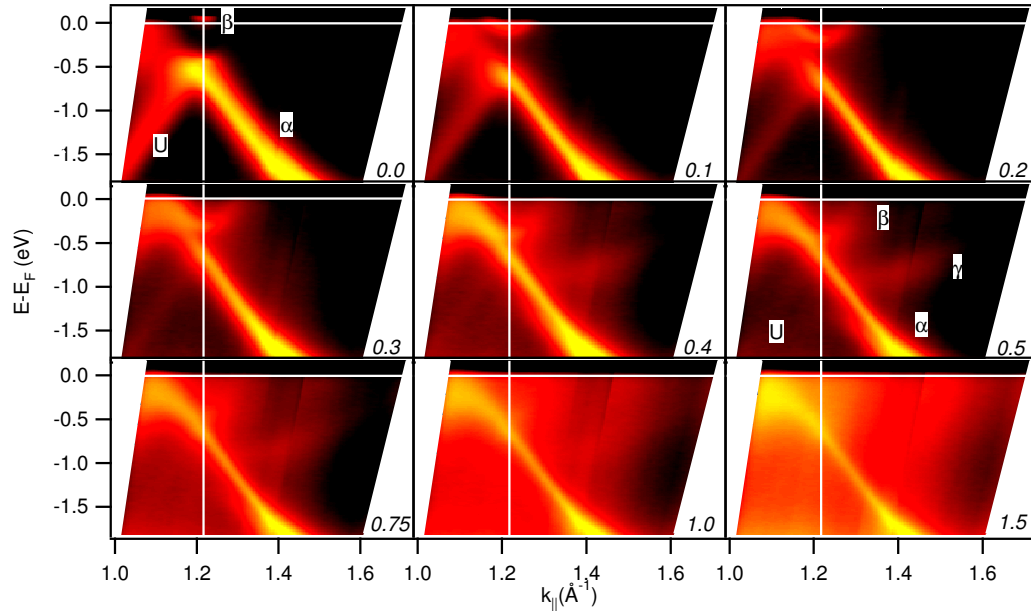


Figure 3.10: Dispersion of the bands near the $\bar{X}_{p(1\times 1)}$ point for different manganese coverages of Cu(001). The logarithmic intensity is presented with a colour scale to strengthen minor features. The $\bar{X}_{p(1\times 1)}$ -position is indicated by a vertical white line.

point in the SBZ and, for the first time, an occupied spin down state (spin minority) of the $c(2\times 2)$ MnCu surface compound was found. In the following the nature of the states are probed by experimental techniques. To this aim different manganese coverages between 0 and 1 ML were prepared consecutively. Fig. 3.10 shows the dispersion of bands near $\bar{X}_{p(1\times 1)}$ as a function of coverage. Logarithmic intensities are presented in a colour scale. The vertical white lines denote the $\bar{X}_{p(1\times 1)}$ position. The following details can be observed:

- The Cu(001) umklapp-band U loses its intensity with increasing Mn coverages. At a coverage corresponding to 0.4 ML Mn it disappears. The reason is the symmetry change from $p(1\times 1)$ to $c(2\times 2)$ and, hence, an elimination of the umklapp-condition.
- The copper sp bulk band α is only slightly affected by the Mn coverage. Upon Mn coverage and at large \vec{k}_{\parallel} values a slight shift to higher binding energies can be observed that was discussed already before.
- With increasing Mn coverage the Cu(001) Shockley state β moves continuously to higher binding energies. At a Mn coverage of 0.5 ML corresponding to the $c(2\times 2)$ MnCu surface compound it hybridises with the sp bulk band. For Mn coverages exceeding 1 ML the parabola-like dispersion typical for surface states is not longer visible.
- The new spin minority feature γ is only seen between 0.4 and 0.75 ML Mn coverage, indicating that it is related to the quality of the $c(2\times 2)$ structure.

This finding rules out the interpretation by HUTTEL *et al.* who claimed this band to be a reminiscence of the Cu(001) *sp* band [Hut01].

Now the behaviour of the Cu(001) Shockley surface state will be discussed in detail. The image state observed by inverse photoemission for the pure Cu(001) surface is found to be shifted by 450 meV to lower energies upon formation of the $c(2\times 2)$ MnCu surface compound [Rad97a, Hay95]. This value coincides exactly with the work function change that has been experimentally measured by photoemission [Bin82]. The latter is expected, since image states are always pinned to the vacuum level. Following the explanation given by SMITH [Smi85] there may exist an additional ($n=0$) Shockley surface state at lower energy than the lowest state ($n=1$) of the image-potential Rydberg series. Such a state appears only in Shockley-inverted gaps and is localised close to or particularly within the outermost atomic surface layer, while image states are found several angstroms underneath the surface in the vacuum region. The considered Cu- $\bar{X}_{p(1\times 1)}$ surface state was successfully described by this approach [Smi85].

Adsorption of alkali metals on clean surfaces lowers the work function. However, only an energy shift of 20% of the work function change was observed for the Shockley state [Lin80]. This can be understood by considering the reasons of a work function change: There are mainly two mechanism possible for such a phenomenon: (*i*) an alteration of the surface dipole, or (*ii*) a variation of the Fermi level position. For alkali adsorption on noble metal surfaces a strong drop of the surface dipole is expected due to the positive alkali ion cores that remain as a result of the charge transfer from the alkali atoms to the substrate. This work function change would strongly affect the image state, while for the Shockley state at least part of the effect is screened by conduction electrons. On the other hand, changes of the Fermi level position should affect all states in a same way. Particularly almost identical shifts for the $n=1$ image and the $n=0$ Shockley state may be expected. For the $c(2\times 2)$ MnCu system magnetism was found to be the reason for the work function change [Rad97a], that shifts the Fermi level but should not affect the surface dipole that are similar for (001) surfaces of Cu and Mn metals. The nearly identical energy shift of the Shockley state observed in the present work (430 meV) and of the image state observed by inverse photoemission [Rad97a, Hay95] as well as the work function change [Bin82] (450 meV) support this point of view. Fig. 3.11 compares the energy shift of the vertex of the Shockley state derived parabolic band observed in PE spectra taken at 21.2 eV photon energy (Fig. 3.10) and the work function change taken from [Bin82]. Since the presented data were not measured spin-resolved, the correct spin polarisation can only be obtained from theory. As explained, the theoretical results of the present study are not in agreement with the interpretation given in [Hut01]. One of the conclusions of [Hut01] is an assignment of one observed feature to the spin-down component of the MnCu surface state. However, if the Shockley surface state is split, its spin up part component should be found at *higher* binding energy. This would be only possible on basis of their data, if feature γ is

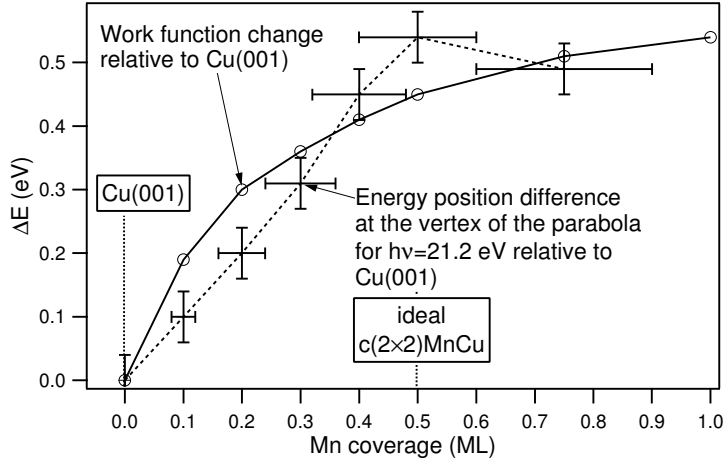


Figure 3.11: Comparison of energy shift observed for the bottom of the surface state derived band and work function changes [Bin82] as a function of Mn coverage on Cu(001).

considered to be the spin up band. Notwithstanding γ was assigned to the bulk band [Hut01]. On the other hand, our experimental findings show that features β and γ have different origin. Feature β changes continuously with coverage, while γ is only observed between 0.4 and 0.75 ML Mn coverage. Assuming the theoretical data presented by HUTTEL *et al.* to be correct, there remains a last possibility to reconcile them with the experiment: The Shockley surface state is *not* spin splitted. It moves in energy with the work function change. Between 0.4 and 0.75 ML it becomes spin split with β as the spin down component and γ as the spin up part. Nevertheless, this last possibility can be excluded by the very different dispersions of β and γ that should be similar for both components of a spin split surface state.

3.2.5 Quenching of the Cu(001) Tamm state upon Mn deposition

Another well known Cu(001) surface state is found in the region of the $\bar{M}_p(1\times 1)$ point of the SBZ. Fig. 3.12 displays the Tamm surface state taken at a photon energy of 21.2 eV at $\theta=60^\circ$ for clean Cu(001), a clean $c(2\times 2)$ surface, and a $c(2\times 2)$ surface exposed for 15 hours to a pressure of 6×10^{-11} mbar. As it can be seen in the inset of Fig. 3.12, where the intensity of the surface state is displayed normalised to the surface state signal of clean Cu(001); the surface state is already totally quenched at 0.2 ML Mn coverage. This is expected for the quenching of a “dangling bond state” at the Cu(001) surface since this state is localised only in the top surface layer, while the former described Shockley surface state penetrates deeper into the solid. It is interesting to note that after some hours exposed to residual gases a shoulder at the same energy position as the Tamm peak appears in the spectra and the extra $c(2\times 2)$ spots vanish in the

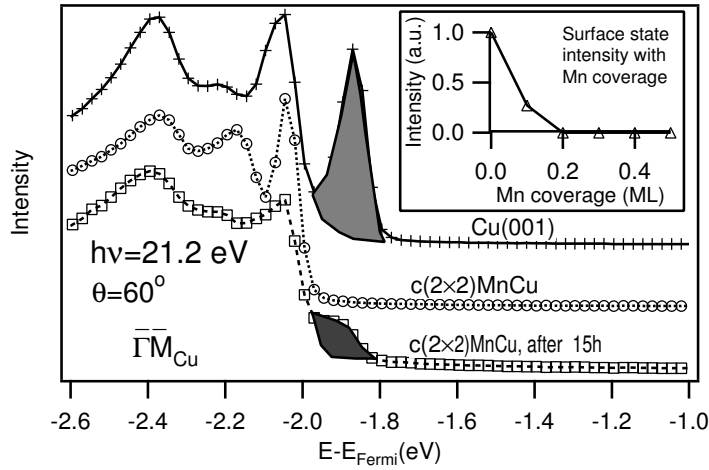


Figure 3.12: Copper Tamm surface state in the region near $\bar{M}_p(1\times 1)$ for Cu(001) and after deposition of 0.5 ML Mn. Inset: decrease of Tamm surface state intensity with coverage normalised to the surface state signal from clean Cu(001).

LEED pattern. Possibilities for such a behaviour could be either a metastability of the surface compound caused by a transport of Mn into the copper bulk matrix or contamination induced clustering of the manganese leaving parts of the copper substrate uncovered so that the surface state reappears. Further investigations of this phenomenon were not carried out.

3.3 Fermi-surface changes after formation of the $c(2\times 2)$ structure

Band-structure investigations along the high symmetry directions give already a deep insight into the electronic structure. Another very important point for the characterisation of the electronic structure are Fermi surface measurements. Additionally, such experiments are a good tool to follow the dispersion in low symmetry directions. Figs. 3.13 (a) and (b) compare Fermi surface cuts taken with a photon energy of 21.2 eV for Cu(001) and $c(2\times 2)$ MnCu/Cu(001). The cuts were measured in an azimuthal angle range of 90° and corresponding replica are shown for the other three quadrants to facilitate the presentation. Like in the band-dispersion the main copper derived structures are preserved in the Fermi surface after deposition of Mn. There appear, however, some additional features that are emphasised in Figs. 3.13 (c) to (f). The Shockley surface state region of clean Cu(001) and $c(2\times 2)$ MnCu/Cu(001) in Figs. 3.13 (c) and (d) is probed with a photon energy of 23.1 eV in order to use the enhanced surface state intensity. To strengthen the details again a logarithmic colour scale is used. While in pure Cu(001) the Fermi energy is only touched by the electronic bands, in $c(2\times 2)$ MnCu an elliptic Fermi surface is observed. From the non-circular shape and together with the parabolic dispersion appearing at least in $\bar{\Gamma}\bar{X}_p(1\times 1)$ direc-

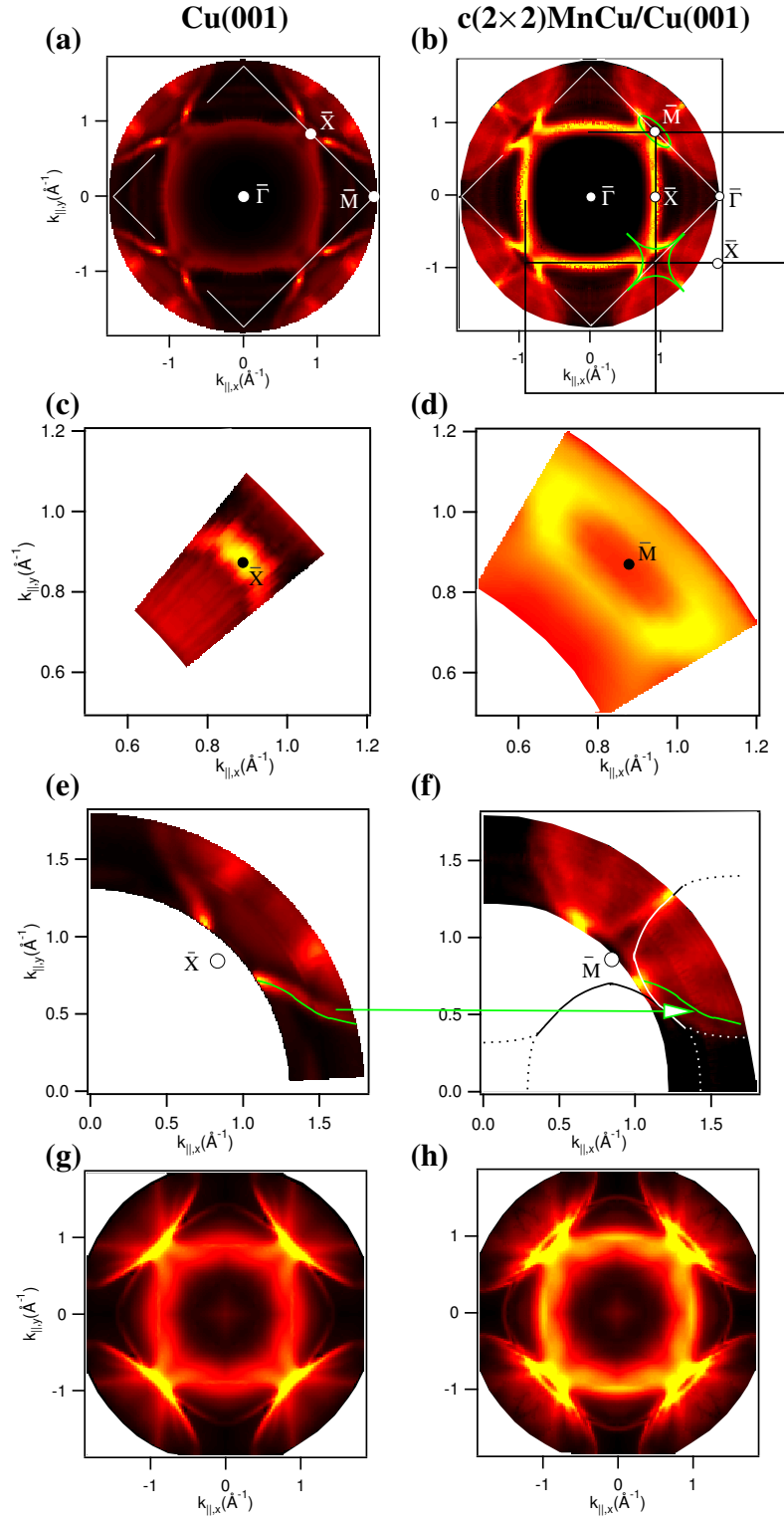


Figure 3.13: Experimental Fermi-surface cuts of (a): Cu(001) and (b): $c(2 \times 2)$ MnCu/Cu(001) as measured with $h\nu = 21.2$ eV; the Shockley-state region taken with a photon energy of 23.1 eV of (c): Cu(001) and (d): $c(2 \times 2)$ MnCu; the Mn spin-minority state region of (e): Cu(001) and (f): $c(2 \times 2)$ MnCu; the calculated Fermi-surface cuts for a photon energy of 21.2 eV for (g): Cu(001) and (h): $c(2 \times 2)$ MnCu. High symmetry points $\bar{\Gamma}$, \bar{M} , \bar{X} are given for their respective surface Brillouin zones: $p(1 \times 1)$ for Cu(001) and $c(2 \times 2)$ for the MnCu surface compound.

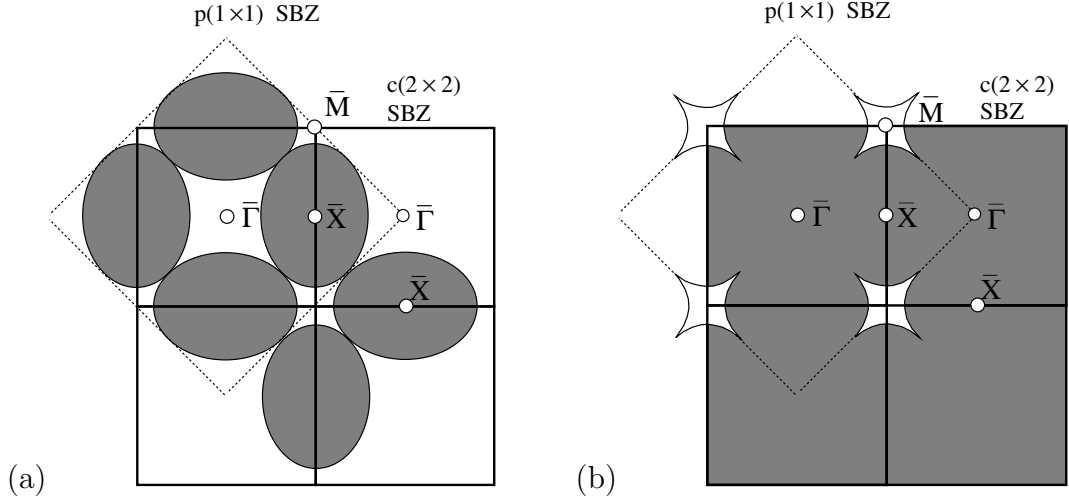


Figure 3.14: Possible models for the spin minority Fermi surface induced by the Mn: (a) model related to the experimentally derived ellipse structure, (b) two casually linked Fermi surface features: One reveals the star-like spin minority derived Fermi surface, and (beginning from the tip of the star) the other one (not shown) is caused by a spin separation of the Cu bulk band induced by the Mn magnetic field. In this presentation unoccupied parts of the SBZ are shaded.

tion (see Fig. 3.10) different effective masses in $\bar{\Gamma}\bar{X}_{p(1\times 1)}$ and $\bar{X}\bar{M}_{p(1\times 1)}$ direction are concluded. The Fermi surfaces obtained from the photoemission LKKR calculations shown in Figs. 3.13 (g) and (h) are in agreement with the experimental Fermi surfaces, particularly in the Shockley surface state region. Figs. 3.13 (e) and (f) emphasise the experimental Fermi surface region of the spin minority surface state. The shape of this Fermi surface feature is star-like or even again elliptic, however, now around the $\bar{X}_{c(2\times 2)}$ points of the second SBZ. The experimental data do not allow to distinguish between these two possibilities. When assuming the new feature to be elliptic, backfolding of this spin minority Fermi surface into the first surface Brillouin zone as shown in Fig. 3.14(a) reveal the spin minority band to be occupied not only around $\bar{X}_{p(1\times 1)}=\bar{M}_{c(2\times 2)}$ but also around $\bar{\Gamma}$. In this presentation unoccupied parts of the SBZ are shaded. The remaining question is, why no bands were found around $\bar{\Gamma}$ in the first Brillouin zone. One reason may be Brillouin zone selection rules as discovered by SHIRLEY *et al.* for graphite [Shi95]: Some bands that are very intense in the first surface Brillouin zone are extremely weak in the second one and vice versa. In graphite this behaviour depends on the band symmetry (σ or π). Another possibility is indicated in Fig. 3.14(b): If the part of the ellipse, which is parallel to the belly structure (dotted lines in Fig. 3.13[f]), does not belong to the spin minority Fermi surface, the Fermi surface will be reduced to a star-like shaped feature and the bands will be only occupied close to $\bar{X}_{p(1\times 1)}$. The reason for the dotted lines in Fig. 3.13(f) could be spin-split copper bulk bands induced by the high magnetic moment of the Mn atoms. These split bulk bands would cross the Fermi surface

at slightly different \vec{k} values. In the spectra shown in Fig. 3.7 an influence to the copper bulk band was observed. However, such an influence should also be seen for other regions of the belly structure. Since no changes were observed there, we assign the Fermi surface with the elliptic shape to the spin minority bands and attribute the absence of the signal near $\bar{\Gamma}$ to other phenomena. Among such phenomena could be, for example, a hybridisation of Mn derived states with unoccupied Cu-derived bands that follow still the $p(1\times 1)$ symmetry.

3.4 Conclusions

A new method for the determination of the Mn spin majority occupied band of the $c(2\times 2)\text{MnCu}/\text{Cu}(001)$ surface compound based on the symmetry of the surface Brillouin zone was presented. At the $\bar{\Gamma}$ point of the second SBZ this band was detected at 3.0 eV binding energy. Considering the inverse photoemission data of RADER *et al.* [Rad97a] a total exchange splitting of 4.85 eV is concluded. For two compound layers in the $pgg(4\times 2)$ structure the same value of exchange splitting was observed giving evidence that the Mn atoms are still in a high spin ground state.

The Shockley surface state of Cu(001) is maintained after Mn deposition with a binding energy shift proportional to the change of work function. The latter is tracked by the surface potential and affects image and Shockley states in almost the same manner.

Furthermore, an occupied spin minority band was found close to the $\bar{X}_{p(1\times 1)}$ point of the SBZ. The measured Fermi surface of this feature is elliptic shaped and localised around the $\bar{X}_{c(2\times 2)}$ points in the second SBZ. An occupation of the spin minority band at the $\bar{\Gamma}$ point was not observed.

Chapter 4

Growth and magnetic properties of Mn/Cu multilayers

4.1 Aim of study of Mn/Cu multilayers

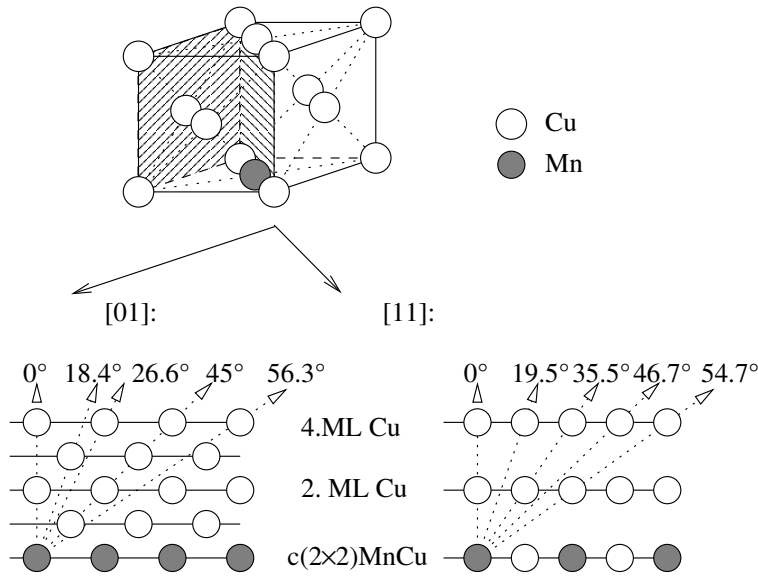
It is of high interest to study the effects of the high magnetic moment carried by the manganese atoms (up to $5\mu_B$ per atom) to surrounding atoms. In contrast to the following elements in the periodic table (Fe, Co, and Ni) Mn, as a bulk material, does not reveal ferromagnetic order. The strong overlapping of the $3d$ orbitals of neighbouring Mn atoms suppresses the macroscopic magnetic moment in Mn metal. The interesting question is now, what happens, when the interatomic Mn-Mn distance is increased in compounds with non-magnetic materials, as for example, Cu. This can be realised by inserting Mn atoms as impurities in a glass-like structures [Owe56, vdM85] or by synthesis of ordered MnCu compounds. Unfortunately, manganese and copper do not form stable bulk compounds [Mas92]. On the other hand it is known, that half a monolayer of Mn on Cu(001) forms an ordered $c(2\times 2)$ surface structure [Flo92, Wut93c]. If Cu grows epitaxially on top of such a surface compound in a normal Cu(001) stacking sequence, further $c(2\times 2)$ MnCu overlayers could be grown and a quasi-bulk system could be created.

4.2 Synthesis of MnCu/Cu Multilayers

4.2.1 Growth of Cu on $c(2\times 2)$ MnCu/Cu(001)

Growth of Mn on Cu is very well studied by Auger electron spectroscopy (AES) and LEED [Bin82], dynamic LEED [Flo92], X-ray photoelectron diffraction in forward scattering [Ege90] and backward scattering modes [Too96], as well as by scanning tunnelling microscopy [vdK95, Noh94, Wut96, Flo92]. This large number of studies was motivated on the unusual behaviour of the Mn/Cu(001)

(a) Without Mn corrugation



(b) With Mn corrugation of 0.3 Å

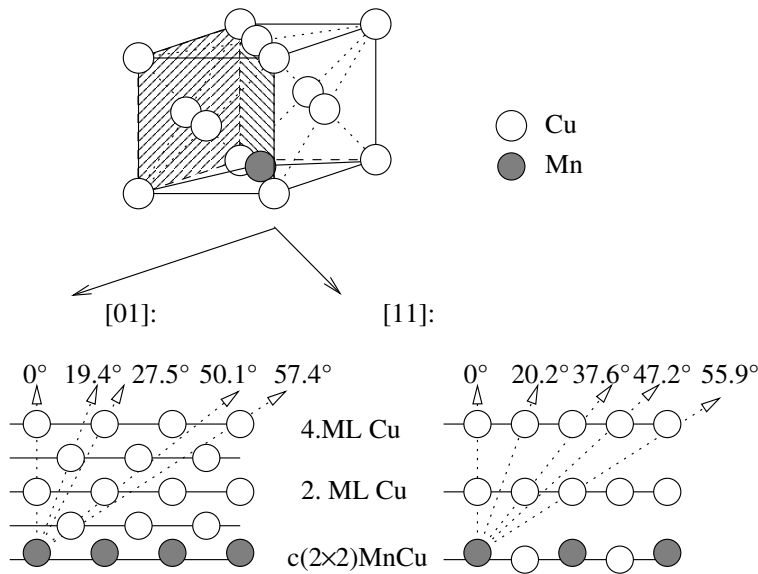


Figure 4.1: Schematic diagram of PED from copper grown on unbuckled (a) and buckled (b) $c(2 \times 2)\text{MnCu}/\text{Cu}(001)$ surface in both high symmetry directions, [01] and [11], respectively.

formation ¹.

In the present work, photoelectron diffraction (PED) together with LEED was used to study the growth of Cu overlayers on $c(2 \times 2)\text{MnCu}/\text{Cu}(001)$. The experiment was carried out at the SU 7 beamline of the Laboratoire pour l'Utilisation du

¹A more detailed description of the growth of the Mn/Cu(001) system can be found in Appendix A.

Rayonnement Electromagnétique (L.U.R.E.) in Orsay/France, using the Spanish-French Station PES 2. The copper deposition rate was calibrated with an Al substrate covered with some manganese to establish similar conditions as for the growth of Cu on MnCu. The Mn and Cu core-level intensities were analysed taking into account layer stacking and tooling ratios as explained in a previous work [Sch97] and the deposition rate was tuned to approx. one monolayer per minute. At low coverages, the background intensity of the LEED pattern increased with copper deposition. Additionally all LEED spots become broader and a weakening of the $c(2\times 2)$ superstructure occurred. The superstructure disappeared after adsorption of approximately 4 ML. At further copper deposition the LEED pattern showed a $p(1\times 1)$ overstructure. It was worse than the pure Cu(001) pattern, but still with well visible spots and relatively low background intensity indicating reasonable well long-range order at the surface.

For the determination of the short-range order, PED was applied in forward scattering geometry. A photon energy of 470 eV was used in order to obtain predominantly forward scattered electrons (kinetic energies higher than 400 eV) at reasonable counting rates since the photon flux decreases with increasing photon energy due to the beamline performance. This was also the reason to use the $3p$ core levels of Mn and Cu that are less intense than the deeper lying $2p$ core levels of both elements. A further cause was that the binding energies of the Mn and Cu $3p$ core levels lie in the same energy region, but are well separated from each other. Therefore effects like the background intensity distribution are nearly identical in both cases, but no photoelectron diffraction mixing is monitored. Finally, it should be mentioned that in the energy region around 400 eV kinetic energy no Auger emissions appear. The Cu and Mn $3p$ core levels were measured and their peak positions were determined. Photoelectron diffraction was carried out by measuring the intensity at the kinetic energies corresponding to the maxima of these peaks, I_p , and - for further normalisation - the background intensity, I_{20} , at approximately 20 eV higher kinetic energy. The normalisation was done to the characteristic form $(I_p - I_{20})/I_{20}$, that will be used in the following in all presentations such as polar scans and 2-dimensional intensity distribution plots (for further details of the normalisation process see [Sch97]).

A structural model of a fcc-like copper film epitaxially grown on the $c(2\times 2)$ MnCu surface is presented in Fig. 4.1. The theoretical positions of the PED intensity enhancement of the Mn emission due to the overlayer atom diffraction are displayed for two high symmetry directions for unbuckled (a) and buckled (b) $c(2\times 2)$ MnCu underneath 4 copper monolayers, respectively (for emission angles lower than 60° only). A 0.3 Å corrugation of the manganese at the interface was assumed according to [Wut93c].

In order to deal with clean samples, all mentioned overlayer stacks were grown on a clean Cu(001) substrate. For all samples, not only PED but also normal photoemission as well as soft X-ray absorption measurements were performed in order to characterise them as well as possible. Results obtained by last two tech-

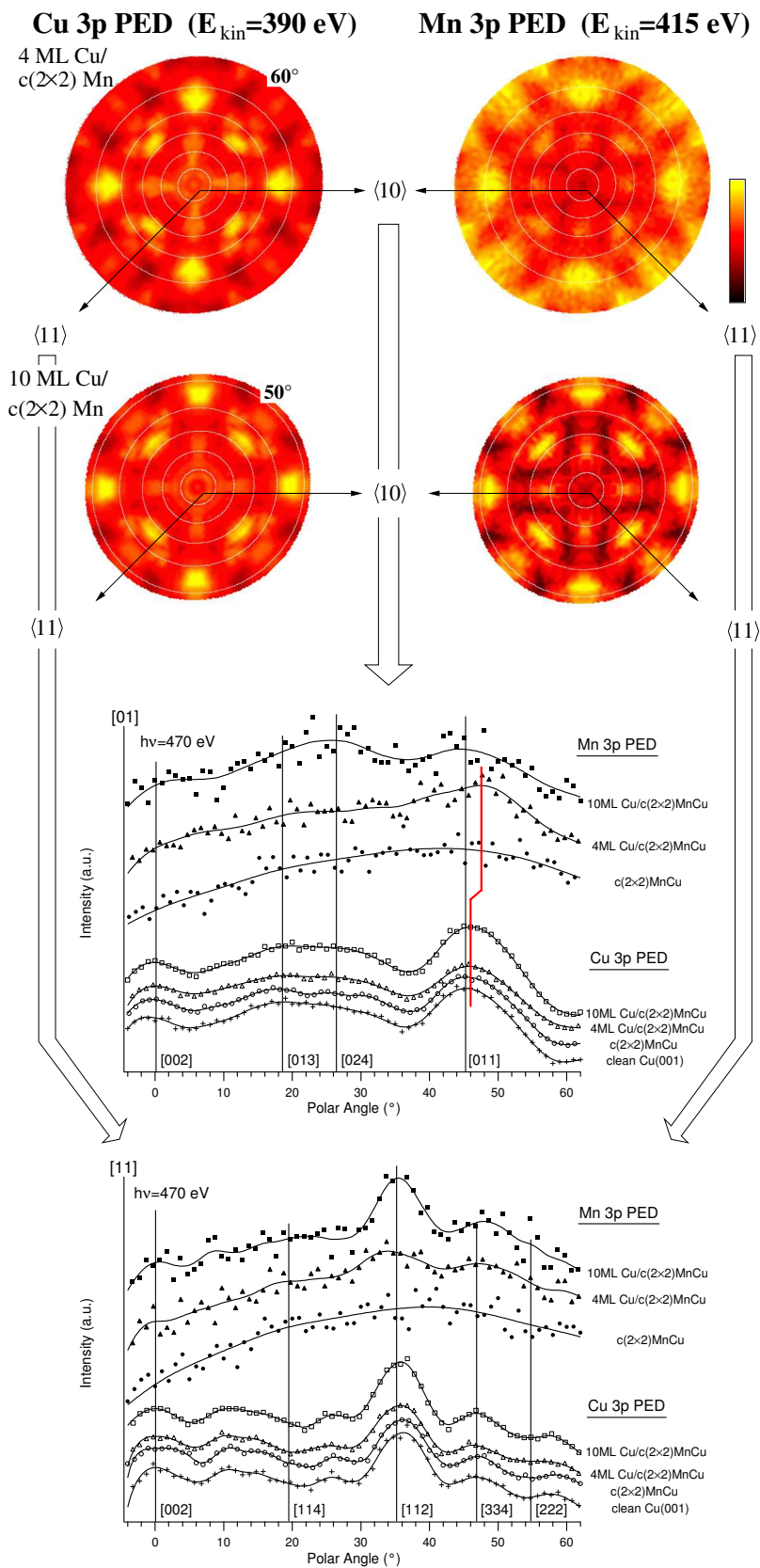


Figure 4.2: PED results. Top part: 2-dimensional intensity distribution plots (holograms) of 4 and 10 ML Cu on $c(2 \times 2)$ MnCu/Cu(001), for either Cu 3p and Mn 3p core levels. Bottom part: corresponding polar cuts in $[01]$ and $[11]$ high symmetry directions.

niques will be discussed in the following sections. For copper coverages up to 10 monolayers, a manganese core-level signal was still obtained. For higher coverages, only copper signals were detected indicating a completely covered surface. A summary of the experimental results is shown in Fig. 4.2. The upper part shows the two-dimensional photoelectron diffraction intensity distribution in a stereographic projection (referred to as hologram in the following) for 2 copper coverages: 4 ML and 10 ML, for either Cu (left hand side) and Mn (right hand side) emissions, respectively. The Cu $3p$ PED holograms are nearly identical to the clean Cu(001) $3p$ PED pattern (not shown). On the other hand, the Mn $3p$ PED intensity distribution pattern of 4 monolayers Cu indicates already well resolved structures, very similar to the Cu hologram. These structures become even more pronounced for the 10 ML copper-overlayer case. Note that for non-ordered samples an isotropic pattern should occur. The obtained holograms, however, indicates growth like in a normal Cu(001) layer stack. Together with the above mentioned suppression of the Mn-core level intensity for coverages above 10 ML (and, hence, a fully Cu covered $c(2\times 2)$ MnCu surface), these results suggest an epitaxial pseudomorphic growth mode. The corresponding polar cuts of the intensity distribution displayed in the lower part of Fig. 4.2 support this point of view. In the polar cuts also the theoretical values of the uncorrugated 4 ML Cu/ $c(2\times 2)$ MnCu compound taken from Fig. 4.1 (a) are given by vertical lines. When comparing the sketched structural model of 4 ML Cu on top of a corrugated $c(2\times 2)$ MnCu surface (in Fig. 4.1 [b]) with the one without corrugation (Fig. 4.1 [a]), the most prominent difference should be an intensity increase around 50° in [01] direction. In the model, however, only the first Cu atom in the [011] direction row has been taken as diffracting atom. A consideration of the following atoms in this row will slightly change the intensity distribution. When comparing the two low coverage holograms of Cu and Mn as emitters (Fig. 4.2), a shift of the main intensity spot in the [01] direction can be detected, also seen in the polar cut below (marked in the figure). A corrugation of the manganese atoms can, therefore, be concluded. For 10 ML coverage this shift of the spot has disappeared and the normal 45° Cu(001) value is reestablished. There are several reasons possible for this behaviour: (i) the existence of additional scatterer in the row, that diffract close to the 45° value and (ii) a flattening of the $c(2\times 2)$ MnCu interface underneath 10 ML of Cu. A discrimination between these two options is not possible on the basis of this experiment and the statistics of the curves do not permit deeper analysis. We underline, however, that for low coverage (4 ML), a preserved outward corrugation of the Mn atoms can be concluded and therefore, similar magnetic properties as in the $c(2\times 2)$ MnCu/Cu(001) compound may be expected also for Cu/ $c(2\times 2)$ MnCu/Cu(001).

4.2.2 Mn-Cu multilayers

As already mentioned above, more than 4 ML Cu/ $c(2\times 2)$ MnCu/Cu(001) results in a $p(1\times 1)$ LEED pattern. Upon deposition of a second half of monolayer of Mn on top of this 3-layer compound, a $c(2\times 2)$ LEED pattern was recovered. From this LEED pattern and the fact, that copper covers completely the Cu/ $c(2\times 2)$ MnCu/Cu(001) surface compound and grows in a fcc-(001) structure, a $c(2\times 2)$ MnCu/Cu multilayer growth was concluded ².

4.3 Magnetism of the system

Magnetic properties of multilayer systems can be studied with the same techniques as the $c(2\times 2)$ MnCu/Cu(001) surface. Soft X-ray absorption (SXA or NEXAFS) measurements have shown that the Mn atoms of $c(2\times 2)$ MnCu are in a high spin state [O'B93]. Here, the results of a similar study performed on $c(2\times 2)$ MnCu, on $p(1\times 1)$ Cu/ $c(2\times 2)$ Mn/Cu(100), and finally on the sandwich system $c(2\times 2)$ MnCu/Cu/ $c(2\times 2)$ Mn/Cu(001) are presented. The branching ratio \mathcal{B} between the white-line intensities at the L_3 and L_2 threshold is defined by

$$\mathcal{B} = \frac{I(L_3)}{I(L_3) + I(L_2)}. \quad (4.1)$$

The $L_{2,3}$ absorption edge is dominated by the dipole transition from the $2p_{3/2}$ and $2p_{1/2}$ core levels into the *empty* $3d$ states. Branching ratios have been derived from peak areas assuming a linear background superimposed by two step functions as suggested by TOBIN *et al.* [Tob92]. The procedure of this background subtraction for the $c(2\times 2)$ MnCu/Cu(001) sample is illustrated in Fig. 4.3. The linear background, that is due to the secondary electrons, is subtracted first from the original curve (inset of Fig. 4.3). In a second step the electronic transition from the core levels into the continuum ($4s$ states) is considered. This is done by a superposition of two step functions [Stö92] with inflection points 2 eV *below* the L_3 and L_2 white-line positions. The value of approx. 2 eV corresponds to the energy position of the empty Mn $3d$ spin-minority ground states above the Fermi level [Rad97a]. However, the potential of the photo-hole may be lowered even below E_F in the final state leading to the situation that the white-lines appear at lower photon energies than the $2p \rightarrow 4s$ absorption edge. To account for such effects, the inflection points for the two step functions were assumed 1 eV below the L_3 and L_2 peak positions. Since here we compare only branching ratios obtained by the same background correction process, the position of the inflection point is not important for the analysis. For the width of the step function a value of about 3 eV was used that corresponds to the full width at half maximum of the L_3 and L_2 peaks. Considering this background the peak areas

²Photoelectron diffraction of this stack has not been carried out since the element specific method can't distinguish between the Mn (and Cu) atoms of the top and the underlying layers.

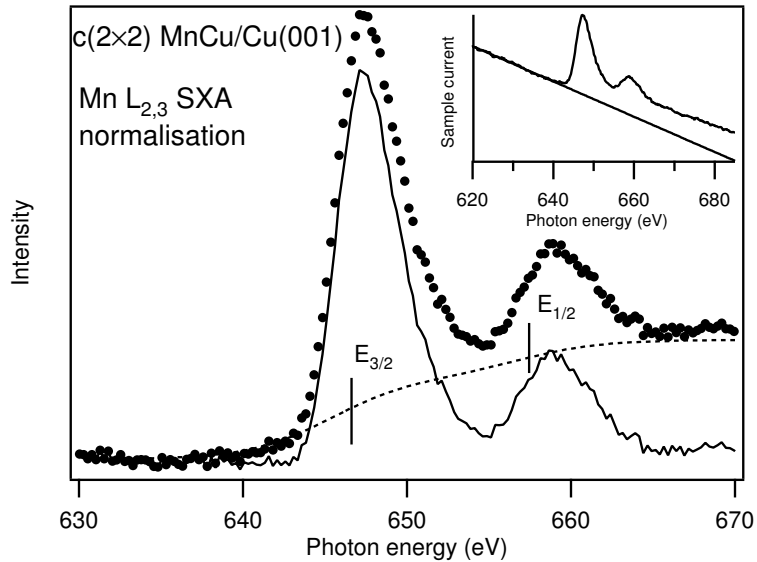


Figure 4.3: Normalisation procedure for the SXA spectrum for $c(2\times 2)\text{MnCu}/\text{Cu}(001)$: After a linear background correction (top inset), a two-step background function (dashed line) with the inflection points $E_{3/2}$ and $E_{1/2}$ 1 eV below the maxima peak positions was subtracted from the resulted spectrum (dotted). Peak areas are then derived by an integration of the finally normalised spectrum (continuous line).

and from there the branching ratio \mathcal{B} can be calculated. The relative error of the peak area determination was estimated by changing the step function values (height, width, inflection point position) in reasonable physical ranges and for the branching ratio a relative error of $\Delta\mathcal{B}=0.01$ was obtained.

For linear polarised light, derivations from the statistical value of $\mathcal{B}=2/3$ are due to spin orbit interactions. This effect was checked previously in the case of $\text{Mn}/\text{Cu}(001)$ [O'B93] and explained theoretically [vdL92]. A higher branching ratio value for the manganese $L_{2,3}$ absorption edge detected for the $c(2\times 2)\text{MnCu}$ surface compound indicates that Mn atoms are in a high spin ground state. Since the process depends strongly on the normalisation procedure, all normalisations were done in the same way and compared to a branching ratio value obtained for a 30 ML Mn film on $\text{Cu}(001)$. The latter system did not show any LEED pattern and was, therefore, interpreted as a non-magnetic polycrystalline Mn bulk sample. It should be noted that the obtained $\mathcal{B}=0.72$ value for this bulk Mn film is slightly higher than the non-magnetic statistic 0.67 value, possibly due to the applied normalisation procedure. Fig. 4.4 shows the Mn $L_{2,3}$ absorption doublet for all stages of the multilayer growth: $c(2\times 2)\text{MnCu}/\text{Cu}(001)$, 4 and 10 ML $\text{Cu}/c(2\times 2)\text{MnCu}/\text{Cu}(001)$, and $c(2\times 2)\text{MnCu}/10$ ML $\text{Cu}/c(2\times 2)\text{Mn}/\text{Cu}(001)$ as compared to the 30 ML $\text{Mn}/\text{Cu}(001)$ film representing non-magnetic bulk manganese. While the shape of the Mn $L_{2,3}$ edges of $c(2\times 2)\text{MnCu}$, $\text{Cu}/c(2\times 2)\text{MnCu}$ and $c(2\times 2)\text{MnCu}/\text{Cu}/c(2\times 2)\text{MnCu}$ are very similar to each others, there is a significant difference to bulk Mn. If from the measured branching ratio of the

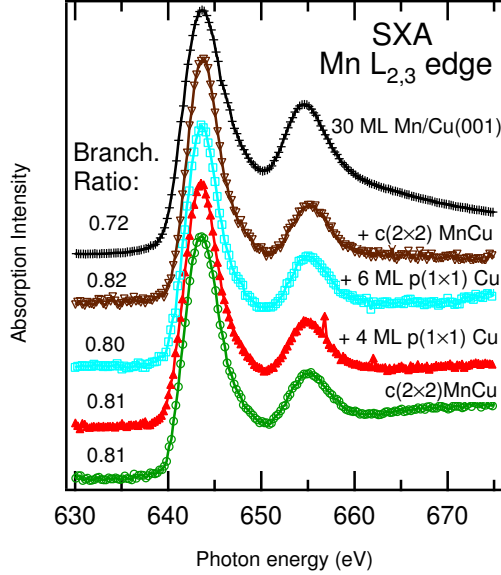


Figure 4.4: Soft X-ray absorption spectra at the Mn $L_{2,3}$ edge of $c(2\times 2)\text{MnCu}/\text{Cu}(001)$, 4 and 10 ML $\text{Cu}/c(2\times 2)\text{MnCu}/\text{Cu}(001)$, and $c(2\times 2)\text{MnCu}/10$ ML $\text{Cu}/c(2\times 2)\text{MnCu}/\text{Cu}(001)$ as compared to the one of 30 ML $\text{Mn}/\text{Cu}(001)$ film representing non-magnetic bulk manganese (from bottom to top).

simple $c(2\times 2)\text{MnCu}$ surface layer a high-spin ground state can be concluded, the same argument holds for Mn atoms of the following stages of multilayer formation. Obviously, a high spin-ground state is even present in the case of the 10 ML $\text{Cu}/c(2\times 2)\text{MnCu}/\text{Cu}(001)$ stack, where the manganese atoms lie far below the surface and no corrugation was detected by photoelectron diffraction. For the second $c(2\times 2)$ surface on the top of the 3-layer sandwich, the signal from the Mn atoms of the two compound layers overlap each other. Here the manganese atoms of the upper as well as the buried Mn layer contribute to the signal but the signal of the latter is very small as compared to the top layer contribution. Since no derivations from the \mathcal{B} value of the first compound layer was detected, also the Mn atoms of the second $c(2\times 2)\text{MnCu}$ layer are in a high spin ground state.

4.4 Photoemission results

4.4.1 Core-level photoemission

Core-level photoemission is a powerful tool to study electronic structure of solids. Not only the chemical composition of the sample can be concluded from the spectra but an analysis of binding energy shifts allows detailed informations about chemical bonding. Unfortunately, the discussion of core-level shifts is often very

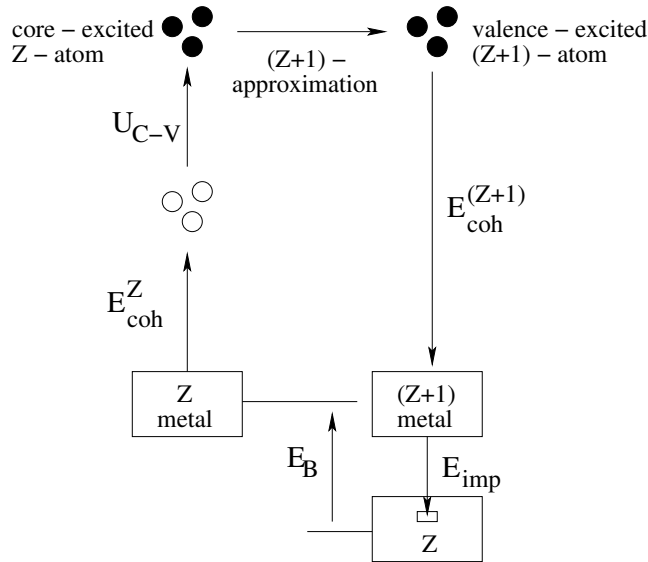


Figure 4.5: Hypothetical Born-Haber process for calculation of core-level binding energies of a Z -metal.

loose and handwaving and the conclusions, therefore, not always correct. Usually a final-state screening picture is applied, which relates energy shifts to charge-transfer. In this way, a chemical shift to higher binding energies is taken as indication for electron removal, i.e. oxidation of the respective atom, while a shift to lower binding energies is interpreted as electron up-take, i.e. reduction of the atom. In the same way, surface core-level shifts (SCS) are treated: Since at the surface the atomic coordination is smaller than in the bulk, final screening is less effective, and as a result an energy shift to higher binding energy is obtained. This naive picture fails, however, in several cases: For example, the chemical shift of the localised $4f$ -level of Eu and Yb in compounds with strongly electronegative elements is always negative, and the surface components of Au-metal are shifted to lower binding energy.

20 years ago, JOHANSSON proposed a simple method that allows a quantitative prediction of core-level binding energy changes [Joh80]. This method is based on a hypothetical Born-Haber process that replaces the photoexcitation process into a sequence of thermo-chemical steps that arrives to the same final-state and is shown schematically in Fig. 4.5. Starting with a metal of an element with atomic-number Z , as a first step evaporation of the metal is considered that takes the cohesive energy of the Z -metal, E_{coh}^Z . As a second step, excitation of a core-electron into the lowest lying unoccupied valence orbital in the gas-phase takes place that is related to an excitation energy U_{C-V} . The core-excited atoms are now replaced by atoms of the next following element in the periodic table ($Z+1$ -approximation) that are characterised by the same valence-electron configuration as the previous core-excited atoms. The ($Z+1$)-atoms are now condensed to a ($Z+1$)-metal leading to an energy gain of E_{coh}^{Z+1} . As a final step, the ($Z+1$)-metal is dissolved into the Z -metal applying the respective formation enthalpy,

called “impurity term”, E_{imp} . The resulting insulated $(Z+1)$ -atoms in the host of the Z -metal are then considered as equivalent to the fully-screened final-state of photoemission. The binding energy, E_B , is now obtained by summing up the energies involved in the individual steps of the model:

$$E_B = E_{coh}^Z + U_{C-V} - E_{coh}^{Z+1} + E_{imp}. \quad (4.2)$$

At the surface, cohesive-energies are reduced to about 80% of their bulk values due to the reduced coordination number [Joh80]. Thus, the surface core-level shift ΔE_{SCS} is given by:

$$\Delta E_{SCS} := E_B^{surface} - E_B^{bulk} \cong 0.2 \cdot (E_{coh}^{Z+1} - E_{coh}^Z - E_{imp}). \quad (4.3)$$

Chemical bonding can be taken into account introducing the formation enthalpy, $-\Delta H$, needed to decompose the compound into metallic pieces of the pure elements. In this way, the cohesive energies in (4.2) have to be replaced by $(E_{coh}^Z - \Delta H^Z)$ and $(E_{coh}^{Z+1} - \Delta H^{Z+1})$, respectively³, and the chemical shift may be expressed as:

$$\Delta E_{CS} := E_B^{comp} - E_B^{bulk} = \Delta H^{Z+1} - \Delta H^Z + E_{imp}^{comp} - E_{imp} \quad (4.4)$$

whereby E_{imp}^{comp} denotes the heat of solution of a molecule of the $(Z+1)$ -compound in the matrix of molecules of the Z -compound. Values for the formation enthalpies and the impurity-term may be calculated from the semi-empirical Miedema-scheme [Mie75, Mie76]. Thereby, E_{imp}^{comp} results usually small and may be neglected.

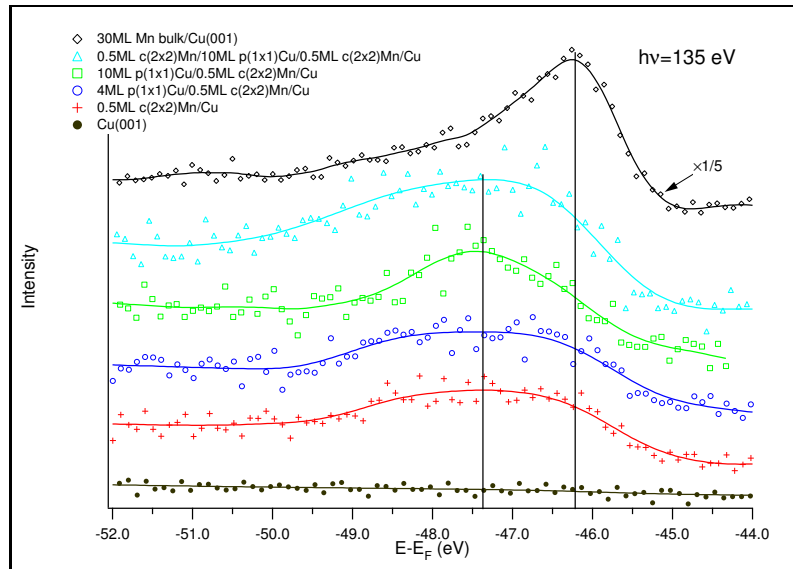
Applying the method to the present case of Mn-Cu compound, we will start with the surface core-level shifts of pure metals: For Mn, the $(Z+1)$ -element is Fe, $E_{coh}^{Fe} - E_{coh}^{Mn} = 1.4$ eV and $E_{imp} \approx 0$ eV, results in $\Delta E_{SCS} \cong 0.3$ eV to higher binding energies. For Cu, the $(Z+1)$ -element is Zn, $E_{coh}^{Zn} - E_{coh}^{Cu} = -2.1$ eV and $E_{imp} \cong 1$ eV, thus $\Delta E_{SCS} \cong -0.2$ eV.

Figs. 4.6(a) and (b) show PE spectra of the Mn $3p$ and Cu $3p$ binding energy regions, respectively, for the pure metals and the considered surface compounds and multilayers⁴. In case of Mn-metal, the $3p$ spectrum consists of a single feature with a broad asymmetric tail towards higher binding energy, while in case of Cu a well-resolved spin-orbit split doublet is observed. With a linewidth larger than 1 eV the SCS of Cu (-0.2 eV) is spectroscopically not resolved, but the spin-orbit

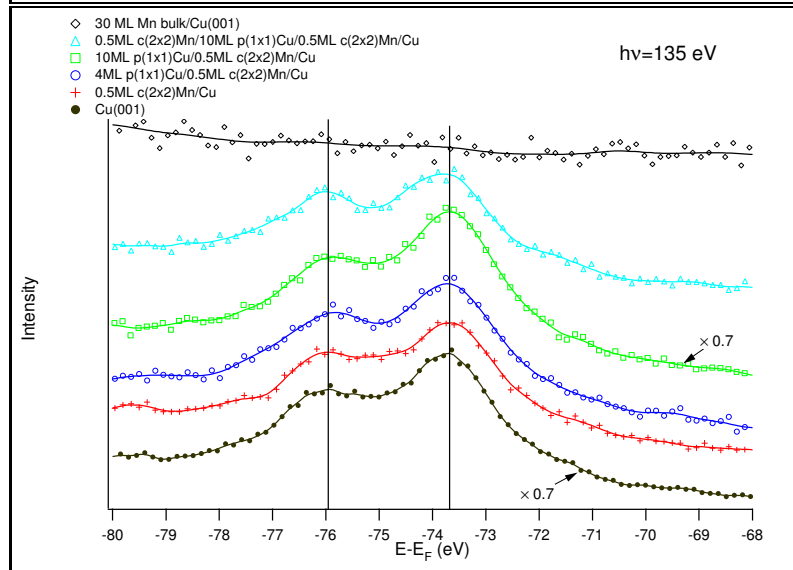
³Note, that for an exothermic process ΔH is negative, while cohesive energies are taken positive.

⁴While the photoelectron diffraction experiment were carried out with a photon energy of 470 eV, the presented core-level photoemission data were taken at $h\nu=135$ eV. There are several reasons for using this photon energy, (i) better energy resolution (for TGM monochromator $\propto E^{3/2}$), (ii) higher surface sensitivity due to a lower electron mean free path [Den79], (iii) highest cross-section for the Mn $3p$ core level [Yeh85], and (iv) maximum of monochromator transmission. The incidence angle was chosen to be 45° in order to use both s - and p - linear polarised light. As a reference and for further interpretation the valence band with the Fermi edge was measured and binding energy values are given in respect to the sample Fermi level.

(a) Mn 3*p* core-level emission



(b) Cu 3*p* core-level emission



(c) valence band emission

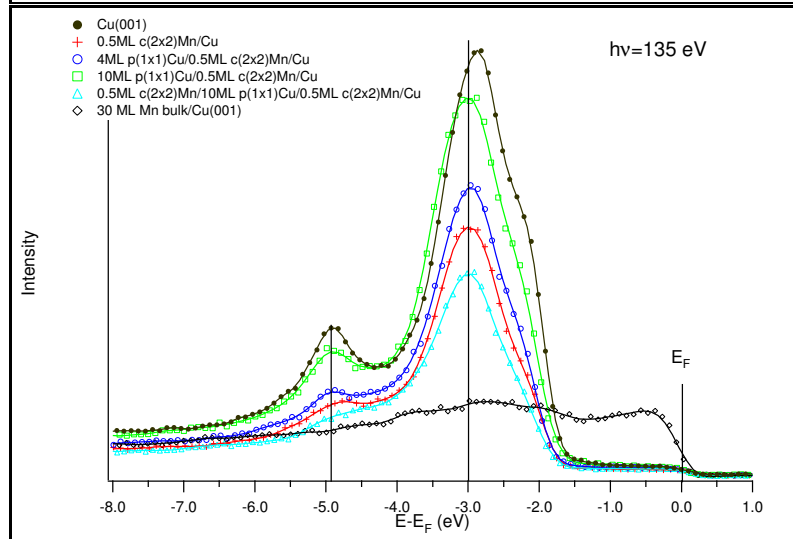


Figure 4.6: PE spectra of the 3*p* core-levels of Mn (a) and Cu (b) in Mn/Cu(001), as well as the valence band structure (c) measured with $h\nu = 135$ eV.

components are well separated due to the the large splitting observed (2.2 eV). In Mn, the respective splitting amounts to only 0.7 eV⁵, and the $3p_{3/2}$ -component of the surface emission appears with a ΔE_{SCS} of 0.3 eV just in between the $3p_{3/2}$ - and $3p_{1/2}$ -bulk emission leading to an unresolved triangle-like shape of the PE spectrum. For the surface compound and the multilayer systems, the Mn $3p$ spectra consists of a broad bump shifted with respect to the pure metal by about 1 eV to higher binding energies, while the Cu $3p$ spectra remains unaffected⁶. For the Cu-states this behaviour is expected since the spectra are dominated by strong emissions of the underlying pure Cu-substrate masking chemical shifts of the surface compound. The behaviour of the Mn-states, however, is strange, since a well-resolved doublet is expected for the surface compound. The calculated ΔH of a hypothetical MnCu-bulk compound is positive (0.06 eV) indicating that this compound is unstable. The same holds for a FeCu-bulk compound ($\Delta H=0.23$ eV). The surface-component of the hypothetical MnCu-crystal is expected at $\Delta E_{SCS}^{MnCu} = 0.2 \cdot (E_{coh}^{Fe} - \Delta H^{FeCu} - E_{coh}^{Mn} + \Delta H^{MnCu} - E_{imp}) \cong 0.3$ eV, the chemical shift of MnCu-bulk with respect to Mn metal $\Delta E_{CS}= 0.17$ eV. Thus, the shift of the Mn $3p$ states of the MnCu surface compound with respect to Mn-metal is expected to be of the order 0.5 eV, much less than observed.

Neither the large shift nor the strange shape of the Mn $3p$ emission of MnCu can be understood on the basis of the present model. A possible explanation, however, are multiplet effects arising from the coupling of the $3p$ -hole with the unfilled $3d^n$ shell. In the surface compound the overlap of the $3d$ -orbitals of neighbouring atoms is reduced with respect to Mn-metal and the $3d$ -states behave, therefore, more localised. This is the mechanism responsible for the high-spin state and the magnetism of the surface compound, and the same phenomenon is also reflected in the $3p$ -core level spectra: The localisation of the $3d$ -orbitals leads to formation of strong $3p^5 3d^*$ final-state orbitals (the asterisk denotes a probable increase of the $3d$ -occupation in the final state) and thereby to the broad PE signal that is strongly different for all synthesised overlayer stacks from that of pure Mn-metal.

4.4.2 Valence-band photoemission

The valence band was studied with photon energies ranging from 32 eV to 135 eV. The valence-band spectra taken at a photon energy of 135 eV were taken together with the $3p$ core-levels spectra at the SU 7 beamline, while spectra measured at other photon energies were taken at the SU 6 beamline of LURE. In both cases linear polarised light was used with an incidence angle of 45°. Fig. 4.6 (c) shows valence-band photoemission spectra taken at different stages of the multilayer formation. For reason of comparison, also spectra of clean

⁵Such spin-orbit splittings can be calculated [Kut92] and lead to approx. 1.8 eV for copper and 0.7 eV for manganese.

⁶The binding energy shift of the Mn $3p$ core-level was already observed in [O'B93] but interpretation was slightly different.

Cu(001), $c(2\times 2)$ MnCu/Cu(001), and bulk Mn are shown. After formation of $c(2\times 2)$ MnCu/Cu(001) a slight shift of the most intense peak from 2.8 eV to 3.0 eV binding energy can be observed. RADER *et al.* found the main peak in $c(2\times 2)$ MnCu at 3.7 eV using resonant photoemission [Rad97a] and assigned this peak to emissions from the Mn 3*d* spin majority band. This result, however, could not be confirmed in the present work (see chapter 3.2.3). An interaction of the Mn bands with the intense Cu 3*d* bands responsible for this peak is possible. The Cu *sp* band located at approx. 5 eV binding energy, on the other hand, does not change its position. At the following stages of multilayer formation structures do not shift the peak positions, only an intensity suppression of the Cu *sp* band can be observed that increases with thickness of layered structure. In difference to Cu(001) the spectrum of non-magnetic bulk Mn shows a rather broad band distribution ranging from the Fermi edge to 5 eV binding energy. It should be mentioned, however, that this Mn layer was not ordered and such a broad structure is, therefore, expected since the experiment integrates over all possible interband transitions. As can be seen, a part of the intense structures is located around the Fermi edge and was attributed to the non-magnetic 3*d* bands [Rad97a]. An enhancement of the intensity around the Fermi edge upon multilayers formation would, consequently, signify a growth of non-magnetic Mn. This is not observed, however, and is a further confirmation, that the Mn atoms behave still magnetic in the synthesised multilayers.

A photon energy of 135 eV is, however, not well suited for valence band mapping, since \vec{k} and energy resolution as well as surface sensitivity are rather low as compared to those at lower photon energies. Therefore, photon energies of 32 eV and 55 eV were applied in the following. Since the spectra changes only slightly in going from Cu(001) to $c(2\times 2)$ MnCu (see chapter 3.2), strong changes for the spectra with further copper overlayers and a second $c(2\times 2)$ MnCu surface compound formation cannot be expected. Fig. 4.7 shows the angle resolved photoemission spectra for Cu(001), $c(2\times 2)$ MnCu/Cu(001), 4 ML $p(1\times 1)$ Cu/MnCu/Cu(001), and the multilayer system $c(2\times 2)$ MnCu/Cu/MnCu/Cu(001) in normal emission taken at a photon energy of 32 eV. The spectra look very similar to each other. The only difference is that with increasing coverage all structures become broader and the main peak drops. This behaviour is expected for a surface that becomes less ordered, when other layers are deposited onto a well ordered surface. Whereas the intensity of the main peak around 3 eV binding energy decreases, other less pronounced Cu-derived features like the peak at around 11.3 eV seem to become enhanced upon deposition. This peak can be identified as a Cu two-hole final state satellite [Iwa79]. A comparison of the spectra normalised to the higher harmonics intensity above the Fermi level reveals an increase of the intensity close to the Fermi level for the manganese overlayers. There exist mainly two possibilities to attribute this intensity enhancement to Mn 3*d*-derived states, (*i*): a growth of non-magnetic Mn with non-spin-split 3*d* bands in the vicinity of the Fermi level, or (*ii*): spin minority Mn 3*d* bands that become partly occupied. The growth of

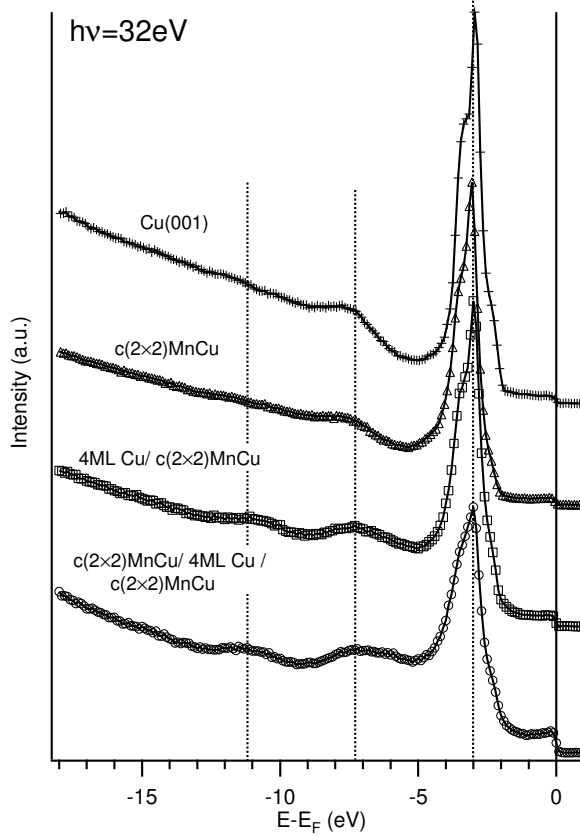


Figure 4.7: Angle resolved photoemission spectra taken at a photon energy of 32 eV in normal emission geometry for Cu(001), $c(2\times 2)$ MnCu/Cu(001), 4 ML $p(1\times 1)$ Cu/ $c(2\times 2)$ MnCu/Cu(001), and $c(2\times 2)$ MnCu/Cu/ $c(2\times 2)$ MnCu/Cu(001). Dotted lines denote Cu-derived band features: the 3d states at 3 eV, the sp band at approx. 7 eV, and a two-hole final state satellite at approx. 11 eV.

non-magnetic manganese can nearly be ruled out on the basis of the SXA and core-level experiments. The second explanation is also not very probable, since an occupied spin minority band was clearly found near $\bar{X}_{p(1\times 1)}$ but not confirmed at $\bar{\Gamma}_{p(1\times 1)}$ (see chapter 3.3). The origin of this phenomenon is, therefore, independent from the magnetic state of the manganese. A more probable explanation is based on the consideration of indirect interband transitions. Band structure calculations for Cu(001) do not show any bands close to the Fermi level sampled with photon energies around 32 eV. Notwithstanding at all \vec{k} points the Fermi edge can be measured. Direct electron transitions result mainly in pronounced peaks which are broadened due to finite life time of the excited electrons. Additional contributions to the signal are caused by indirect transitions, when phonons destroy the electron \vec{k} conservation. Furthermore, band structure calculations assume infinite dimensions of the crystal. Photoemission experiments, on the other hand, deal with significant surface contributions to the signal. At the surface, the translation symmetry is broken and projected bands along the measured high symmetry direction contribute to the spectra. sp -type bands in metals disperse

strongly across the Brillouin zone and the respective projected bands may contribute to nearly all \vec{k} points. Another reason for the higher Fermi-edge intensity is that the cross-section of the manganese 4s states is nearly 2 times higher than that of the copper 4s states. Consequently, an enhancement of the Fermi-level intensity is expected with increasing Mn 4s and mixtures.

Band structure investigations for copper overlayers on $c(2\times 2)\text{MnCu}/\text{Cu}(001)$ taken along the high symmetry directions $\bar{\Gamma}\bar{X}_{p(1\times 1)}$ and $\bar{\Gamma}\bar{M}_{p(1\times 1)}$ do not indicate changes relative to the photoemission spectra measured for $c(2\times 2)\text{MnCu}$ except the \vec{k} -region around the $\bar{X}_{p(1\times 1)}$ point that was already discussed in chapter 3.3. The growth of the second $c(2\times 2)\text{MnCu}$ surface compound on the three-layer system $\text{Cu}/c(2\times 2)\text{MnCu}/\text{Cu}(001)$ resulted in further broadening of the peaks and higher background intensity but no new bands were monitored. As a summary, Fig. 4.8 shows the photoemission spectra for all stages of the multilayer formation measured at different \vec{k} points along the two high symmetry directions ($h\nu=32$ eV). New features due to possible coupling between the two compound layers do not appear at larger emission angles. On the other hand, if such structures exist, their contributions to the spectra would be weak as already was seen in case of $c(2\times 2)\text{MnCu}$. Furthermore, the sample quality must be very good to observe the discussed features. In case of $c(2\times 2)\text{MnCu}$, the lifetime of the new spectral contributions was only approx. 1 hour. This is about the preparation time of the multilayer system, if necessary checks for structural characterisation with LEED and ARUPS are performed. A faster preparation could not be realised due to the complicated sample treatment.

4.4.3 Fermi surface analysis

The differences of the Fermi surfaces between $\text{Cu}(001)$ and $c(2\times 2)\text{MnCu}$ were already discussed in detail in chapter 3.3. The most interesting \vec{k} region is around the $\bar{X}_{p(1\times 1)}$ point, where the copper sp band approaches the Fermi energy near the Shockley inverted L band gap. This band does not cross the Fermi level for photon energies between approx. 20 and 34 eV. In clean $\text{Cu}(001)$ the Shockley surface state, that resides in this gap is unoccupied and touches only the Fermi energy. It becomes occupied in the $c(2\times 2)\text{MnCu}$ surface compound due to the work function change that influences both the image state as well as the Shockley state. Furthermore a spin minority band becomes occupied near $\bar{X}_{p(1\times 1)}$ resulting in a spin minority Fermi surface.

Since measurements of the whole Fermi surface with a single channeltron analyser take much longer acquisition time than the usual life time of the sample, the Fermi surface was analysed only by taking cuts in the high symmetry directions $\bar{\Gamma}\bar{M}_{p(1\times 1)}$ and $\bar{\Gamma}\bar{X}_{p(1\times 1)}$. For this purpose, first, the usual procedure to determine the Fermi edge position was applied. Then, the intensities at E_F and at approx. 2 eV higher kinetic energy (for further normalisation) were monitored over the required azimuthal angle range. Fig. 4.9 shows two high symmetry directions in

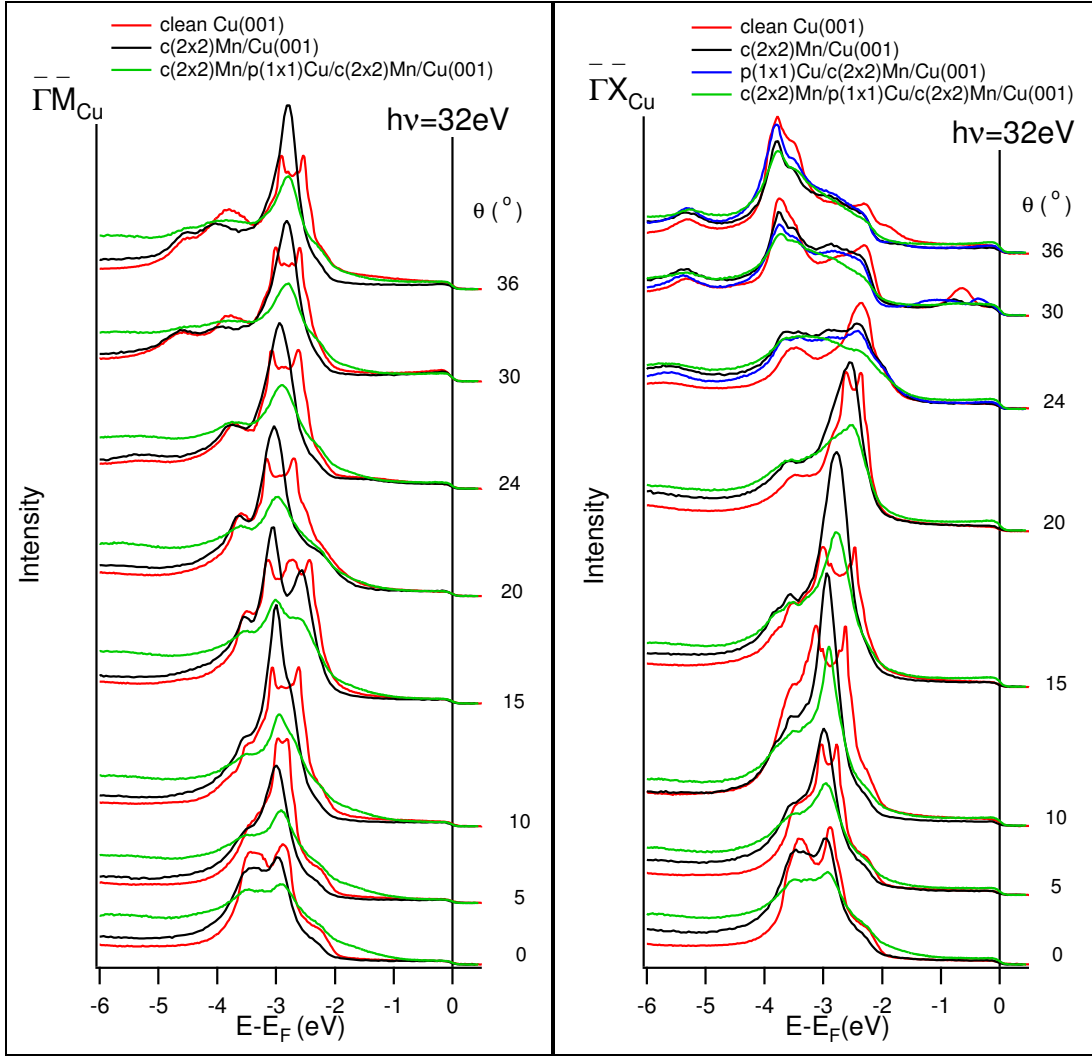


Figure 4.8: Comparison of the angle resolved photoemission spectra of Cu(001), $c(2\times 2)$ MnCu, 4 ML Cu/ $c(2\times 2)$ MnCu, and a second $c(2\times 2)$ MnCu surface compound measured in the $\bar{\Gamma}\bar{X}_{p(1\times 1)}$ and $\bar{\Gamma}\bar{M}_{p(1\times 1)}$ high symmetry directions with a photon energy of 32 eV.

the experimental two-dimensional $c(2\times 2)$ MnCu/Cu(001) Fermi surface cut and the corresponding polar scans measured along these high symmetry directions. The observed ring structure in the two-dimensional Fermi surface cut originates from the copper sp band. It should be mentioned that the sp band does not cross the Fermi edge in $\bar{\Gamma}\bar{X}_{p(1\times 1)}$ direction and forms the “dog bone structure” as well as in the measurement with $h\nu=21.2$ eV (see the band structure in Fig. 3.6). The closed structure of the ring is caused by the Shockley surface state that is located exactly in the band gap and becomes occupied in $c(2\times 2)$ MnCu. In the Fermi surface polar cuts shifts of the peaks from Cu(001) to $c(2\times 2)$ MnCu/Cu(001) are due to a slight shift of the copper sp band ($\bar{\Gamma}\bar{M}_{p(1\times 1)}$ direction) that changes its positions and due to an occupation of the Shockley state, which shifts to higher binding energies upon Mn deposition ($\bar{\Gamma}\bar{X}_{p(1\times 1)}$ direction). Since the surface-

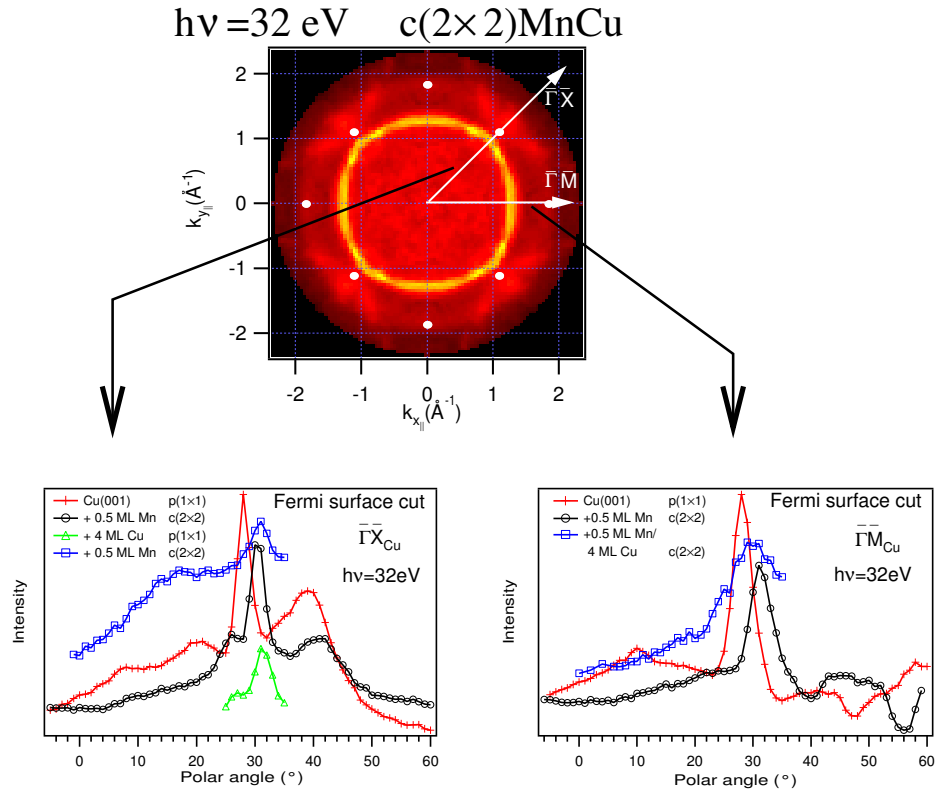


Figure 4.9: Fermi surface evaluation upon multilayer formation: *top*: two-dimensional Fermi surface cut for $c(2 \times 2)\text{MnCu}/\text{Cu}(001)$ measured with $h\nu=32 \text{ eV}$ in a 90° polar angle range and duplicated to a 360° range. High symmetry directions, where the Fermi surface polar cuts are taken, are shown by arrows. *Bottom*: Polar cuts of the Fermi surfaces of the Mn-Cu multilayers.

state energy is directly coupled to the work function variation caused by the magnetism of the manganese atoms, the observed shift of the copper sp band is also assigned to the high magnetic moment of Mn. Further deposition of copper does not affect the Fermi-level crossing of the Shockley state in $\bar{\Gamma}\bar{X}_p(1 \times 1)$ direction. However, the formation of the second $c(2 \times 2)\text{MnCu}$ surface compound on the $\text{Cu}/c(2 \times 2)\text{MnCu}/\text{Cu}(001)$ three-layer system changes slightly the shape of the polar cut: The total intensity at the Fermi level increases although the crossing is less pronounced as compared to the cut for the $c(2 \times 2)\text{MnCu}$ system. The reason was already mentioned above. The quality of the structural order in the layer decreases and, hence, bands become broader and less intense. However, the band crossing takes place clearly at the same polar angle as in $c(2 \times 2)\text{MnCu}$. This confirms that the manganese atoms are still in a high spin ground state. This conclusion is based on the fact that for a non-magnetic system the work function would approach the value of $\text{Cu}(001)$ and both sp bands and the Shockley state will shift back to initial positions in $\text{Cu}(001)$.

4.5 Conclusions

It was shown that copper grows pseudomorphically on the $c(2\times 2)\text{MnCu}/\text{Cu}(001)$ surface compound and enables the possibility to grow further $c(2\times 2)\text{MnCu}$ surface compounds on top. This finding opens the possibility to establish not only artificial bulk compounds but also magnetic multilayer systems as the Mn atoms were detected to carry still a high atomic moment below the copper overlayers. It enables further studies of the material as application for GMR-materials or for hard drive materials since magnetic information can be conserved below a copper layer.

Chapter 5

The electronic structure of Mn overlayers on ferromagnetic films of Fe, Co, and Ni epitaxially grown on Cu(001)

5.1 Synthesis of the fcc-(001) surfaces

Most compounds and alloys form (poly-) crystalline solids. Crystal structure depends on the electronic properties of the atoms: Electron density, ion radii, bonding characteristics, and other properties like magnetism. Therefore, some elements do not crystallise in closed packed structures like hexagonal closed packed (hcp) or face centred cubic (fcc) lattices. An interesting example is Mn metal that reveal at room temperature a simple cubic (sc) structure with 58 atoms per unit cell, while at higher temperatures it undergoes phase transitions into fcc and body centred cubic (bcc) structures (see Fig. A.2). These phases can also be stabilised at room temperature in form of thin films grown epitaxially on adequate substrates. These films remain thermodynamically stable up to a certain critical film thickness above which the conventional room temperature phase becomes favourable in energy. For magnetic materials, phase transitions are usually related to changes of the magnetic properties. In this way, epitaxial growth allows not only to influence crystal structures and lattice parameters, but also to change the room-temperature magnetic properties of the materials. In this chapter we are interested to stabilise fcc (001) surfaces of the ferromagnetic metals Fe, Co, and Ni with the purpose to grow Mn on top of them and to analyse the properties of the resulting surface compounds.

5.1.1 Fe/Cu(001)

Fe/Cu is one of the “model systems” of epitaxial metastable film growth. Fig. 5.1 (a) shows the calculated total energy versus the Wigner-Seitz radius r_{WS} [Mor86].

The ferromagnetic bcc phase is energetically preferred relative to the fcc phase in agreement with the well-known magnetic and crystallographic phase diagram of iron. If a fcc structure could be stabilised, a wide variety of magnetic structures will be available depending on the lattice constant as indicated in Fig. 5.1 (b) [Mor89, Mor88].

Since Cu has a fcc lattice with a nearest neighbour (NN) distance close to the iron NN value, the most important precondition to grow thin fcc iron films is fulfilled. Experimentally, the initial state of growth is still controversial. Layer-by-layer, bilayer, island growth as well as intermixing of the above modes at room temperature were reported (see [Mül95] and references therein). At a coverage of 2 ML a (4×1) reconstruction has been observed, that transforms into a (5×1) overstructure at 4 ML coverage [Mül95]. For higher coverages (< 11 ML) a $p2mg(2\times 1)$ LEED pattern indicates further changes. Above 10 ML Fe grows in its room temperature stable bcc phase [Mül95, Kie93]. An overview of the phases and their magnetic properties characterised by surface magneto optical Kerr effect (SMOKE) is shown in Fig. 5.2 (a) for two different temper-

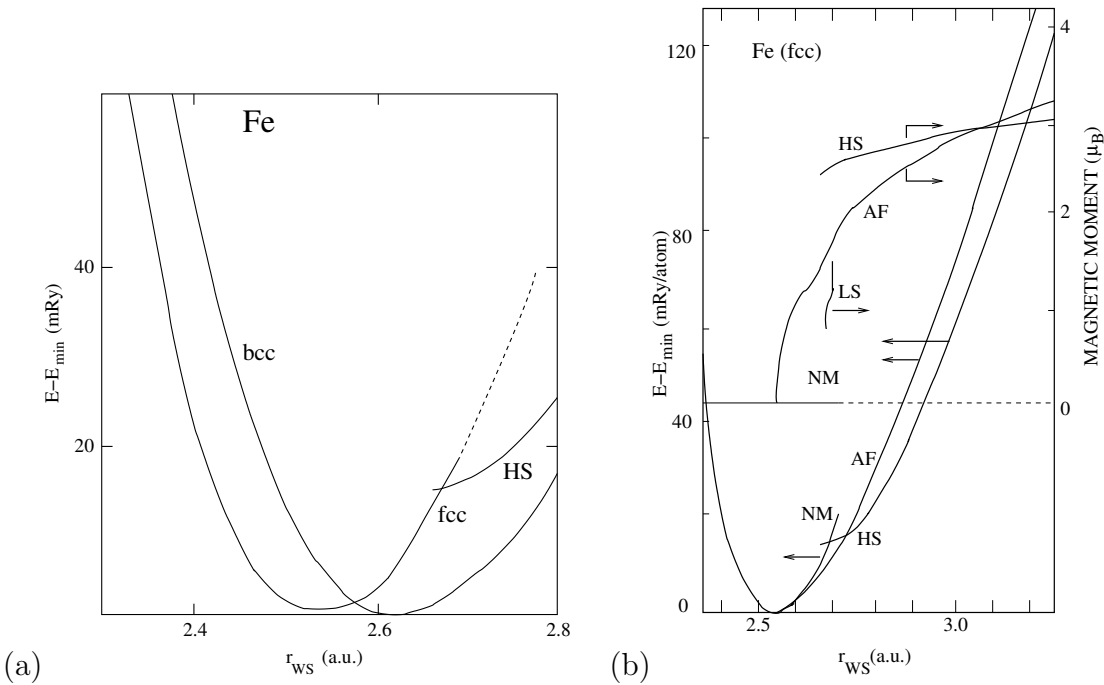


Figure 5.1: **(a)**: Calculated total energy versus the Wigner-Seitz radius r_{WS} for bcc and fcc Fe. The ferromagnetic bcc phase is slightly more favourable than the nonmagnetic (NM) fcc phase in agreement with the well-known magnetic and crystallographic phase diagram of iron. The ferromagnetic bcc phase is stable for all r_{WS} values larger than 2.58 a.u.. In the fcc structure, the NM phase transforms into a high spin (HS) phase for $r_{WS} \geq 2.66$ a.u. [Mor86]. There exists also a stable low spin (LS) phase in the r_{WS} range of the HS phase (not shown). **(b)**: Zero field magnetic moments and total energies as functions of r_{WS} for NM, antiferromagnetic (AF), LS, and HS phases of fcc Fe [Mor89].

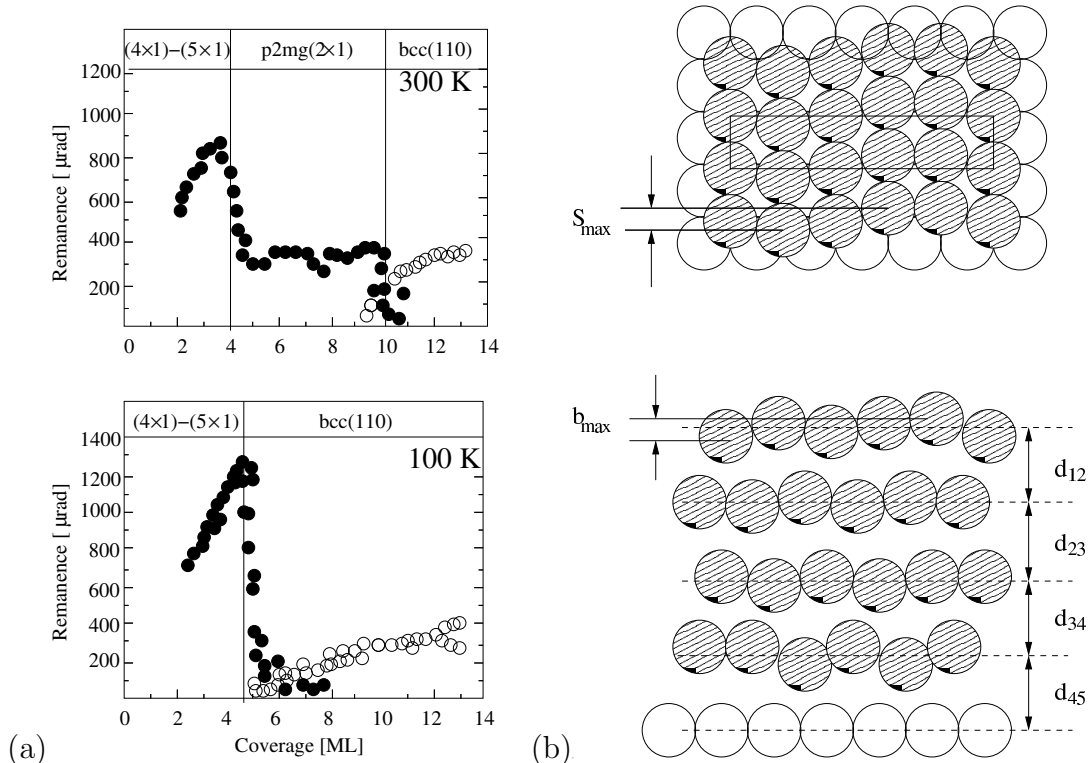


Figure 5.2: **(a)**: SMOKE signal of epitaxial Fe/Cu(001) as a function of coverage for films measured at room temperature and at 100 K, solid (open) circles denote the ellipticities obtained from hysteresis loops recorded in polar (longitudinal) geometry. **(b)**: Structural model of a 4 ML Fe/Cu(001) film. In the right upper corner a top view of only 1 Fe layer is represented, while in the right lower corner a side view of 4 ML Fe/Cu(001) is shown [Mül95].

atures [Mül95]. For coverages up to 4 ML the Fe film is ferromagnetic with perpendicular magnetic anisotropy [Mül95]. This is related to the formation of a tetragonal distorted structure with a c -axis expansion. The structure of a 4 ML Fe film with a (5×1) superstructure is shown in Fig. 5.2 (b) as derived from an I-V LEED analysis [Mül95]. The surface forms mainly a fcc lattice with sinusoidal deviations in all directions. The structure of the Fe films between 5 and 10 ML thickness was found to be fcc with almost no distortions [Wut93d, Cla87]. CO titration experiments at low coverage indicate still Cu atoms at the surface what is explained either by Cu segregation [Kie93] or - less probably - by island growth (Volmer Weber growth mode). Above 5 ML the copper concentration drops below 5% and the surface may be considered to consist only of Fe atoms, so that upon additional Mn deposition formation of a Mn-Cu surface compound can be ruled out.

The magnetism is strongly related to the structure of the film. While for films up to 4 ML thickness ferromagnetic coupling was observed, room temperature growth above 5 ML resulted in a ferromagnetic top layer with the $p2mg(2 \times 1)$ symmetry and an expanded interlayer spacing perpendicular to the surface (1.87

Å) and antiferromagnetic coupled subsurface layers with a smaller spacing (1.78 Å) as compared to the Cu(001) interlayer spacing of 1.80 Å [Mül95].

Recent results of *ab initio* local spin-density calculations carried out by MORONI *et al.* agree quite well with the experimental data [Mor99]. Fe films thinner than 3 ML adopt a ferromagnetic ground state. Thicker films with an even number of Fe monolayers (4 ML, 6 ML, and 8 ML) develop bilayer antiferromagnetic structures, and films with an odd number of Fe monolayers reveal a ferromagnetically coupled bilayer at the surface and degenerated spin structures underneath the surface [Mor99].

5.1.2 Co/Cu(001)

The room temperature phase of bulk Co is hexagonal ($a=2.51$ Å, $c=4.07$ Å). Above 450°C a phase transition to the fcc phase with a lattice constant $a=3.544$ Å takes place [Hul21]. Already 1968 JESSER and MATTHEWS observed for thin Co films on Cu(001) a metastable fcc phase at room temperature [Jes68]. Further investigations for such overlayers were carried out in order to investigate the interesting magnetic properties of the Co layers¹. The growth mode at very low coverages, layer-by-layer [Sch90] to bilayer growth, is still not clear [Kie93]. The bilayer growth was suggested on the basis of soft X-ray diffraction experiments. Recent investigations, however, found a bimodal growth with few Co atoms occupying Cu sites forming nucleation points for the subsequent Co layers [Nou99] and being probably responsible for the different findings. All following layers grow in a layer-by-layer mode with Co atoms in a fcc-like structure. Thereby the interlayer distance in the growth direction is reduced to maintain the total unit cell volume [Cer95, Kie93]. The resulting structure is, hence, not a fcc one, but a distorted tetragonal face centred arrangement (fct)². Fct Co films are ferromagnetic with a Curie temperature below 50 K for the monolayer Co and 500 K for a 2.5 ML Co film [Sch90]. Both temperatures are much lower than the Curie temperature of bulk fcc Co of 1388 K [Cra55]. CO titration experiments showed that the Cu amounts to less than 5% for a film thickness between 3 and 5 ML and growth temperatures between 80 and 300 K [Kie93]. As Co grows pseudomorphically without lateral distortion the LEED pattern shows a $p(1\times 1)$ structure independent of coverage.

Further interest results from the appearance of quantisation effects in thin layers of Co/Cu(001) observed with inverse photoemission and the possibility of synthesis of Cu/fcc-Co(001) layers with the existence of occupied quantum-well states that can be easily studied by PE [Ort93]. Spin-resolved PE experiments have

¹There exist also attempts to grow bcc Co as overlayers, above all on GaAs [Pri85, Teo98], and bulk bcc materials, e.g., Fe [Jay96] or Cr [Sch91]. Like for the fcc phase the driving force of the scientific interest is mainly the magnetism of the bcc Co film.

²There does not exist a fct lattice notation because this structure can be described as a body centred tetragonal structure (bct, I4/mmm). However, as in most publications the fct notation will here be used. This structure is also often assigned as fcc lattice.

shown that the Cu overlayers have states of sp symmetry, which are spin polarized by the confining magnetic interface [Car93]. Such quantum-well structures can only be observed, if the surface has very high crystalline quality [Ort92, Ort93] confirming a very good growth of Co/Cu(001).

5.1.3 Ni/Cu(001)

The room-temperature crystalline structure of Ni is already fcc with a lattice constant of 3.52 Å. From this point of view the question arises, why it is of interest to investigate Ni/Cu(001)? There are mainly two reasons for this study: (i) To investigate growth and structure development at the interface since the lattice mismatch amounts to about 2.5% and (ii) to study the magnetic properties as a function of thickness and lattice constant of the film. Ni films form pseudomorphic layers, which are strained up to a critical thickness of about 7 ML [Hua94, She95]. Between 7 ML and at least 10 ML, a growth with some misfit dislocations take place that are energetically preferred as compared to the strained layer [Hua94]. Depending on temperature, the macroscopic magnetic moment changes temperature dependent from in-plane magnetisation (coverage lower than 7 ML) to a direction perpendicular to the surface (above 7 ML [200 K]) [Far97]. Note that Ni(001) crystals reveal in-plane magnetisation. The Curie temperature T_C was found to be thickness dependent [Pla90]. Surprisingly, there exist only few studies of the electronic structure of Ni/Cu(001), that are furthermore controversial [Man97, Pam01]. While MANKEY *et al.* [Man97] observe already for a film thickness of 1 ML Ni/Cu a Ni bulklike electronic structure, PAMPUCH and co-workers [Pam01] found this limit at higher coverages (3 ML). STM investigations show a fully covered surface and a layer-by-layer growth mode [She95], however, the amount of Cu atoms diffused to the surface remains unknown. SPIŠÁK and HAFNER analysed theoretically the effect of a surfactant Cu layer and found its formation energetically preferred even for the 5 ML Ni/Cu(001) system [Spi00b]. Such a surfactant copper layer could solve the discrepancies between the results of LEED I-V investigations, that reveal a homogeneous tetragonal distortion [Pla90] and an outward relaxation of the outermost atomic surface layer [Mül95]. A growth of a Ni monolayer that is covered by a surfactant Cu layer was also claimed by KIM *et al* [Kim97]. Notwithstanding, very surface sensitive photoemission experiments with a photon energy of 43 eV found the intensity of the copper derived bands to be negligible for 6 ML Ni/Cu(001) [Pam01].

5.2 Manganese exposure to the pseudomorphic grown ferromagnetic fcc Fe, Co, and Ni thin films: spin majority bands

5.2.1 Theoretical considerations

In this section ASA-LMTO calculations with special correction terms were applied to investigate the electronic properties of the interfaces considered. LMTO stands for linear muffin-tin orbitals [And75], ASA for atomic sphere approximation. Briefly, the wave functions, i.e. the eigen functions of the Schrödinger equation are expressed by an expansion in muffin-tin orbitals inside (either muffin-tins, which do not overlap, or atomic spheres, which may overlap), and spherical functions outside of spheres (i.e. in the interstitial, where potential is assumed to be a constant). The potential inside of each sphere is averaged over the polar angles, i.e. is spherically symmetric, what introduces an additional approximation as compared to a Schrödinger equation with a more realistic so-called full potential (FPLMTO). For close-packed systems, ASA-LMTO is pretty accurate. However, ASA-LMTO is less accurate for open structures like oxides surfaces. In that case a set of empty spheres embedded between the real atoms may improve the results and make ASA-LMTO almost as accurate as FPLMTO [Hal]. A 6-layer slab consisting of 5 (001)-layers of the X element in a fcc stacking sequence (X=Cu, Fe, Co, Ni) terminated by a monolayer of the $c(2\times 2)$ MnX-compound was used to simulate the interface in the ASA-LMTO study. Although for the $c(2\times 2)$ MnCu surface compound a ferromagnetic ground state was assumed, not in all cases the ferromagnetic solution was found to have the lowest total energy in the other Mn systems considered here. Fig. 5.3 shows the calculated spin-resolved density of states for the Mn and X atoms in the $c(2\times 2)$ MnX/X(001) surface layer optimised for the lowest total energy. For $c(2\times 2)$ MnCo/Co(001) as well as for $c(2\times 2)$ MnFe/Fe(001) the antiferromagnetic solution was energetically preferred. This agrees with results of other theoretical investigations of MnCo [Nog96] and of MnFe [Spi00a]. In MnCo as well as MnFe the X atoms (X=Co, Fe) order ferromagnetically, while the Mn atoms couple antiferromagnetically with respect to the X atoms. The resulting magnetic moments per atom are compiled together in Table 5.1. However, not all calculations could be performed within the same geometrical arrangement consisting of empty layer, $c(2\times 2)$ compound layer, and 5 substrate layers. $c(2\times 2)$ MnCo and $c(2\times 2)$ MnFe were, therefore, calculated without an empty layer. An inclusion of this layer may slightly change the total energy with the effect that ferromagnetic solutions become energetically preferred. Furthermore, the calculations were performed with the lattice constant of fcc Cu although the X-metals grow on Cu(001) in a tetragonal distorted arrangement.

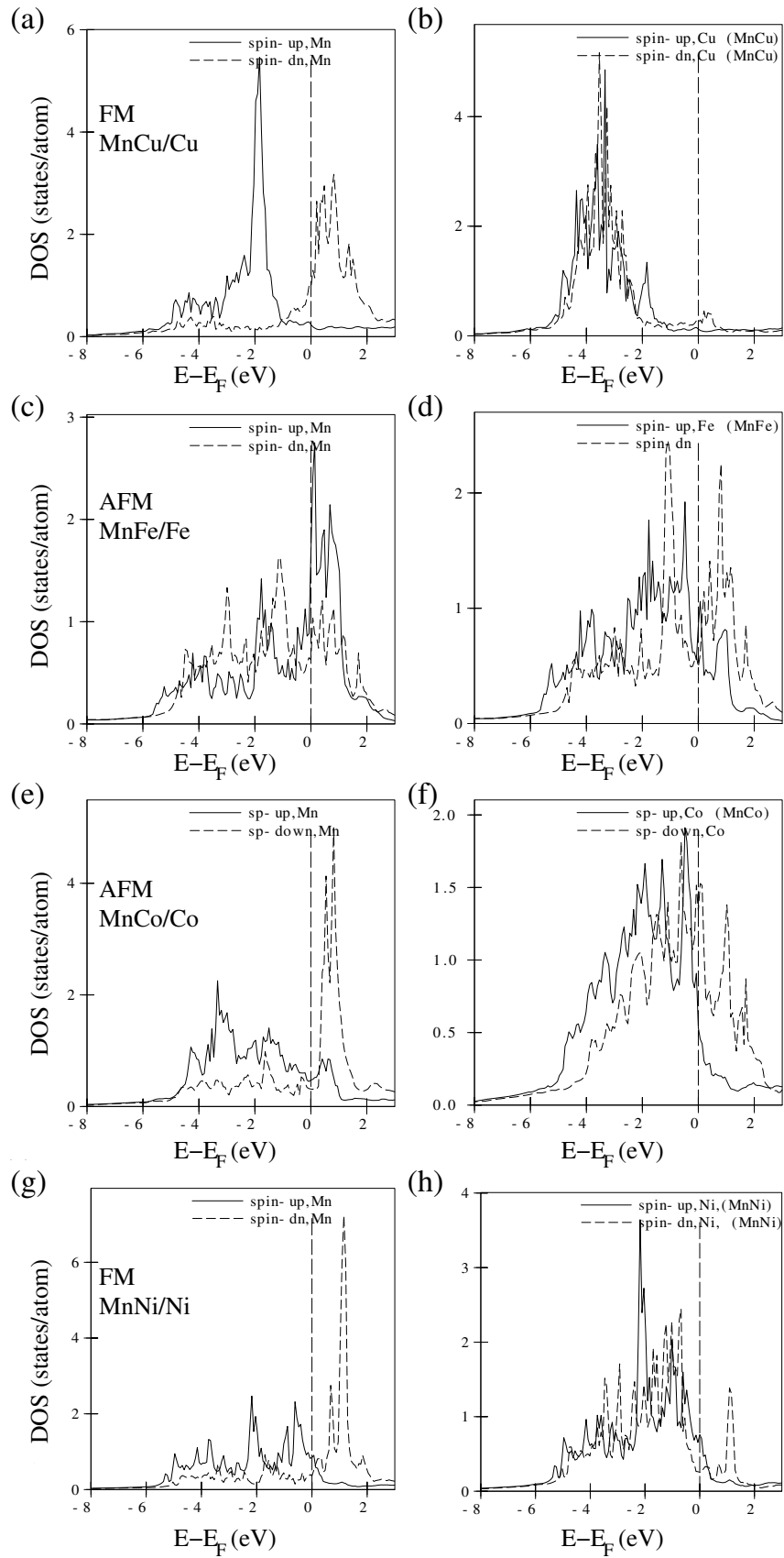


Figure 5.3: Density of states at the Mn (left) and X atoms (right) of the $c(2 \times 2)\text{MnX}/\text{X}(001)$ surface layer ($X = \text{Cu}, \text{Fe}, \text{Co}, \text{and Ni}$).

Structure	Mn atom [μ_B]	X atom [μ_B]	1. X layer [μ_B]
FM $c(2\times 2)$ Mn/Cu(001)	3.83	0.095	<0.01
AFM $c(2\times 2)$ Mn/Fe(001)	-2.22	1.01	1.31
FM $c(2\times 2)$ Mn/Co(001)	2.35	1.31	1.58
AFM $c(2\times 2)$ Mn/Co(001)	-2.69	1.02	1.67
FM $c(2\times 2)$ Mn/Ni(001)	2.90	0.19	0.20

Table 5.1: Magnetic moments of the investigated $c(2\times 2)$ MnX systems as calculated with ASA-LMTO.

5.2.2 Growth and structure of Mn on the ferromagnetic fcc (001) surfaces of Fe, Co, and Ni metal

Literature review

A first structural analysis of the Mn/Ni system was carried out by LEED and medium energy electron diffraction (MEED). These experiments showed a $c(2\times 2)$ -LEED pattern for a coverage of half a monolayer of manganese [Wut93a] that was attributed to the formation of a $c(2\times 2)$ MnNi surface compound using dynamic LEED [Wut93c]. As in the case of the $c(2\times 2)$ MnCu surface compound, also for $c(2\times 2)$ MnNi the Mn atoms were found to be arranged with an outside corrugation of 0.25 Å (Mn in $c(2\times 2)$ MnCu: 0.3 Å) [Wut93c]. Soft X-ray absorption measurements were used to analyse the local magnetic order of the Mn atoms. Mn was found to be in a high spin ground state and ferromagnetically aligned to the underlying Ni layer independent of the magnetisation direction of Ni: In-plane for a Ni(001) crystal and perpendicular to the surface for a 20 ML Ni/Cu(001) thin film [O'B94a, O'B95]. For the latter result epitaxially grown Ni/Cu(001) films were used for Mn growth studies [O'B95, Rad97a]. SPIŠÁK and HAFNER used a LSDA method with generalised gradient approximation (GGA) to analyse two and three dimensional compounds of MnNi [Spi99]. For the intermetallic MnNi *bulk* compound a layered antiferromagnetic high spin ground state with Mn moments of up to $\pm 3.2 \mu_B$ and non-magnetic Ni atoms was predicted. A high spin ferromagnetic order with Mn moments of $3.9 \mu_B$, however, was concluded for a $c(2\times 2)$ MnNi/Ni(001) monolayer [Spi99].

For the Mn/Co/Cu(001) system recently the formation of a $c(2\times 2)$ LEED pattern after deposition of half a monolayer of Mn onto a Co/Cu(001) film was reported [Cho98, Cho99]. The authors interpreted their LEED data in terms of a $c(2\times 2)$ MnCo surface compound. They give, however, no experimental proof for this assignment except that the experimental details are similar to those obtained for $c(2\times 2)$ MnCu. Contrasting to the above result, a previous study of the Mn/Co/Cu(001) system did not found any LEED pattern that differs from $p(1\times 1)$ [O'B94b]. Using SMOKE [Cho99] and circular dichroism [O'B94b] both groups found the Mn atoms to be ferromagnetically aligned to the Co layers.

The antiferromagnetic coupling of Mn to the Co layers that was found in the present work is *not* in disagreement with these experiments, since SMOKE is not element-specific and cannot discriminate the contribution of Mn and Co to the signal. The element-specific dichroism measurement, on the other hand, was not performed for a $c(2\times 2)$ structure. Tight binding calculations predict a competition between an in-plane antiferromagnetically ordered $c(2\times 2)$ configuration and one, in which a ferromagnetic MnCo overlayer is antiferromagnetically ordered to the underlying Co [Nog96].

γ -FeMn reveals a fcc structure with an antiferromagnetic long range order as observed by KOUVEL and KASPER [Kou63]. For the magnetic structure a so-called collinear type-I antiferromagnetic configuration or a configuration consisting of a unit cell of 4 atoms with magnetic moments directed toward the center of the cell was concluded from neutron diffraction measurements [Kou63]. Several theoretical investigations were carried out to determine the magnetic ground state. Most recently SPIŠÁK and HAFNER found a ground state with parallel Fe moments and canted Mn moments forming an angle of 128° [Spi00a]. However, they also found that a uniform collinear antiferromagnetic order is built up, if substitutional disorder in the system is present [Spi00a]. To our knowledge, so far no investigations of the Mn/Fe/Cu(001) system has been performed.

Present results

Before all, the aim of this work was the investigation of the electronic structure of the compounds. However, since crystallographic structure, magnetic properties, and the electronic structure are related to each other, some aspects of the growth process have to be considered as well.

Here, the ferromagnetic metals Fe, Co, and Ni were deposited with coverages between 2 ML and 7 ML onto a clean Cu(001) crystal at room temperature. Subsequently, these two-layer systems were exposed to the Mn. In order to minimize contamination effects, all overlayer systems were measured immediately after preparation. The Fermi surface and the band structure were usually probed at the same photon energy. For another photon energy, the system was prepared again starting from the clean Cu(001) surface. The acquisition time for one stack was around 4 hours. For each $h\nu$ contaminations were checked in the beginning and at the end of the experiment by taking valence-band photoemission spectra with HeI light, where the oxygen $2p$ cross-section is nearly maximal. While no contaminations were found for freshly grown films sometimes after the measurement traces of a sample deterioration were detected. Usually in these cases the experiment was repeated until no further contaminations were observed. Note that both the band structure and the Fermi surface cuts were found to be unaffected by small amounts of contamination. The thickness of the ferromagnetic films were determined by micro-balances that were calibrated with the manganese source. Thereby the fact was used that the deposition of Mn on Cu(001) results in

a $c(2\times 2)$ LEED pattern best visible for exact half a monolayer. Different sticking factors were not considered. Since the evaporators were placed at different points characterised by different distances with respect to the micro-balances, geometrical aspects were accounted for. For the Fe/Cu system, the thickness can easily be proved by the thickness-dependent superstructures in the LEED pattern [Mül95]. For the other two systems, a comparison with published photoemission results was used as a further test.

Mn/Fe/Cu(001)

To our knowledge no results of investigations of this three-layer system were published up to now. In the present study the growth of Mn on Fe/Cu(001) was tested for two different Fe/Cu(001) coverages: One for a 4 ML Fe/Cu(001) stack with a (5×1) superstructure in the LEED pattern, the other one for a 6 ML Fe/Cu(001) stack with a (2×1) LEED pattern. Fig. 5.4 shows a set of LEED images for the 4 ML (5×1) Fe/Cu(001) stack before and after Mn deposition. The LEED patterns obtained for the Fe/Cu(001) stack were not as sharp as previously reported in Refs. [Mül95, Xho92], where best quality films were grown by deposition at substrate temperatures of 100 K followed by annealings at room temperature [Ste88]. Such a procedure was not carried out in the present study in order to minimise preparation time. Deposition of half a monolayer of Mn yields a $c(2\times 2)$ superstructure with LEED spots that are only slightly broader than the ones of the Fe/Cu(001) substrate. Mn deposition onto a 6 ML (2×1) Fe/Cu(001) system reveal, however, not very sharp $c(2\times 2)$ LEED spots *and* less intense $p(2\times 2)$ spots *as well*. There exist mainly two possibilities for the occurrence of a $p(2\times 2)$ LEED pattern: *(i)* a different crystalline structure, or *(ii)* an antiferromagnetic ordering of the surface. For antiferromagnetic systems additional (less intense) $c(2\times 2)$ LEED spots are expected [Tam88]. An additional $c(2\times 2)$ overstructure to the already existing $c(2\times 2)$ pattern of the Mn/Fe/Cu(001) system would produce a $p(2\times 2)$ LEED image. The thicker (2×1) Fe/Cu(001) film was found to order antiferromagnetically in the Fe layers with the exception of a ferromagnetic top layer [Mül95]. This top layer, however, becomes destroyed upon Mn deposition. Since our theoretical investigations suggest antiferromagnetic coupling of Mn to the fcc Fe(001) film, we assign the obtained $p(2\times 2)$ LEED pattern to antiferromagnetic ordering.

It should be pointed out, that the obtained superstructures are still not a proof for the formation of a $c(2\times 2)$ MnFe surface compound. The formation of the 2-D surface compound is very probable due to the existence of analogous compounds for Mn/Cu(001) and Mn/Ni(001). Further investigations, such as a LEED I-V analysis or photoelectron diffraction should be used to confirm the compound formation as it was done for the $c(2\times 2)$ MnCu system [Wut93c, Too96].

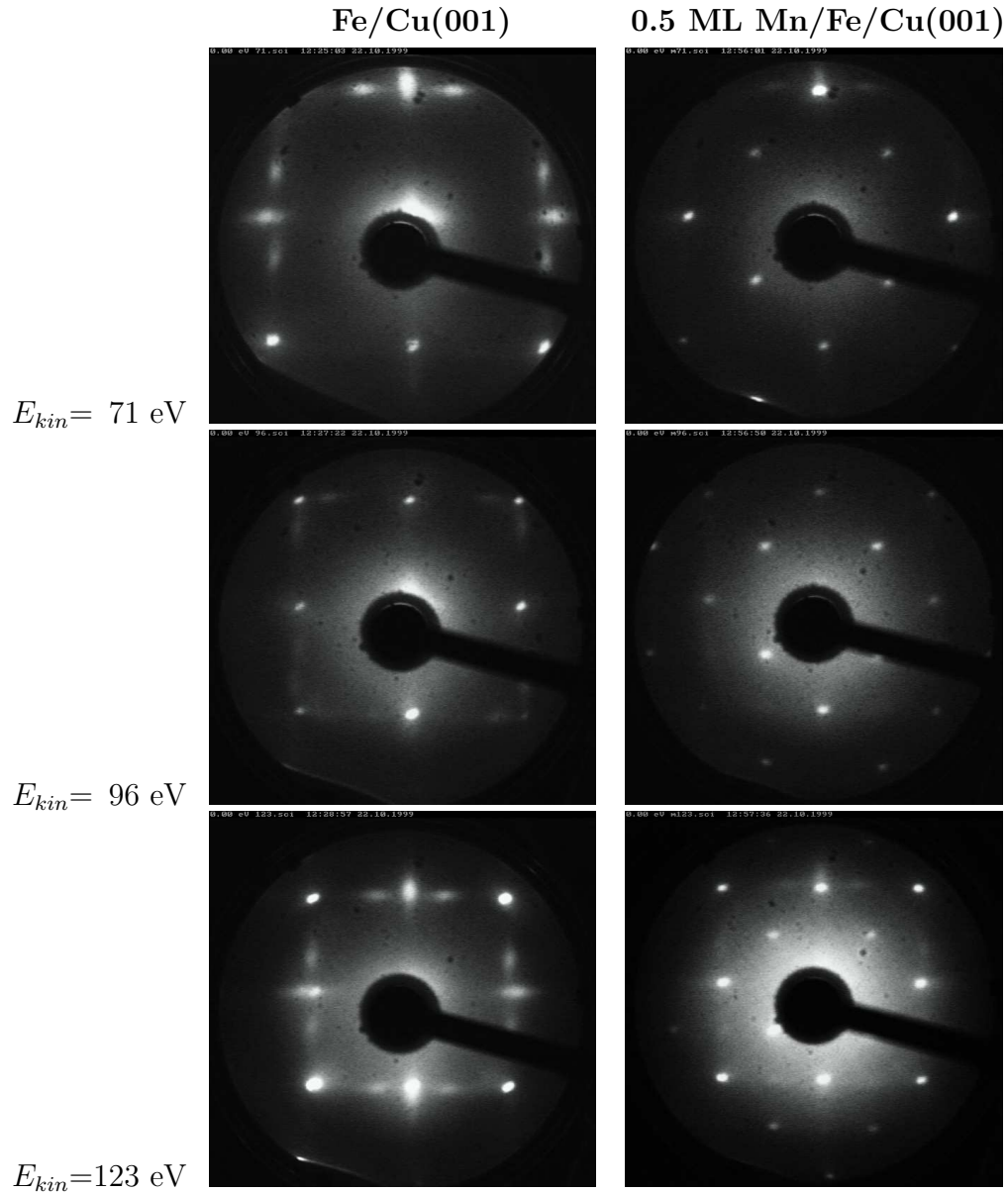


Figure 5.4: LEED patterns obtained for 4 ML Fe/Cu(001) (left) and 0.5 ML Mn/Fe/Cu(001) (right) for kinetic energies 71 eV, 96 eV, and 123 eV.

Mn/Co/Cu(001)

The LEED patterns obtained in the present study for the Mn/Co/Cu(001) system are similar to the ones presented by CHOI *et al.* [Cho98]. The spots, however, turned out to be slightly sharper than reported in this reference and less intense than the ones of the Co/Cu(001) substrate. For the Mn/Ni(001) system it was found that a deposition at higher temperatures (around 400 K) increases the structural order (see below). Such a preparation technique could also be applied for the Mn/Co/Cu(001) system.

Mn/Ni/Cu(001) and Mn/Ni(001)

Manganese growth on Ni(001) and Ni/Cu(001) systems was already studied in details [Wut93a, O'B95]. Also in these cases additional $c(2\times 2)$ LEED spots were obtained at a coverage of 0.5 ML Mn. Room temperature deposition of Mn onto Ni(001) yields LEED spots that are about three times broader than the Ni(001) $p(1\times 1)$ ones [Wut93a]. The quality of the samples can be improved by deposition at higher substrate temperature (around 400 K) [Wut93a, Rad97a]. In the present work the latter was achieved by Mn deposition directly after the necessary sample annealing after ion etching. This procedure gave identical sharp and intense $p(1\times 1)$ and $c(2\times 2)$ LEED spots for 0.5 ML Mn/Ni(001).

5.2.3 Electronic structure of 0.5 ML manganese deposited on the fcc (001) surfaces of Fe, Co, and Ni

Fig. 5.5 shows photoemission spectra of a 6 ML (2×1) Fe/Cu(001) stack taken with a photon energy of 21.2 eV in both high symmetry directions: $\bar{\Gamma}\bar{M}_{p(1\times 1)}$ and $\bar{\Gamma}\bar{X}_{p(1\times 1)}$. A comparison with the PE spectra of Cu(001) of Fig. 2.4 indicate that the features between 2 and 5 eV binding energy originate from bands of the Cu(001) substrate that are still visible in spite of a coverage of 6 ML of Fe. This is rather surprising, since (i) the valence band photoemission signal at this photon

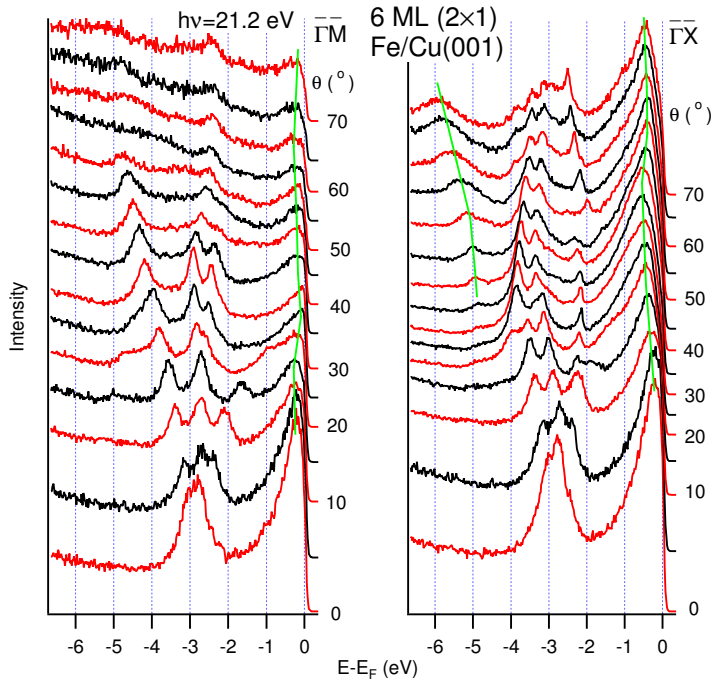


Figure 5.5: Photoemission spectra of a 6 ML (2×1) Fe/Cu(001) stack taken at a photon energy of 21.2 eV for several emission angles in both high symmetry directions $\bar{\Gamma}\bar{X}_{p(1\times 1)}$ and $\bar{\Gamma}\bar{M}_{p(1\times 1)}$.

energy is rather surface sensitive and (ii) the structural investigations resulted in completely Fe covered Cu(001) surface. A simple model calculation, however, will show that our result is not in conflict with the assumption of a perfect 6 ML overlayer of Fe. First, we have to take into account the mean free path of the electrons, Λ , that corresponds to 3.4 ML at a kinetic energy of 13.5 eV (Cu 3d bands) [Den79]. Assuming an exponential intensity decrease of the signal with depth x , the photoemission intensity of the Cu 3d substrate and the Fe overlayers can be estimated to

$$I_{Fe} \propto \int_0^a e^{-x/\Lambda_{Fe}} dx \propto \Lambda_{Fe} \cdot (1 - e^{-a/\Lambda_{Fe}}) \quad (5.1)$$

$$I_{Cu} \propto e^{-a/\Lambda_{Fe}} \cdot \int_0^\infty e^{-x/\Lambda_{Cu}} dx \propto \Lambda_{Cu} \cdot e^{-a/\Lambda_{Fe}} \quad (5.2)$$

where a denotes the overlayer thickness ($a=6$ ML). Supposing identical values of the mean free paths, $\Lambda_{Cu} = \Lambda_{Fe} = \Lambda$, the relative intensity I_{Fe}/I_{Cu} amounts to $(1 - e^{-a/\Lambda})/e^{-a/\Lambda}=4.8$. As a second step, different cross-sections for the 3d states have to be taken into account: The Fe 3d cross-section amounts to only 2/3 of the Cu 3d value [Yeh85], and normalisation to the number of 3d electrons reduces the relative Fe signal additionally by a factor 0.6 (electronic configurations: Fe: [Ar]4s²3d⁶, Cu: [Ar]4s¹3d¹⁰). To summarise, for $h\nu=21.2$ eV the Fe emission should be about two times higher as compared to the Cu emission for the 6 ML Fe/Cu(001) stack. This value is very close to the intensity relation seen in the normal emission spectrum of Fig. 5.5. Since there are still Cu derived spectral features, it is impossible to detect emissions from the exchange split Mn 3d bands, which are expected between 1.55 and 3.7 eV as in the case of Mn/Cu. Thicker films, however, could not be used since a phase transition takes place at 11 ML for Fe/Cu and the quality of the overlayers decreases with thickness.

Nevertheless, in chapter 3.2.3 a new method for the determination of the Mn spin majority band in $c(2 \times 2)$ MnCu was presented that should be applicable also for fcc (001) surfaces of Fe, Co, and Ni. The results obtained by this method for the $\bar{\Gamma}$ point in the second $c(2 \times 2)$ surface Brillouin zone of some overlayer systems including Fe, Co, and Ni are shown in Fig. 5.6. Vertical lines denote the positions of the new peaks induced by manganese. The observation of the new peaks upon Mn adsorption proves that the same method works for the overlayer compounds considered here. Once the method is established, different overlayer systems can be studied in detail.

In the framework of this thesis Fe films of two different thicknesses were studied by PE: A 4 ML (5×1) Fe/Cu(001) and a 6 ML (2×1) Fe/Cu(001) stack. Besides structure, the main difference relates to the magnetic properties. As already mentioned above, in the 4 ML Fe/Cu(001) system the iron layers were found to be ferromagnetically ordered, while the 6 ML Fe/Cu(001) consists of antiferromagnetically ordered layers with the exception of the ferromagnetically coupled

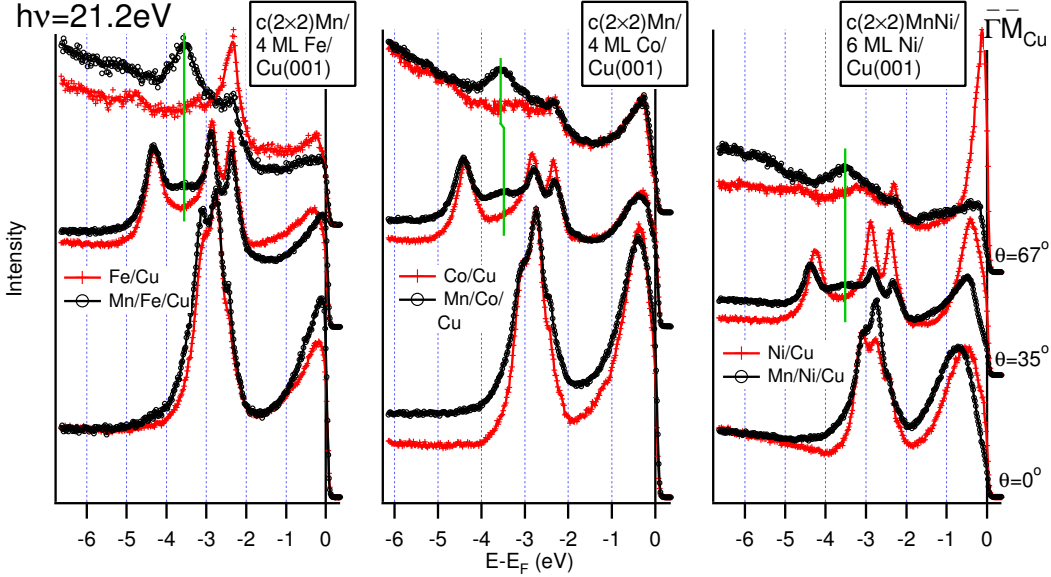


Figure 5.6: PE spectra for pure and manganese exposed Fe/Cu(001), Co/Cu(001), and Ni/Cu(001) stacks measured with a photon energy of 21.2 eV for the $\bar{\Gamma}$ points in the first and the second $c(2\times 2)$ surface Brillouin zone as well as for one emission angle between these points. The spectra were taken along the $\bar{\Gamma}\bar{M}_{p(1\times 1)}$ direction.

top layer [Mül95]. Deposition of 0.5 ML Mn causes a $c(2\times 2)$ and a $p(2\times 2)$ reconstruction of the LEED patterns of 4 and 6 ML Fe/Cu(001), respectively. PE spectra for these compounds measured at the $\bar{\Gamma}$ points in the first and the second $c(2\times 2)$ SBZ can be seen in Fig. 5.7(a). Apart from the intensity variation that is due to the different overlayer thickness, nearly no difference between the spectra of the different stacks can be observed. Also deposition of half a monolayer of Mn does not lead to a distinct behaviour of the two systems. Although different magnetic properties are expected for the substrate films [Mül95], no variations in the electronic structure are observed. This is mainly due to the fact that the Curie temperature T_C is very low for films in the monolayer range and above T_C the samples are not magnetically ordered. Even below T_C magnetic moments order in domains that are usually much smaller than the focus of the analyser used in PE experiments. The result, therefore, is averaged over all magnetic domains³. For the Fe/Cu(001) system, TOBIN *et al.* deduce a T_C value of approx. 220 K for the 4 ML Fe/Cu(001) film [Tob92]. In Ni/Cu(001) and Co/Cu(001) T_C increases approximately linear with the overlayer coverage in this thickness range [Tis94, Sch90]. Supposing also a linear relationship of the T_C -thickness dependence in Fe/Cu(001) a Curie Temperature *above* room temperature is obtained for the 6 ML Fe/Cu(001) stack. Consequences of such a magnetic ordering are, however, neither observed in PE spectra of Fe/Cu(001)

³In spin-resolved photoemission the magnetisation of the sample is induced by an external magnetic field.

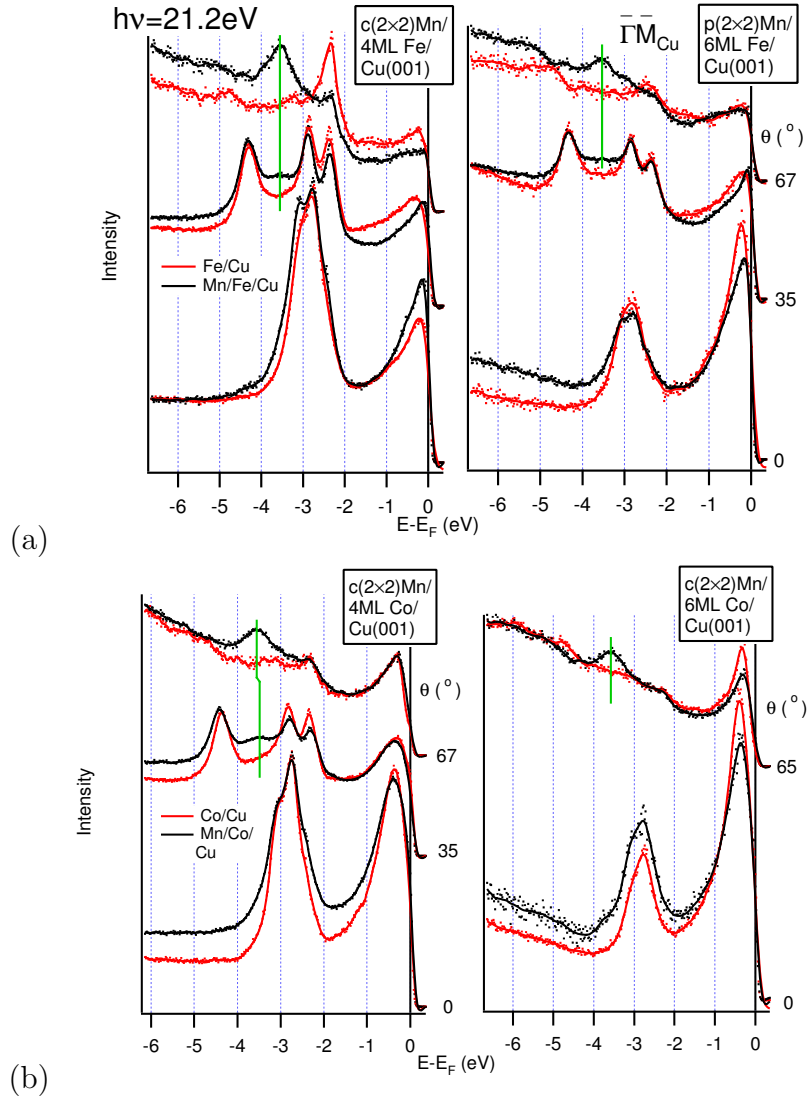


Figure 5.7: PE spectra for 0.5 ML Mn on top of (a) the 4 and 6 ML FeCu(001) and the Co/Cu(001) bilayer systems, respectively, taken at a photon energy of 21.2 eV at the $\bar{\Gamma}$ points in the first and second $c(2\times 2)$ surface Brillouin zone as well as for one \vec{k} -point between these points. The spectra were taken along the $\bar{\Gamma}\bar{M}_p(1\times 1)$ direction.

nor in those of Mn/Fe/Cu(001).

Photoemission, on the other hand, is able to determine the *local* magnetic moment of the Mn atoms, since room temperature measurements far above $T_C=50$ K reveal a spin splitting of 4.85 eV in the Mn/Cu(001) system (see chapter 3.2.3). This local magnetic moment of the Mn atoms arises, because the Mn-Mn distance is enhanced as compared to that in bulk Mn and the overlap of neighbouring Mn d orbitals becomes small. Nevertheless, the Mn $3d$ bands may hybridise with electronic states of surrounding atoms if the binding energies are comparable ($3d$ bands of Cu in $c(2\times 2)$ MnCu). For Mn overlayers on Fe, Co, and Ni, which do not reveal this energy overlap, the Mn $3d$ spin majority band is not expected to hybridise. An equal value of 3.55 eV binding energy observed for this band after

deposition of 0.5 ML Mn onto 4 and 6 ML Fe/Cu(001) implicates that this free local magnetic spin majority band remains unchanged even if the LEED patterns are different. Unfortunately, there do not exist inverse photoemission results that allow to search for the unoccupied Mn 3*d* spin minority band and to estimate the exchange splitting of the Mn 3*d* bands.

In case of the Co/Cu(001) system, the structural and magnetic phenomena are not as complicated as in Fe/Cu(001). Here again 4 and 6 ML coverages of the magnetic material (Co) were used. As for Fe, the Co 3*d* emission appears close to the Fermi energy and increases with coverage (see Fig. 5.7 [b]). Manganese deposition of 0.5 ML does not affect the spectral shape significantly, but leads to a new spectral feature at 3.55 eV binding energy at the $\bar{\Gamma}$ point of the second $c(2\times 2)$ SBZ. In analogy to the Mn/Fe/Cu-system this feature is again assigned to the presence of a Mn 3*d* free local magnetic spin majority band. As for Mn/Fe/Cu, it can be concluded that the Mn atoms at the $c(2\times 2)$ Mn/Co surface are in a high spin ground state like in the $c(2\times 2)$ MnCu surface compound, while the band splitting is most probable differing from that of the latter. A further detail is seen in the PE spectra for the low coverage Mn/Co/Cu(001) system: The Mn induced peak disperses towards the Fermi level when leaving the $\bar{\Gamma}_{c(2\times 2)}$ point. From the shift of 100 ± 50 meV observed between spectra taken at $\bar{\Gamma}_{c(2\times 2)}$ and a \vec{k} -point $2/3$ of the $\bar{\Gamma}\bar{X}_{c(2\times 2)}$ distance a dispersion of about 150 ± 75 meV throughout the SBZ may be extrapolated. This value lies within the same range as the value of 110 ± 60 meV that was observed for the Mn spin *minority* state in $c(2\times 2)$ MnCu [Rad97a] and indicates a high localisation of the Mn spin majority states in Mn/Co/Cu.

The band structure of Mn/Ni(001) was studied in more detail. The reason were discrepancies between our data and those published by RADER *et al.* [Rad97a]. Additionally, there exist further discrepancies in the literature concerning the electronic structure of the Ni/Cu(001) system [Man97, Pam01]. In Fig. 5.8 PE spectra for the 0.5 ML Mn on 3 and 6 ML Ni/Cu(001) stacks as well as on a Ni(001) crystal are presented. As for the Fe and Co systems the 3*d*-emission is found close to the Fermi level. Already upon formation of the first Ni monolayer on Cu(001) Ni bulk like behaviour was reported by MANKEY *et al.* [Man97]. This is in contradiction with the PE results of PAMPUCH *et al.* [Pam01] who found bulk like behaviour at coverages around 3 ML. The PE spectra for Ni/Cu(001) and Ni(001) depicted in Fig. 5.8, however, show that 3 ML are not enough to develop a Ni bulk like behaviour, since the doublet structure characteristic for the Ni(001) spectrum is even not visible for a 6 ML Ni/Cu stack. Mn deposition onto these surfaces produces in all cases a $c(2\times 2)$ LEED pattern, the electronic structure, however, differs between each other. Let us consider first the Ni/Cu(001) films. The Ni 3*d* emission close to the Fermi level is affected by the 0.5 ML Mn. The peak intensities decrease and the peak positions shift to higher binding energies. Such effects were not observed in Fe- or Co-derived systems. A new manganese-induced peak arises at the $\bar{\Gamma}$ point in the second $c(2\times 2)$ SBZ at a

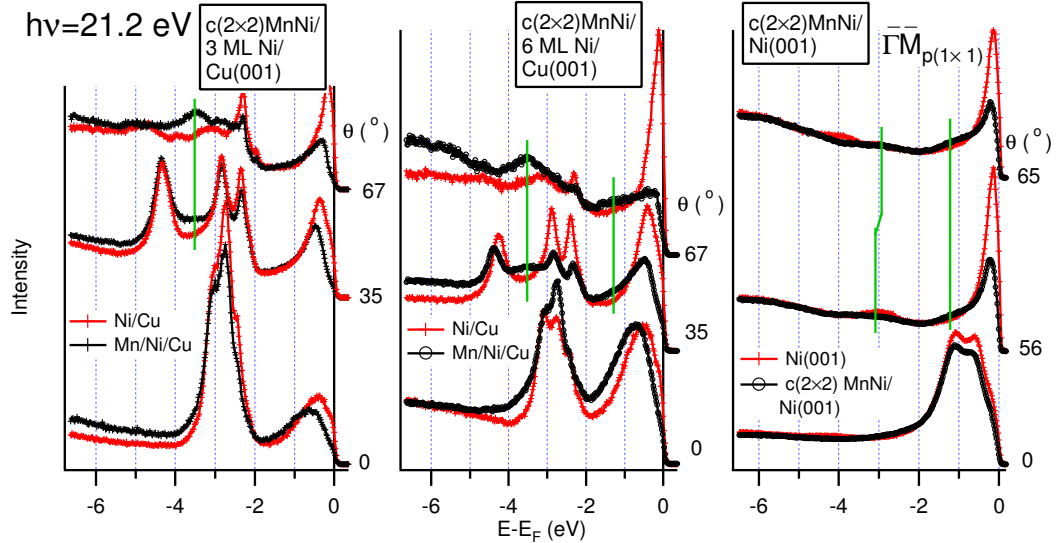


Figure 5.8: PE spectra for 0.5 ML Mn on top of a 3 and 6 ML Ni/Cu(001) bilayer systems and a Ni(001) crystal measured with a photon energy of 21.2 eV at the $\bar{\Gamma}$ points in the first and the second surface Brillouin zone as well as one emission angle between these points. The spectra were taken along the $\bar{\Gamma}\bar{M}_{p(1\times 1)}$ direction.

binding energy of 3.48 eV. RADER *et al.* [Rad97a] found the peak position at 3.2 eV binding energy and assigned it to the Mn 3*d* spin majority states. They used a 25 ML Ni/Cu(001) film as substrate and assigned a bump between the broad Ni emission close to the Fermi level and the secondary electron background to the Mn emission (see Fig. 5.9 [a]). In order to study a possible dependence of the peak position of the film thickness, a Ni(001) crystal was used in the present work as a reference. No differences between the clean Ni(001) and the $c(2\times 2)$ MnNi/Ni(001) data have been observed at the $\bar{\Gamma}$ point of the first SBZ. Using the previously described method of measuring close to the $\bar{\Gamma}$ point of the second SBZ, one has to consider the strongly dispersing Ni *sp* band (peaks at approx. 4.0 eV binding energy for $\theta=65^\circ$ and at 3.0 eV for 56°), that masks possible Mn emissions. The $c(2\times 2)$ MnNi/Ni(001) surface compound reveals additionally a very weak dispersing feature at 3.0 eV, that can be interpreted as a Mn 3*d* spin majority band similar to other investigated $c(2\times 2)$ structures. This weak signal is not monitored at normal emission. This fact can be explained by the increased surface sensitivity at higher emission angles and/or Brillouin zone selection rules as found in graphite by SHIRLEY *et al.* [Shi95]. Another not dispersing peak in the $c(2\times 2)$ MnNi/Ni(001) spectra taken in the region of the $\bar{\Gamma}$ point in the second $c(2\times 2)$ SBZ is observed at about 1 eV binding energy. It can be assigned either to a backfolded Ni band that appears at this \vec{k} -position due to the changed symmetry, to another Mn-derived band, or to a band introduced by a changed magnetic order. Also in the $c(2\times 2)$ Mn/6 ML Ni/Cu(001) spectra this additional feature exists, however, with even lower intensity. For

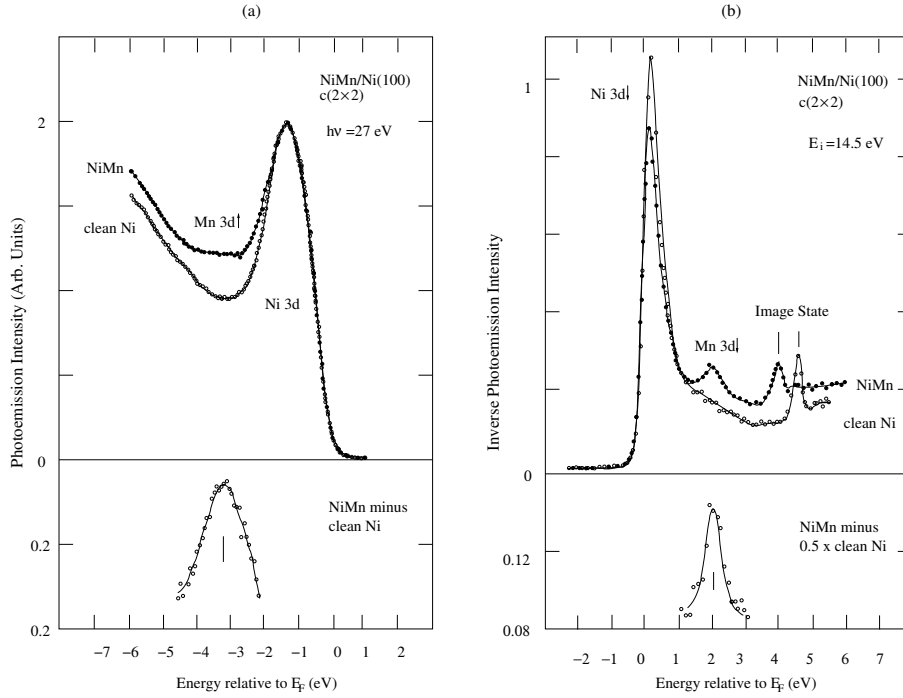


Figure 5.9: Normal emission spectra for 0.5 ML Mn onto a 25 ML Ni/Cu(001) stack (a) and a Ni(001) surface (b) obtained by RADER *et al.* [Rad97a] with photoemission (a) and inverse photoemission (b), respectively.

the $c(2 \times 2)$ MnNi surface compound grown on the thinner Ni film such a peak is not present. This finding excludes the explanation by the backfolded Ni band since the $c(2 \times 2)$ symmetry is characteristic for all synthesised compounds. It does not rule out, on the other hand, the magnetic scenario: In all three cases the magnetic order of the Ni substrate is the same with the magnetisation vector perpendicular to the film surface. Ni/Cu(001) films behave ferromagnetically at room temperature for film thicknesses larger than 5 ML, while for thinner films the Curie-temperature was found to be below room temperature [Tis94]. Therefore, one could attribute the disappearance of the 1 eV binding-energy feature in the thin-film sample (MnNi/ 3 ML Ni) to a lack of magnetic order. However, since in the case of the Mn/Fe/Cu system influences of the magnetic order due to different coverages of the Fe-substrate has not been observed in the PE spectra, also for the Mn/Ni/Cu system such kind of magnetic influence is not very probable.

Hints for the existance of Mn 3d spin majority states at approx. 1 eV binding energy were not only obtained by our theoretical work (see Fig. 5.3) but also by SPIŠÁK and HAFNER, who found in their DOS calculation a broad Mn-derived doublet structure with maxima at approx. 2.3 and 0.9 eV [Spi99]. Therefore we assign the 1 eV feature in MnNi to the occurance of an additional spin majority peak induced by Mn. The maximum spin splitting ΔE_{tot} at $\bar{\Gamma}$ can be calculated using the IPES result of RADER *et al.*, who observed the unoccupied Mn 3d band

Structure	$E(\text{Mn } 3d^\uparrow)$ [eV]	$E(\text{Mn } 3d^\downarrow)$ [eV]	ΔE_{tot} [eV]
$c(2\times 2)\text{Mn/Fe/Cu}(001)$	3.55	-	-
$c(2\times 2)\text{Mn/Co/Cu}(001)$	3.55	-	-
$c(2\times 2)\text{Mn/3 ML Ni/Cu}(001)$	3.5	-	-
$c(2\times 2)\text{Mn/6 ML Ni/Cu}(001)$	3.5	-	-
$c(2\times 2)\text{Mn/25 ML Ni/Cu}(001)$	3.2*	-	-
$c(2\times 2)\text{Mn/Ni}(001)$	3.0	2.05*	5.05
$c(2\times 2)\text{Mn/Cu}(001)$	3.0	1.85*	4.85

Table 5.2: Summary of the Mn $3d$ spin up (\uparrow) and down (\downarrow) band positions for the investigated structures. Values from RADER *et al.* [Rad97a] are marked with a asterisk *.

2.05 eV above the Fermi level (see Fig. 5.9[b]). For Ni ΔE_{tot}^{Ni} amounts to 5.05 eV and is, hence, slightly larger than the value $\Delta E_{tot}^{Cu}=4.85$ eV for the $c(2\times 2)\text{MnCu}$ surface compound.

Table 5.2 presents the occupied and unoccupied Mn $3d$ band positions for the considered systems. It is interesting to note that there are three different values for the Mn/Ni systems: 3.5 eV for thin Ni layers, 3.2 eV for a thick layer, and 3.0 eV for the Ni(001) bulk sample. Two possible explanations for such a behaviour are: (i) a decreased Mn-Mn distance and (ii) a magnetic influence of the substrate. It seems to be most likely that the local magnetic order that is determined by the Mn-Mn distance is responsible for these energy positions since here the Cu lattice parameter of 3.61 Å is maintained in the surface plane for thin Ni films. For thicker Ni films (25 ML) as used by RADER *et al.* it may already somewhat relax with a lattice constant lying inbetween the ones of Cu and Ni. The even smaller lattice constant of 3.52 Å of Ni(001) leads to an increased d - d interaction of neighbouring Mn atoms, decreasing simultaneously the free-atom like Mn magnetic moment characteristic for higher Mn-Mn distances. If the Mn-Mn distances determine the spin band position, this could also explain the nearly identical value of binding energy (3.5 eV) observed for all studied films.

5.3 Fermi surface investigations for pseudomorphic grown $c(2\times 2)\text{Mn/X/Cu}(001)$ structures (X=Fe, Co, Ni)

In chapter 3.2 it was shown that there exists also occupied spin minority states close to the $\bar{X}_{p(1\times 1)}=\bar{M}_{c(2\times 2)}$ point in the surface Brillouin zone of $c(2\times 2)\text{MnCu}$. The consequence of this finding is that the spin up and down bands are not totally separated by the Fermi level as believed in former work. For the $c(2\times 2)\text{Mn/X}(001)$ systems (X= Fe, Co, and Ni) analogous investigations are much more complicated

since these materials are characterised by partly filled $3d$ bands that are situated close to the Fermi level. Contributions of Mn are, therefore, difficult to discriminate. Intensity variations near the Fermi level in the Mn/Ni/Cu(001) system, however, give rise to suspicions that there exists some influence of Mn. Conventional band-structure mapping is not very well suited to search for such details due to the masking of the Mn- $3d$ -derived features by the intense $3d$ bands of the substrates. Therefore, Fermi-surface mapping was used, a method, which is much more sensitive to variations near the Fermi level sampling the electronic structure in two dimensions and not only in the high symmetry directions as by photoemission investigations. A problem encountered in the present work was the lack of available conventional photoemission data and Fermi-surface mappings of the simple X/Cu(001) substrate layer system (X=Fe, Co, Ni). Therefore, also the simple Fe, Co, and Ni/Cu(001) systems have been studied in the framework of the present thesis and the respective results will be presented briefly.

5.3.1 $c(2 \times 2)$ Mn/Fe/Cu(001)

Fig. 5.5 displays valence band spectra of a 6 ML Fe/Cu(001) stack taken with a photon energy of 21.2 eV. The features close to the Fermi level originate from Fe $3d$ -derived bands. The most important detail for the following consideration is the fact that there is nearly no visible dispersion of the envelope of the Fe-derived emissions. This is due to the fact that the dispersive properties of the individual subbands are masked by the superposition of the respective emissions. The dispersion of the individual subbands, however, can be deduced from the intensity variations of the $3d$ peaks. This point of view is supported by the Fermi-surfaces mapping that reveal rich structure as it will be shown below. The problem concerning the analysis of the Fermi surfaces presented here is the strong light polarisation effect that was described in section 2.2.3. This makes a normalisation of the intensities at the Fermi energy very difficult. Fig. 5.10 shows two possibilities for such a normalisation for the Fe/Cu(001) system; (i): normalisation to a continuous background intensity upon the polar angle variation, (ii): normalisation to the d band intensity along the $\bar{\Gamma}\bar{X}$ direction so that a step-less d band intensity occur. In both cases the symmetry of the polar-cut curves is identical, however, the intensity distributions are quite different. When using the normalisation to the weaker features which are mainly dominated by the broad Fe sp band, the intensity at large emission angles becomes usually enhanced. On the other hand, the absolute calibration of the intensity distributions is not so important here as this work focuses only on the differences of the Fermi surface with and without Mn overlayer. In the following, the normalisation to the d band intensity is used in order to emphasise a step-less intensity of the d bands since the Fermi surface is mainly formed by these bands.

The 6 ML Fe/Cu(001) Fermi surface measured with 21.2 eV as well as 40.8 eV photon energies is totally different from the Cu(001) Fermi surface seen in

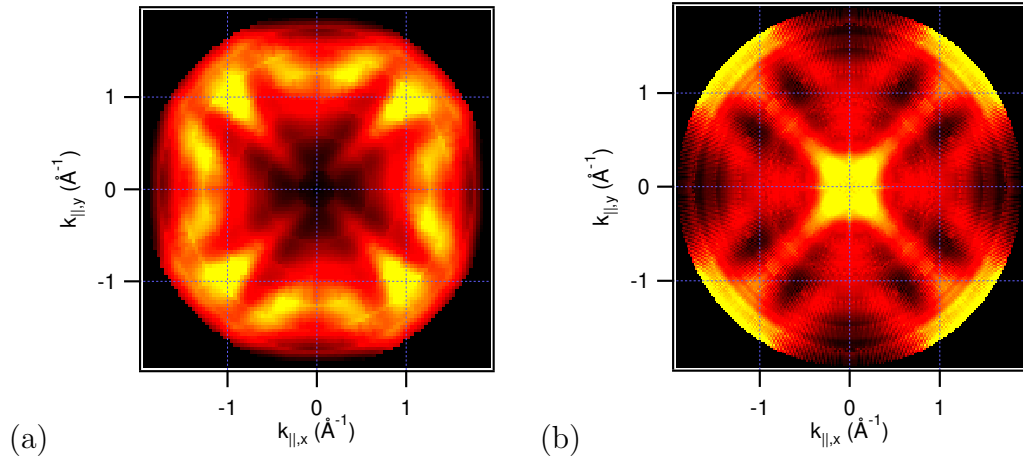


Figure 5.10: Fermi-surface cut for 6 ML Fe/Cu as measured with 21.2 eV photon energy: **(a)**: normalisation to the background of *sp*-derived emissions ; **(b)**: normalisation to the intensity of the *d* bands.

Fig. 2.19. This implies that *sp* bands of the Cu substrate do not contribute significantly to the Fermi surface image⁴. Fig. 5.11 shows the experimental and calculated Fermi surfaces as obtained by our FPLO band-structure calculations [Koe99] for the photon energies of 21.2 eV and 40.8 eV. Two different magnetic structures were assumed for calculations: A ferromagnetic and a layered antiferromagnetic ground state⁵. The experimentally observed structure of antiferromagnetically coupled layers with two ferromagnetically ordered top layers was not considered in view of the large unit cell and the resulting running time of the calculation. A clear assignment of the experimental structures to the theoretical results is not possible. The ferromagnetic result is slightly closer to the experiment than the antiferromagnetic one since at least for $h\nu=21.2$ eV the experimentally observed diagonal structure of the intensity distribution is correctly reproduced. This might be expected since emissions from the two ferromagnetically coupled surface layers will dominate the experimental results masking weaker contribution from the antiferromagnetically ordered bulk layers. However, results of the calculations may change drastically if the tetragonal distortion of the Fe film and variation of the inner crystal potential are considered. Even small variations of these parameters change the k_{\perp} position of the final state. Since there are many rather weak dispersing *3d* bands forming the Fermi surface, such variations may completely change the Fermi surface. Apart from this fact the real magnetic structure which is not considered in the calculations as well as surface and interface effects make the analysis rather complicated. There are only very few differences visible between the Fe/Cu(001) and the

⁴Note that the *3d* copper bands were still visible in the conventional PE spectra.

⁵While the ferromagnetic Fe is calculated in a fcc lattice with $Fm\bar{3}m$ symmetry (space group 225), the layered antiferromagnetic lattice is simple tetragonal with $P4/mmm$ symmetry (space group 123) and two antiferromagnetically ordered atoms as a basis.

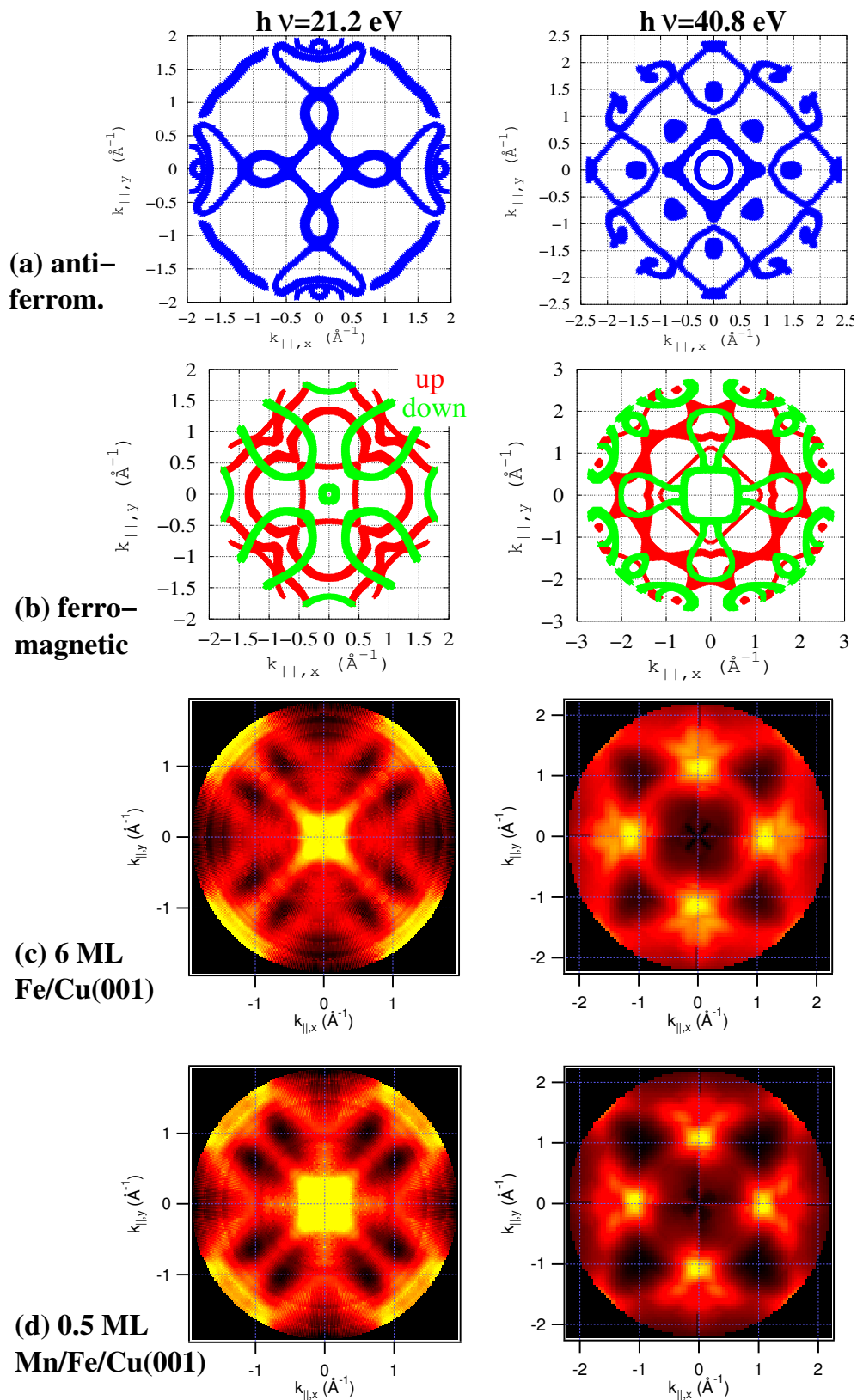


Figure 5.11: Calculated Fermi-surface cuts of a fcc-Fe(001) assuming (a) layered antiferromagnetic and (b) ferromagnetic ordering as compared to the experimentally observed cuts for 6 ML Fe/Cu (c) and $c(2\times 2)$ Mn/6 ML Fe/Cu (d) taken at the photon energies of 21.2 eV and 40.8 eV, respectively. For ferromagnetically ordered Fe, the spin up and down sheets are shown by dark and light colours, respectively.

$c(2\times 2)$ Mn/Fe/Cu(001) Fermi-surface cuts. This observation suggests that there are no new Mn-derived bands crossing the Fermi edge. It was shown that in the case of $c(2\times 2)$ MnCu the intensity of the additional structures at the Fermi level is low. For Fe/Cu, on the other hand, the intensity of the Fe 3d bands that cross the Fermi edge is several orders of magnitude higher and, therefore, contributions from low intense bands are hardly to detect.

5.3.2 $c(2\times 2)$ MnCo/Cu(001)

As in the case of Fe/Cu fcc Co-derived bands do not disperse strongly near the Fermi energy. The Fermi surface cuts reveal, however, several well separated fine structures. The characteristic Fermi surface for fcc Co is already observed for 1 ML Co/Cu(001) [Cas96]. Fig. 5.12 presents the Fermi-surface mappings as measured with 21.2 eV and 40.8 eV photon energies for the 6 ML Co/Cu(001) stack and the $c(2\times 2)$ Mn/Co surface formed upon deposition of half a monolayer of manganese on top of the Co film. Model calculations were only performed for the ferromagnetic ground state compatible with earlier theoretic and experimental results on the Co/Cu(001) system. To account for the mentioned tetragonal distortion of the grown Co film calculations were performed for two different lattices, a simple fcc lattice with the Cu(001) lattice parameter and a tetragonal distorted fcc lattice with a Cu(001) lattice constant in the plane ($a=3.605$ Å) and a decreased lattice constant perpendicular to the surface ($c=3.425$)⁶, adjusted in the way that the unit cell volume is the same as in hcp Co. The Co Fermi surface is formed by d and sp bands containing spin minority as well as spin majority states, however, for the d bands only spin minority bands cross the Fermi energy (the spin majority bands are completely occupied). The calculated band structure at the Fermi energy (Fermi surface) perpendicular to the surface in the two high symmetry direction of the SBZ is displayed in Fig. 5.13(a). With a photon energy of 40.8 eV the normal emission measurement is very close to the Γ point of the 3-D Brillouin zone, where no bands are expected from theory. The band that crosses E_F closest to the Γ point in $(10)=\bar{\Gamma}\bar{X}_{p(1\times 1)}$ direction leads to a quadratic feature in the calculated Fermi surface map of fcc Co that crosses the k_x, k_y -axis at about ± 0.4 Å⁻¹. In the calculation for the fct Co lattice, on the other hand, this band crosses the Fermi level exactly at Γ . In the present experiment such a structure is not reliably monitored. HOCHSTRASSER *et al.*, on the other hand, observe a very broad region of high PE intensity around Γ and interpret this finding as due to an increased d -hole pocket as compared to the case of Ni/Cu(001) [Hoc99]. CASADO measured the Fermi surface with a photon energy of 45 eV sampling nearly the same region very close to Γ and did not find evidence for high intensity close to the Fermi level [Cas96]. The reason for this discrepancy in the experimental findings remains puzzling. The only states that might cause this region of high intensity near the Γ point originate from

⁶The lattice is body centred tetragonal with $I4/mmm$ symmetry (space group 139).

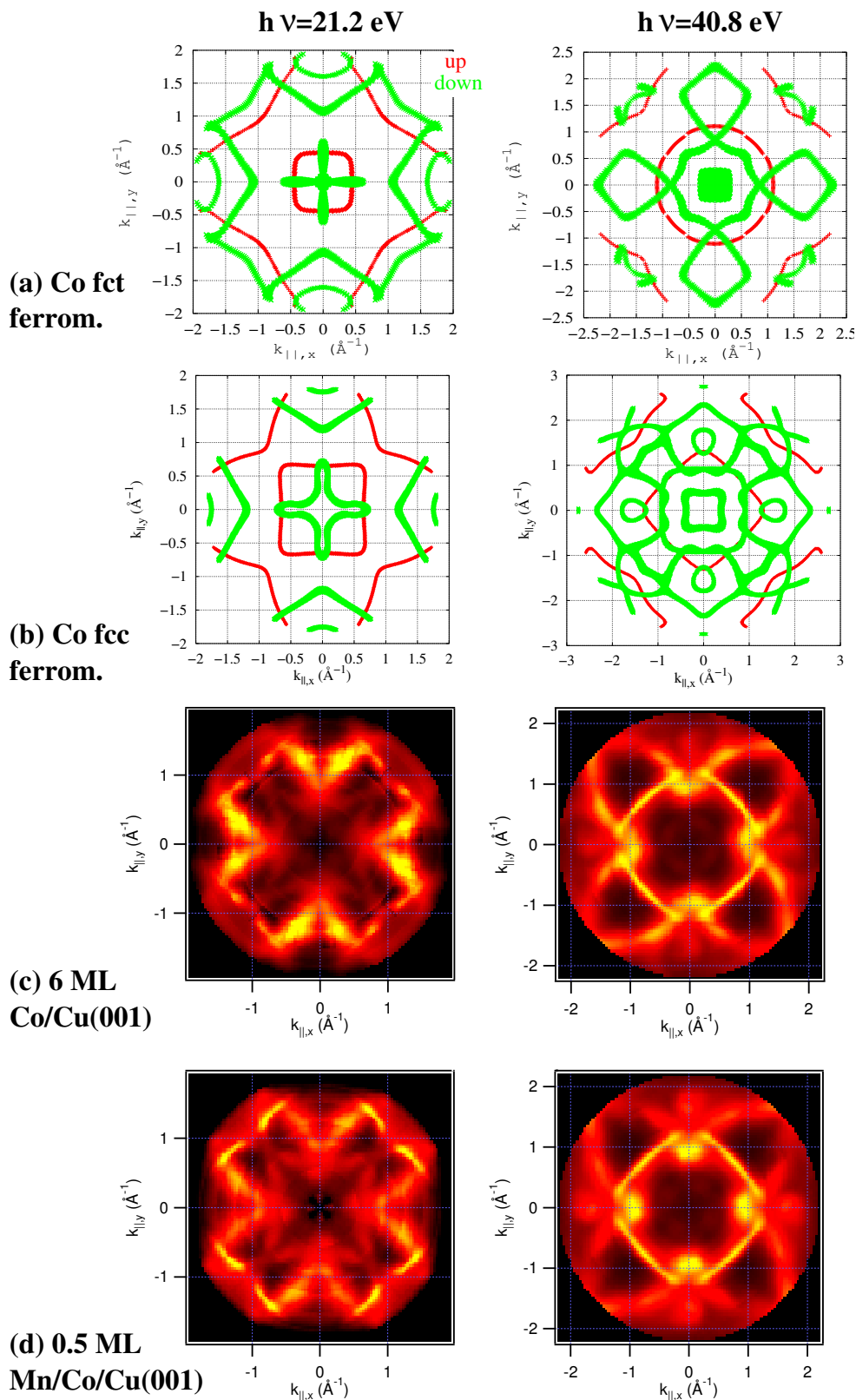


Figure 5.12: Theoretical Fermi-surface mappings for a fct Co(001) (a) and a fcc Co(001) (b), both ferromagnetically ordered, compared to the experimentally measured cuts for 6 ML Co/Cu (c) and half a Mn monolayer on top of 6 ML Co/Cu (d) for the photon energies of 21.2 eV and 40.8 eV. For the theory, the spin up and spin down sheets are shown by dark and light clours, respectively.

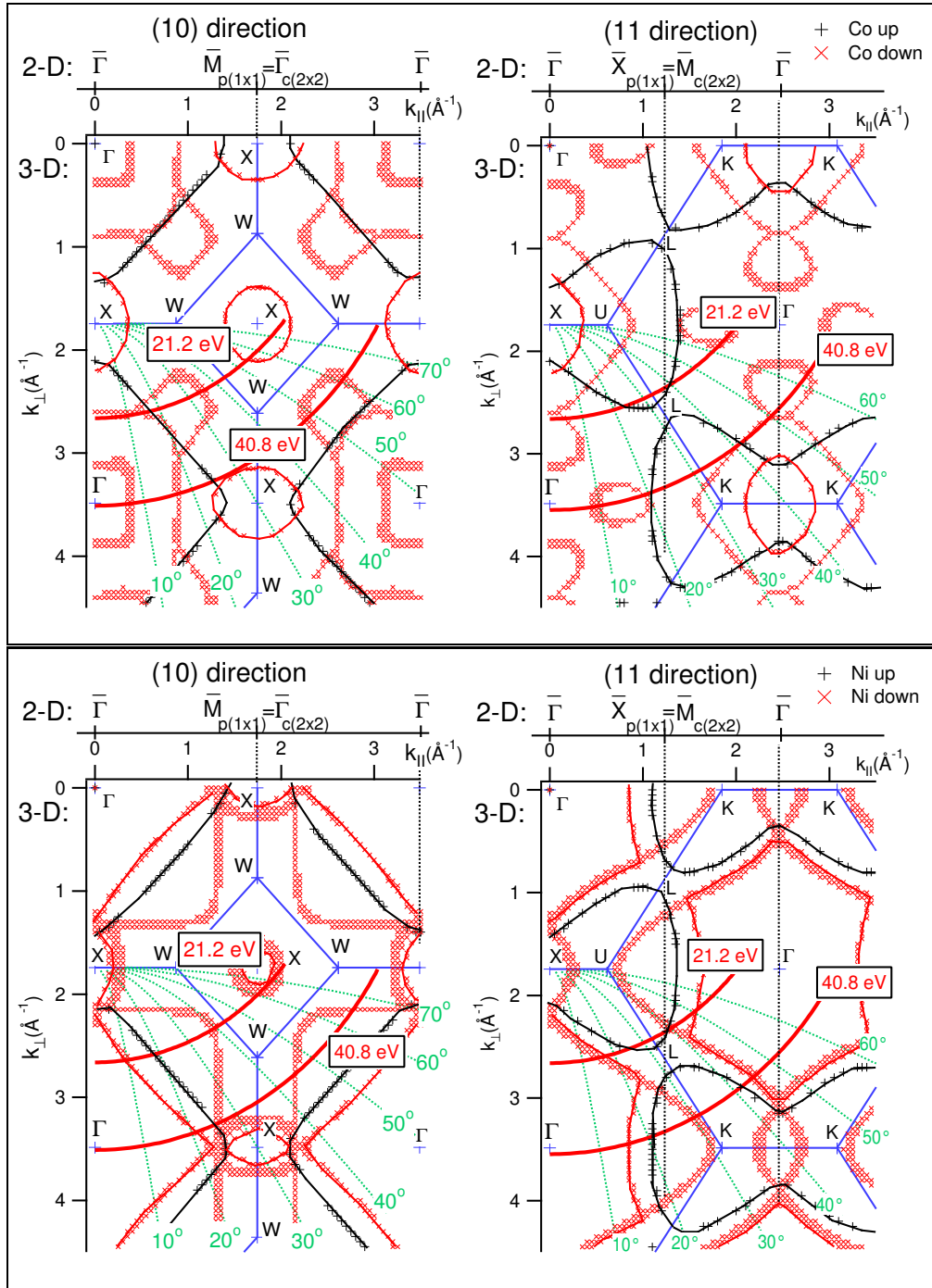


Figure 5.13: The theoretical Fermi-surfaces cuts of ferromagnetic fcc Co (top, $1.61\mu_B$) and Ni (bottom, $0.59\mu_B$). Solid lines denote sp character while open crosses mark d character bands. Regions sampled with HeI and HeII photoemission are shown by parts of circles.

the spin minority Γ_{12} band with Δ_1 symmetry in $\bar{\Gamma}\bar{X}$ direction. Transitions from this band are *not* forbidden (as believed by CASADO) by the symmetry selection rules and should be observable in experiments at 40.8 eV photon energy. In our Fermi-surface cut measured at this energy there is in fact a very weak structure

close to the theoretically expected quadratic shape of the Fermi surface crossing near $\bar{\Gamma}$. The low intensity of the signal is, however, in sharp contrast to the high intensity observed by HOCHSTRASSER *et al.* [Hoc99]. A possible explanation for these different results may be based on the large energy window of 400 meV used in [Hoc99] that is not particularly suited for Fermi-surface measurements. Usually, energy windows in the range of the energy resolution of the analyser are used with values ranging between 50 meV and 100 meV. Otherwise all bands within a 400 meV window below E_F will contribute to the signal, and for systems with flat $3d$ bands additional structures are included in the Fermi surface mapping that usually appear only at higher binding energies.

Other structures are well reproduced by the experiment: The spin majority sp bands forming at $h\nu=40$ eV the nearly circular structure in the Fermi surface cuts in Fig. 5.13(a) are superimposed by the spin minority d bands. Also the circles around the X point formed by the spin minority sp bands that are touched by the free-electron-final-state parabola in $\bar{\Gamma}\bar{M}$ direction (Fig. 5.13[a]) are experimentally well resolved and can be observed in the experimental Fermi-surface mapping at $h\nu=40.8$ eV as ellipses around 1.6 \AA^{-1} . The calculated rectangular shaped spin up structure (sp spin majority band) that appears in the calculated Fermi-surface cut for the fcc Co at 0.7 \AA^{-1} taken for $h\nu=21.2$ eV in $\bar{\Gamma}\bar{M}$ direction is found in the experiment to be slightly distorted. The effect of a decrease of the c axis in the fct structure as compared to the fcc lattice leads to an expansion of the Brillouin zone in the direction normal to the surface and a corresponding change of the band structure. The respective result for the fct structure is shown in Fig. 5.12(a). In fact, an influence of the distortion exists, however, in general the fcc lattice is a reasonable well approximation considering the Fermi surface mappings since the experimental findings are even closer to the calculated fcc results. This, on the other hand, might be related to the not exactly known inner crystal potential of Co/Cu, that in case of the present calculations was approximated by that of Cu. Most often the bottom of the sp band at Γ derived from the band structure calculation is used as a first approximation. In case of Co this sp band is shifted by approx. 1 eV towards the Fermi energy. A different inner potential value changes the final states and, hence, the experimentally observed band structure features. A more detailed discussion of the distortion effect is presented below in the framework of the Mn/Ni/Cu Fermi surface analysis.

As it can be concluded from a comparison of Fig. 5.12(c) and (d), differences between the experimental Fermi-surface mappings for Co/Cu systems with and without Mn are marginal, allowing the same conclusions as derived for Fe/Cu: Manganese bands do not cross the Fermi level and the Co-derived band structure is not affected by the Mn.

5.3.3 $c(2\times 2)\text{MnNi}/\text{Ni}/\text{Cu}(001)$ and $\text{MnNi}/\text{Ni}(001)$

In the calculated Fermi surface cuts in the high symmetry directions $\bar{\Gamma}\bar{X}$ and $\bar{\Gamma}\bar{M}$ presented in Fig. 5.13 a nearly identical shape of the sp spin majority band for Ni/Cu and Co/Cu can be observed. Within a simple rigid-band model, an increase of atomic number (e.g., from Co to Ni) yields to a decrease of the binding energy of the bands, an phenomenon that is confirmed experimentally. If, however, as seen in the Fermi surface cuts in Fig. 5.13, the spin majority Fermi surface of Ni and Co are similar to each other, this finding may be assigned to a different exchange splitting of the spin bands. On the other hand, the Ni spin minority bands differ completely from those obtained in the calculated Fermi surface of Co. Fig. 5.14 shows the calculated and measured Fermi surface cuts for a pure 6 ML Ni/Cu(001) stack and after deposition of half a monolayer of Mn taken with 21.2 eV and 40.8 eV photon energy, respectively. Nearly the same behaviour as for Co is encountered: the calculated and experimental Fermi surface cuts at 40.8 eV photon energy are similar to each other. Furthermore, there exists nearly no difference to the Co/Cu(001) Fermi surface cut measured at 40.8 eV. This points out that the main structures are caused by the spin majority sp bands. Differences can be found in the Fermi-surface cut taken with 21.2 eV photon energy, where an intense ring structure originating mainly from the spin minority d bands or by surface states is found by the experiment at higher emission angles⁷. The spin majority sp band resulting in the “dog bone” structure of the Fermi surface is not well resolved and reveals rather low intensity. On the other hand, HOCHSTRASSER *et al.* observed the sp spin majority bands with the highest PE intensity and additional d spin minority bands contributing to the signal located across the neck of the “dog bone” [Hoc99]. In contrast to their results MANKEY *et al.* concluded that the Fermi surface is mainly formed by d bands when applying a photon energy of 45 eV [Man97].

Like in Co/Cu(001) also in Ni/Cu(001) the effects of the tetragonal distortion of the crystalline structure were studied. The magnetic moments related with fcc and fct structures are very similar to each other (fcc: $1.61\mu_B$, fct: $1.57\mu_B$). Note, however, that the emissions from the d bands are expected to be affected by the crystal structure changes. The effect of the distortion is mainly the different k_{\perp} position sampled in the experiment. Among other things the distortion results in a closed ring structure in the Fermi-surface cut at 21.2 eV photon energy as shown for the calculated fct Ni film of Fig 5.14(a). This ring structure coincides quite well with the experiment while the calculations for fcc Ni do not show such a ring.

Deposition of half a monolayer of Mn does not change the Fermi surface shape dramatically. However, the intensity distribution for the photon energy of 21.2

⁷PLUMMER and EBERHARDT concluded from their PE experiments performed for the Ni(001) surface, that there exist magnetic surface states at the Brillouin zone boundaries [Plu79].

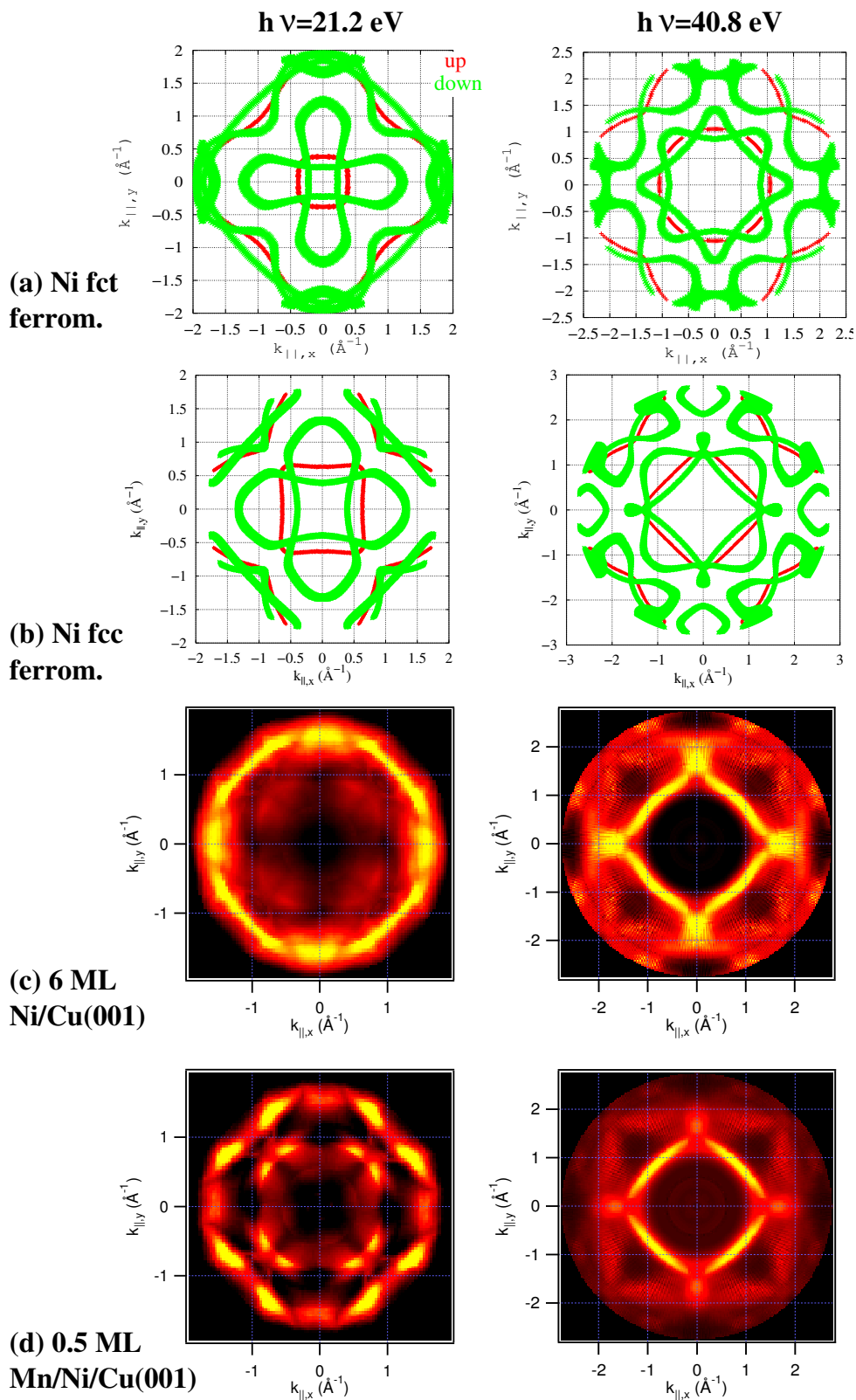


Figure 5.14: Calculated Fermi-surface cuts for ferromagnetically ordered fct Ni(001) (a) and fcc Ni(001) (b) as compared to the experimentally measured cuts for 6 ML Ni/Cu and $e(2 \times 2)$ MnNi/ 6 ML Ni/Cu(001) (d) at the photon energies of 21.2 eV and 40.8 eV, respectively. For the theory, the spin up and spin down sheets are shown by dark and light colours, respectively.

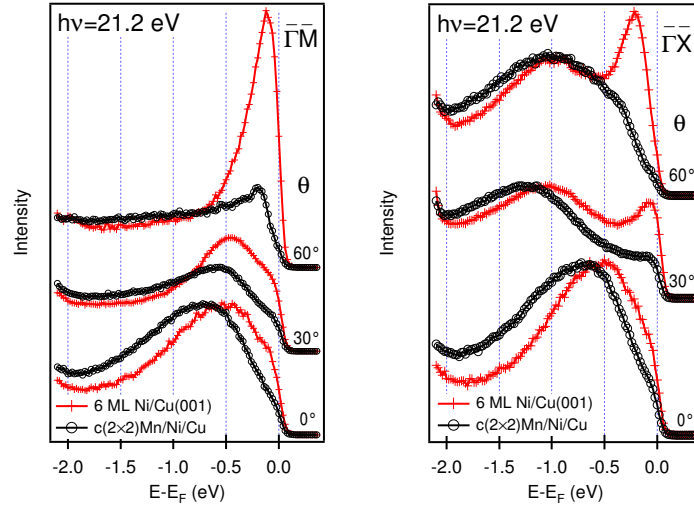


Figure 5.15: Photoemission spectra taken at $h\nu=21.2$ eV for pure 6 ML Ni/Cu(001) and after deposition of half a monolayer Mn forming the $c(2\times 2)$ surface alloy. Emissions from the intense d band or more probable d like magnetic surface states as interpreted by PLUMMER and EBERHARDT [Plu79] close to the Fermi level are strongly quenched upon Mn adsorption.

eV changes. This effect can also be observed in the photoemission spectra that are displayed in Fig. 5.15. Upon formation of the $c(2\times 2)$ MnNi surface compound, not only a strong intensity decrease is observed but also some slight shifts of the d bands are observed. The sp bands are less affected as already seen in the Fermi surface cut taken with a photon energy of 40.8 eV that is mainly determined by bands of this character. In order to study this effect more in details a Ni(001) crystal was used as substrate. Fig. 5.16 shows the Fermi-surface cuts measured at a photon energy of 21.2 eV for Ni(001) and $c(2\times 2)$ MnNi/Ni(001). First, when

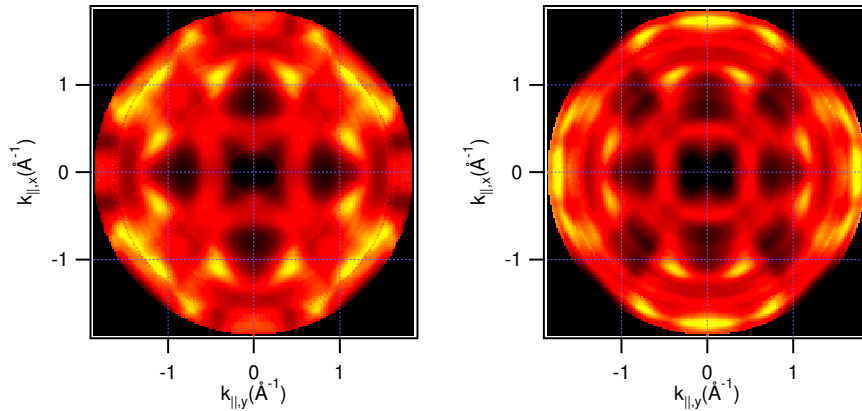


Figure 5.16: Experimental Fermi surface cut of Ni(001) (left) and $c(2\times 2)$ MnNi/Ni(001) (right) measured with a photon energy of 21.2 eV, respectively.

comparing the Fermi-surface cut of Ni(001) and Ni/Cu(001) of Fig. 5.14 one may realise that both Fermi surface cuts are rather different. This confirms our former conclusion that even a 6 ML Ni/Cu films cannot be considered to behave bulk-like. Comparing Ni(001) and $c(2\times 2)$ MnNi/Ni(001), only a few differences are observed between the two cuts that can be attributed to the decrease of the Ni(001) magnetic surface state after Mn adsorption. The influence of the MnNi overlayer on the Ni substrate is, therefore, stronger in case of the thin Ni film than in the case of a bulk Ni(001) crystal. An explanation of this phenomenon may be found in the different magnetic properties of the Ni substrates, since at 7 ML the magnetisation vector changes its orientation from in-plane to perpendicular to the surface, while in Ni(001) the vector again reveals an in-plane direction. Since the considered coverage of 6 ML is very close to the above mentioned value of 7 ML and also some deviations in the coverage calibration are possible, a different magnetisation vector could yield to the observed behaviour. Another possible reason may be related to the different crystallographic structure since Ni(001) has a fcc structure, while Ni/Cu(001) reveals a tetragonal distorted fct lattice. Nevertheless, a clear Fermi surface crossing of new Mn induced bands is not observed in $c(2\times 2)$ MnNi/Ni/Cu(001) and $c(2\times 2)$ MnNi/Ni(001) supporting the hypothesis of separated Mn spin bands in analogy to Mn/Fe/Cu and Mn/Co/Cu.

Chapter 6

Summary and Outlook

The electronic structure of the $c(2\times 2)\text{MnCu}/\text{Cu}(001)$ surface compound was studied in detail by angular resolved photoemission. While previous investigations found new manganese-derived $3d$ majority and minority spin bands well separated from each other by the Fermi level [Rad97a], in this work an occupied spin minority band close to the $\bar{X}_{p(1\times 1)}=\bar{M}_{c(2\times 2)}$ point of the surface Brillouin zone has been obtained by comparison of experimental and theoretical results. The corresponding two-dimensional spin minority Fermi surface was found to be ellipse-like and hole-like around $\bar{X}_{c(2\times 2)}$. An occupation of this spin minority state at $\bar{\Gamma}$ is possible but cannot be confirmed by our measurements. This spin minority states are partially filled only for a nearly perfect $c(2\times 2)\text{MnCu}/\text{Cu}(001)$ surface compound. However, as the magnetic character of the bands was attributed by the theory, a spin resolved photoemission experiment is necessary to make a definitive conclusion about the spin character of the new peaks. Inverse photoemission, on the other hand, can follow the dispersion of the unoccupied spin minority bands.

The $\text{Cu}(001)$ Shockley surface state moves in energy continuously with Mn coverage until the $c(2\times 2)\text{MnCu}$ is built. Since this coincides with the work function change when going from $\text{Cu}(001)$ to $c(2\times 2)\text{MnCu}/\text{Cu}(001)$, this shift is not only trapped by the image state (as already detected by inverse photoemission [Hay95, Rad97a]), but also by the Shockley state. A similar treatment of image ($n=1$) as well as the Shockley ($n=0$) states as a part of the image potential Rydberg series was proposed already in an earlier work of SMITH [Smi85].

Using the changed symmetry of the $c(2\times 2)$ surface Brillouin zone a new method for the detection of the Mn-derived $3d$ spin majority band was presented. Usually the intense substrate copper-derived bands mask the new Mn bands. However, when measuring at the $\bar{\Gamma}_{c(2\times 2)}$ point of the second surface Brillouin zone, where copper bands reveal a gap, a shoulder at 3.0 eV binding energy was interpreted as a searched Mn-derived spin majority feature. For the 1 ML $pgg(4\times 2)\text{Mn}/\text{Cu}(001)$ system, which consists of two slightly distorted $c(2\times 2)\text{MnCu}$ compound layers, the same energy position for the spin majority band was found indicating that also in the second compound layer the Mn atoms are still in a high spin ground

state.

The procedure of a measurement at the $\bar{\Gamma}$ point of the second surface Brillouin zone was also applied to the $c(2\times 2)\text{Mn}/\text{X}(001)$ systems synthesised on the ferromagnetic fcc (001) surfaces of epitaxially grown $\text{X}/\text{Cu}(001)$ systems ($\text{X}=\text{Fe}, \text{Co}$, and Ni). For the first time the $\text{Mn}/\text{Fe}/\text{Cu}(001)$ system was investigated and a $c(2\times 2)$ LEED pattern as for $\text{Mn}/\text{Cu}(001)$ and $\text{Mn}/\text{Ni}(001)$ was obtained. By this similarity the observed $c(2\times 2)$ structure was interpreted due to formation of a MnFe surface compound. However, further investigations like, e.g., I-V-LEED or PED in backward scattering geometry have to be performed to confirm this result. The Mn-derived $3d$ spin majority band was found at approx. 3.5 eV binding energy for all $c(2\times 2)\text{Mn}/\text{X}/\text{Cu}(001)$ systems ($\text{X}=\text{Fe}, \text{Co}, \text{Ni}$) that is slightly larger than its binding energy in $c(2\times 2)\text{MnCu}$. Similar to $c(2\times 2)\text{MnCu}/\text{Cu}(001)$ this value is interpreted as the local free spin majority band position. The main reason for the energy separation of the Mn spin majority and minority bands is the enhanced Mn-Mn distance as compared to that in bulk Mn resulting in a weaker d band overlap. This was verified in the present study by using a $\text{Ni}(001)$ substrate that has a slightly smaller lattice constant. The corresponding position of the Mn spin majority band in $c(2\times 2)\text{MnNi}/\text{Ni}(001)$ ($E_B=3.0$ eV) is found to be lower than that in $c(2\times 2)\text{MnNi}/\text{Ni}/\text{Cu}(001)$.

Only in the case of $\text{Ni}/\text{Cu}(001)$ deviations from the substrate Fermi surface have been found in the $\text{Mn}/\text{X}/\text{Cu}(001)$ systems. In the other cases ($\text{X}=\text{Fe}, \text{Co}$) no new bands cross the Fermi edge or occur in proximity of the Fermi level. The changes in $c(2\times 2)\text{MnNi}/\text{Ni}/\text{Cu}(001)$ was assigned to the $\text{Ni}(001)$ magnetic surface states affected by Mn adsorption. The main problem encountered during the analysis of the systems was the lack of available photoemission data for the ferromagnetic $\text{X}/\text{Cu}(001)$ systems.

Using photoelectron diffraction it was shown that copper grows in a layer-by-layer mode on top of the $c(2\times 2)\text{MnCu}/\text{Cu}(001)$ surface. Thereby the Mn atoms maintain their high spin ground state as it was disclosed by the soft X-ray absorption and photoemission experiment. A second layer of the $c(2\times 2)\text{MnCu}$ surface compound with the Mn atoms again in a high spin ground state could be grown on top of the discussed above sandwich structure. This launches the possibility to investigate the magnetic coupling between the layers and phenomena like giant magnetoresistance or quantum well spin states might be found in the $c(2\times 2)\text{MnCu}/\text{Cu}$ multilayer system. The electronic structures of the three- ($\text{Cu}/\text{MnCu}/\text{Cu}$) and four- ($\text{MnCu}/\text{Cu}/\text{MnCu}/\text{Cu}$) layer stacks were found to be nearly identical.

Preliminary experiments show the existence of a $c(2\times 2)\text{Mn}/\text{Au}(001)$ phase [Sch01] and also on $\text{Ag}(001)$ a $c(2\times 2)$ LEED pattern was observed [Sch96]. This suggests that the $c(2\times 2)$ -derived Mn structures represent a new class of magnetic surface compounds. Fcc (001) surfaces of other elements or compounds should be probed in order to fully characterise properties of this $c(2\times 2)$ surface compound group.

Appendix A

The Mn/Cu(001) overlayer system

A.1 Manganese

Manganese is (together with Cr) the element among the $3d$ elements, that has the highest atomic moment due to its electronic configuration, that is shown in Fig. A.1 [Ash76] in a part of the periodic table containing the other elements considered during this work. Together with Cr, Mn contains $5d$ electrons that

Vanadium	Chromium	Manganese	Iron	Cobalt	Nickel	Copper
23	24	25	26	27	28	29
V	Cr	Mn	Fe	Co	Ni	Cu
[Ar] 3d ³ 4s ²	[Ar] 3d ⁵ 4s ¹	[Ar] 3d ⁵ 4s ²	[Ar] 3d ⁶ 4s ²	[Ar] 3d ⁷ 4s ²	[Ar] 3d ⁸ 4s ²	[Ar] 3d ¹⁰ 4s ¹
3.02 BCC	2.88 BCC	8.89 CUB	2.87 BCC	2.51 HEX 1.622	3.62 FCC	3.61 FCC

Labels in the diagram:
 - Symbol of the element: points to Mn
 - Atomic number: points to 25
 - Lattice structure: points to CUB
 - Lattice constant in Å: points to 8.89
 - Electronic configuration: points to [Ar] 3d⁵ 4s²
 - at room temperature: points to the lattice structure and constant labels

Figure A.1: Part of the periodic table: the $3d$ elements near Mn.

order parallel to each other according to Hund's rule as there exist 5 electronic levels that can be occupied each by two electrons of opposite spin amounting to a *atomic* magnetic moment of $5\mu_B$. However, bulk manganese (as well as Cr) is non-ferromagnetic due to antiferromagnetic overlapping of the neighbouring $3d$ levels. While the other elements between Ti and Cu reveal simple bcc, fcc, or hcp lattices, manganese crystallises into a complicated cubic structure with a basis of 58 atoms per unit cell at room temperature. At higher temperature several phase transitions take place including also the fcc and bcc phases (see Fig. A.2 [Pea67]). From the fact that there are already more than one stable bulk phase it can be expected that there will also exist different structures at the surface.

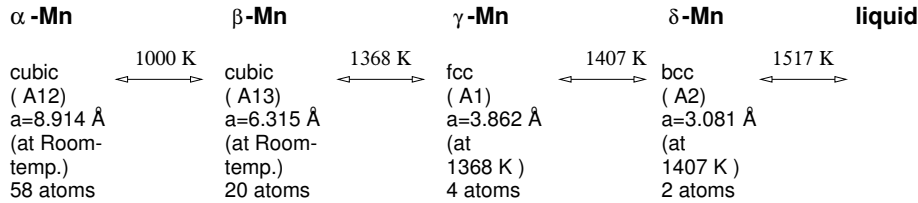


Figure A.2: The variety of the structures of manganese [Pea67].

A.2 The Mn/Cu system

A.2.1 Historical remarks about the Mn/Cu compounds

In 1933 VALENTINER and BECKER investigated copper-manganese alloys containing 10-40 at.% Mn. Interesting magnetic properties were found [Val33]. Pioneering work in surface investigation was carried out in the early 80th by EASTMAN and GROBMAN [Eas73], and the first results related to the absorption of metals on orientated single crystal surfaces were published in 1976 by RHEAD [Rea76] and in 1979 by BIBERIAN and SOMORJAI [Bib79]. BINNS and NORRIS [Bin82] were the first who measured the Mn/Cu(001) surface system.

A.2.2 Investigations in the Mn/Cu surface structure

The Mn/Cu(001) surface structure was studied by the following groups. BINNS and NORRIS [Bin82] used Auger Electron Spectroscopy (AES), Low energy electron diffraction (LEED) and angle-integrated Ultraviolet Photoelectron Spectroscopy (UPS) in 1982; EGELHOFF *et al.* [Ege90] investigated the growth of Mn at Cu(001) at 80K with X-ray Photoelectron and Auger Electron Forward Scattering in 1990; a LEED, Middle Energy Electron Diffraction (MEED) and AES study was published by FLORES *et al.* [Flo92] in 1992; and a dynamical LEED study was done by WUTTIG *et al.* [Wut93c]. *Ab initio* total energy calculations published by WUTTIG *et al.* [Wut93b] concentrated already only on the c(2×2)CuMn/Cu(001) surface alloy. Scanning Tunneling microscopy (STM) experiments were carried out in 1994 by NOH *et al.* [Noh94], in 1995 by VAN DER KRAAN and VAN KEMPEN [vdK95], in 1996 in a reply to the results of NOH *et al.* by WUTTIG *et al.* [Wut96] and by FLORES *et al.* [Flo97]. O'BRIEN and coworker [O'B93] used magnetic circular dichroism and soft X-ray absorption to investigate the c(2×2)CuMn/Cu(001) system. Details of the structure were analysed by TOOMES *et al.* with Photoelectron diffraction. Photoemission experiments were performed in 1995 by HAYDEN *et al.* [Hay95] (Inverse PE) and in 1997 by RADER *et al.* [Rad97a] (PE and inverse PE). Recent theoretical investigations were carried out by EDER *et al.* [Ede99, Ede00] and WORTMANN *et al.* [Wor00].

A.2.3 Experimental results from literature

BINNS and NORRIS who measured first the Mn/Cu(001) structure at room temperature in 1982 found a disordered layer-by-layer (Frank-van der Merve) growth. They measured the intensity of the Cu-62eV and the Mn-40eV Auger lines in AES. LEED analysis at low coverages already indicated a $c(2 \times 2)$ superstructure. Assuming that Mn and Cu do not change their radii significantly they proposed two possibilities for the structure, a $c(2 \times 2)$ superstructure and a $c(2 \times 2)$ surface alloy in which the Mn atoms have replaced the Cu atoms at the face centres of the face centred square arrangement. This structure was favoured because Cu and Mn show a slight tendency to form an ordered Cu_3Mn alloy [Han88].

The LEED measurements at room temperature indicate a $c(2 \times 2)$ superstructure till 0.5 ML Mn (see Figure 1.9). At higher coverage additional peaks of a $p2mg(4 \times 2)$ superstructure appear. These $p2mg(4 \times 2)$ reflexes increase up to a coverage of 3-4 ML Mn. Later on KRAAN and KEMPEN could show that this structure is a $pgg(4 \times 2)$ and not the one claimed before. At 200K other superstructures have been found such as $c(8 \times 2)$ and $c(12 \times 2)$ (see [Flo92] for details). EGELHOFF *et al.* [Ege90], however, did not see any alteration of the LEED pattern evaporating onto a Cu(001) substrate cooled to 80K. Fig. A.3 summarises the LEED results from [Flo92], [vdK95], and [Ege90].

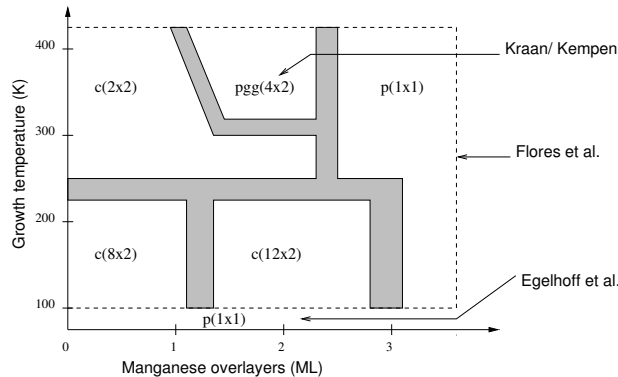


Figure A.3: Mn structures on Cu(001) as investigated by FLORES *et al.* [Flo92] above 100K with a correction by KRAAN and KEMPEN [vdK95] and EGELHOFF *et al.* [Ege90].

A.3 The $c(2 \times 2)$ CuMn/Cu(001) surface alloy

The $c(2 \times 2)$ superlattice is the most interesting surface structure in the Mn/Cu system, because it was not clear whether the $c(2 \times 2)$ LEED pattern reflects a superstructure or an alloy, nor if there exist out- or inward displacements. Additionally there were other questions concerning the magnetic properties. LEED I-V-data taken for the $c(2 \times 2)$ structure showed that Mn is incorporated in the surface forming an ordered surface alloy [Wut93c]. Not only the structure could

be clarified by I-V-analysis, but also a corrugation could be concluded. The analysis is based on structural models which are compared to the experimental data by a trial-and-error procedure calculating the mean quadratical deviation as the Pendry-R-factor [Pen80]. The result for the corrugation calculated by WUTTIG *et al* [Wut93c] is $R=0.30\pm 0.02$ (see Fig. A.4 and table A.1).

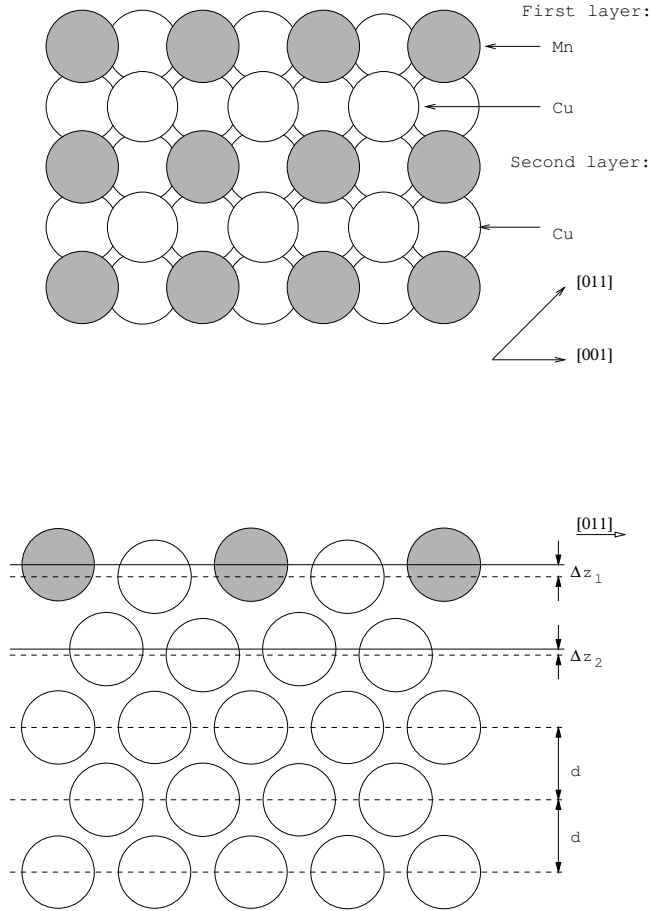


Figure A.4: The model of the $c(2\times 2)\text{Mn}/\text{Cu}(001)$ surface phase and a cut perpendicular to the (001)-surface in the $[110]$ -direction.

Structure	Δz_1 in \AA	Δz_2 in \AA
$c(2\times 2)\text{Au}/\text{Cu}(001)$	0.1(0.18)	-
$c(2\times 2)\text{Pd}/\text{Cu}(001)$	0.02 ± 0.03	-
$c(2\times 2)\text{Mn}/\text{Cu}(001)$	0.30 ± 0.02	0.02 ± 0.03
$c(2\times 2)\text{Mn}/\text{Ni}(100)$	0.25 ± 0.02	0.00 ± 0.03

Table A.1: Summary of the structural results obtained for different ordered surface alloys: Au [Wan87] [Foi87], Pd [Wu88], and Mn[Wut93c].

This analysis predict that the Mn surface-atoms are outwards displaced. A summary of the calculated data compared with other structures gives Table A.1.

WU *et al.* [Wu88] argued that the corrugation of the surface alloy layer increases with increasing size of the deposited element. This statement is consistent with the smaller corrugation of the CuPd surface alloy as compared with the CuAu surface alloy. If this tendency would also hold for Mn, one would expect an even smaller corrugation than the one observed for the CuPd surface alloy since the atomic radius of elemental Mn is smaller than that of Pd. On the contrary, the corrugation found for the Mn surface alloy on Cu(001) and Ni(001) is considerably larger than the corrugation of the CuAu surface alloy (see Table A.1). This shows that simple size arguments are insufficient to explain the corrugation of surface alloys. Further evidence for this statement comes from a comparison of the corrugation for Mn on Cu(001) and Ni(001). One would expect that the corrugation should be slightly larger on the Ni(001) surface, since the misfit between Mn and Ni is larger than between Mn and Cu. On the contrary, a larger corrugation is found for the $c(2\times 2)$ surface alloy of Mn on Cu(001).

BLÜGEL *et al.* have carried out a structural optimisation of a paramagnetic and a ferromagnetic Cu(001)- $c(2\times 2)$ -Mn surface alloy [Wut93b]. In these calculations, which are based on the density functional theory in the local spin density approximation, only a marginal corrugation of less than 0.02 \AA is found for the paramagnetic surface alloy. This compares well with the results and tendencies found for the CuPd and CuAu surface alloy but is at variance with the experimental observation of a pronounced corrugation for the CuMn surface alloy. For the ferromagnetic surface alloy, however, a corrugation of 0.24 \AA is found in the calculation, which is in much better agreement with the experiments. The calculation also shows that the ferromagnetic surface alloy has a considerably smaller energy than the nonmagnetic surface alloy. From these theoretical results BLÜGEL *et al.* conclude, that the pronounced corrugation of the CuMn surface alloy is due to the large magnetic moment at the surface¹. Photoelectron diffraction investigations in the backscattering regime resulted in a corrugation of $(0.39 \pm 0.08 \text{ \AA})$ [Too96], so the result found by WUTTIG *et al.* was confirmed and it was shown that the proposed weaker corrugation concluded from STM data was an artefact of the experiment [Noh94].

The large gain in magnetic energy also stabilises the system against interdiffusion. Hence, both the stability and corrugation are caused by the pronounced magnetic moment of the Mn atoms and the resulting gain in magnetic energy. Soft X-ray absorption measurement confirm this view by detecting Mn being in a high spin-state [O'B93]. The contribution of the long-range magnetic order, i.e. ferro- or antiferromagnetic coupling of the magnetic moments is a factor of 20 smaller

¹In the paramagnetic case, the d bands are half filled. Contrarily in the magnetic case the spin majority d orbitals are nearly completely occupied and the spin minority d bands are nearly empty. As a consequence, there are nearly as many Mn d bonding states occupied as d antibonding states and as a result, the d cohesion becomes less important and is energetically compensated by the gain of magnetic energy. Due to the reduced cohesive energy the atomic radii of the Mn atoms increase leading to the outward corrugation [Wut93b].

than the energy caused by the local moments. This gives further support for the picture presented above, that the large size of the local magnetic moments is the origin of the large outwards relaxation of the Mn atoms and the stability of the surface alloy phase.

If as proposed by WUTTIG *et al.* [Wut93b] and measured by O'BRIEN *et al.* [O'B93] the Mn atoms are in a high spin state, the surface shows different electronic properties than a simple CuMn-alloy. HAYDEN *et al.* [Hay95] found the unoccupied 3d Mn band above the Fermi level using Inverse Photoemission, whereas RADER *et al.* investigated the occupied and unoccupied valence bands by angle resolved photoemission and inverse photoemission. A 5.5 eV large spin-splitting was found [Rad97a]. New valence band spectral features have been found, that could be attributed to correlation satellites driven by the reduced dimensionality [Rad97b].

While former theoretical investigations [Rad97a, Fab95] reported the band splitting much smaller than in the experiment, recent calculations found this magnetic splitting amounting to approx. 4.4 eV [Ede00]. The still existing difference to the experiment was attributed to effects introduced by the final-state screening occurring in photoemission that is not considered in the theory. Another theoretical investigation [Wor00] explained LEED data in [vdK95] as due to the occurrence of a Mn-derived spin minority band close to the \bar{X} point of the surface Brillouin zone.

Bibliography

- [Aeb94] P. AEBI; J. OSTERWALDER; R. FASEL; D. NAUMOVIĆ and L. SCHLAPPBACH: *Fermi surface mapping with photoelectrons at UV energies*. Surf. Sci. **307-309** (1994) p. 917.
- [And75] O. K. ANDERSEN: *Linear methods in band theory*. Phys. Rev. B **12** (1975) p. 3060.
- [Ash76] N. W. ASHCROFT and N. D. MERMIN: *Solid State Physics* (Holt, Rinehart and Winston, 1976).
- [Avi95] J. AVILA; C. CASADO; M. C. ASENSIO; J. L. PEREZ; M. C. MUÑOZ and F. SORIA: *Bulk Fermi surface determination by tuning the photoelectron kinetic energy*. J. Vac. Sci. Technol. A **13** (1995) p. 1501.
- [Bal] P. BALTZERS: Personal communication.
- [Bib79] J. P. BIBERIAN and G. A. SOMORJAI: *Surface structures of metallic monolayers on metal crystal surfaces*. J. Vac. Sci. & Tech. **16** (1979) p. 2073.
- [Bin82] C. BINNS and C. NORRIS: *Manganese overlayers on copper (100); a study by LEED, AES and UPS*. Surf. Sci. **116** (1982) p. 338.
- [Car93] C. CARBONE; E. VESCOVO; O. RADER; W. GUDAT and W. EBERHARDT: *Exchange split quantum well states of a noble metal film on a magnetic substrate*. Phys. Rev. Lett. **71** (1993) p. 2805.
- [Cas96] C. CASADO: *Determinación experimental de la estructura electrónica y la superficie de Fermi de multicapas magnéticas*. Ph.D. thesis, Universidad Complutense de Madrid (1996).
- [Cer95] J. I. CERDÁ: *Caracterización Estructural de Superficies Mediante Difracción de Electrones de Baja Energía (LEED)*. Ph.D. thesis, Universidad Autónoma de Madrid (1995).
- [Cha91] S. CHAMBERS: *Epitaxial film crystallography by high-energy Auger and X-ray photoelectron diffraction*. Adv. in Phys. **40** (1991) p. 357.

- [Cho98] B.-C. CHOI; P. J. BODE and J. A. C. BLAND: *Formation of a two-dimensional $c(2\times 2)$ Mn-Co(001) ferromagnetic surface alloy on Cu(001)*. Phys. Rev. B **58** (1998) p. 5166.
- [Cho99] B.-C. CHOI; P. J. BODE and J. A. C. BLAND: *Magnetic anisotropy strength and surface alloy formation in Mn/Co/Cu(001) overlayers*. Phys. Rev. B **59** (1999) p. 7029.
- [Cla87] A. CLARKE; P. J. ROUS; M. ARNOTT; G. JENNINGS and R. F. WILLIS: *Thickness dependent relaxation in γ fcc Fe films on Cu(001): A LEED structural study*. Surf. Sci. **192** (1987) p. L843.
- [Cou84] R. COURTHS and S. HÜFNER: *Photoemission experiments on copper*. Phys. Rep. **112** (1984) p. 53.
- [Cra55] J. CRANGLE: *The Magnetic Moments of Cobalt-Copper Alloys*. Philos. Mag. **46** (1955) p. 499.
- [Den79] W. A. DENCH and M. P. SEAH: *Quantitative Electron Spectroscopy of Surfaces: A Standard Data Base for Electron Inelastic Mean Free Path in Solids*. Surf. Interf. Anal. **1** (1979) p. 1.
- [Dos86] V. DOSE; T. FAUSTER and R. SCHNEIDER: *Improved resolution in VUV isochromat spectroscopy*. Appl. Phys. A **40** (1986) p. 203.
- [Dur81] P. DURHAM and N. KAR: *Special features in photoemission from the s-p bands of copper*. Surf. Sci. **111** (1981) p. L648.
- [Eas73] D. A. EASTMAN and W. D. GROBMAN: *Photoemission Observed of Resonant d Levels and d-Band Formation for Very Thin Overlayers of Cu and Pd on Ag*. Phys. Rev. Lett. **30** (1973) p. 177.
- [Ebe80] W. EBERHARDT and F. J. HIMPSEL: *Dipole selection rules for optical transition in fcc and bcc lattices*. Phys. Rev. B **21** (1980) p. 5572.
- [Ede99] M. EDER; J. HAFNER and E. G. MORONI: *Structure and magnetic properties of thin Mn/Cu(001) and CuMn/Cu(100) films*. Surf. Sci. **423** (1999) p. L244.
- [Ede00] M. EDER; J. HAFNER and E. G. MORONI: *Structural, electronic, and magnetic properties of thin Mn/Cu(100) films*. Phys. Rev. B **61** (2000) p. 11492.
- [Ege90] W. F. EGELHOFF JR.; I. JACOB; J. M. RUDD; J. F. COCHRAN and B. HEINRICH: *X-ray photoelectron and Auger electron forward-scattering studies of lattice expansions and contractions in epitaxial films*. J. Vac. Sci. Technol. A **8** (1990) p. 1582.

- [Ein05] A. EINSTEIN: *Über einen die Erzeugung und Verwandlung des Lichtes betreffenden heuristischen Gesichtspunkt*. Ann. Physik **17** (1905) p. 132.
- [Fab95] G. FABRICIUS; A. M. LLOIS; M. WEISSMANN; M. A. KHAN and H. DREYSSÉ: *Electronic and magnetic properties of Mn/Cu/Mn and Mn/Ni/Mn slabs*. Surf. Sci. **331-333** (1995) p. 1377.
- [Fad90] C. FADLEY: *Synchrotron Radiation Research: Advances in Surface Science*, chap. The study of surface structures by photoelectron diffraction and Auger electron diffraction (Plenum press, New York, 1990).
- [Far97] M. FARLE; W. PLATOW; A. N. ANISIMOV; P. POULOPOULOS and K. BABERSCHKE: *Anomalous reorientation phase transition of the magnetization in fct Ni/Cu(001)*. Phys. Rev. B **56** (1997) p. 5100.
- [Flo92] T. FLORES; M. HANSEN and M. WUTTIG: *Structure and Growth of Mn on Cu(100)*. Surf. Sci. **279** (1992) p. 251.
- [Flo97] T. FLORES; S. JUNGHANS and M. WUTTIG: *Atomic mechanism for the diffusion of Mn atoms incorporated in the Cu(100) surface: an STM study*. Surf. Sci. **371** (1997) p. 1.
- [Foi87] S. M. FOILES: *Ordered surface phases of Au on Cu*. Surf. Sci. **191** (1987) p. 329.
- [Gar98] M. GARNIER; D. PURDIE; K. BREUER; M. HENGESBERGER; and Y. BAER: *High-resolution photoemission from an ordered Ce/Be alloy*. Phys. Rev. B **58** (1998) p. 3515.
- [Gre97] T. GREBER; T. J. KREUTZ and J. OSTERWALDER: *Photoemission above the Fermi Level: The Top of the Minority d Bands in Nickel*. Phys. Rev. Lett. **79** (1997) p. 4465.
- [Hal] S. V. HALILOV: Personal communication.
- [Hal93] S. V. HALILOV; E. TAMURA; H. GOLLISCH; D. MEINERT and R. FEDER: *Relativistic Green function theory of layer densities of states and photoemission from magnetic compounds*. J. Phys.: Condens. Matter **5** (1993) p. 3859.
- [Hal95] S. V. HALILOV; J. HENK; T. SCHEUNEMANN and R. FEDER: *Surface states and photoemission of magnetic multilayer systems*. Phys. Rev. B **52** (1995) p. 14235.
- [Han88] M. HANSEN and K. ANDERKO: *Constitution of Binary Alloys*. 2 edn. (Mc Graw-Hill New York, 1988).

- [Hay95] A. B. HAYDEN; P. PERVAN and D. P. WOODRUFF: *Inverse photoemission study of the Cu(100)c(2×2)-Mn phase*. J. Phys.: Condens. Matter **7** (1995) p. 1139.
- [Hea77] S. M. HEALD and E. A. STERN: *Anisotropic x-ray absorption in layered compounds*. Phys. Rev. B **16** (1977) p. 5549.
- [Hei79] P. HEINMANN; J. HERMANSON and H. M. H. NEDDERMEYER: *d-like surface-state bands on Cu(100) and Cu(111) observed in angle-resolved photoemission spectroscopy*. Phys. Rev. B **20** (1979) p. 3059.
- [Her87] H. HERTZ: *Ueber einen Einfluss des ultravioletten Lichtes auf die elektrische Entladung*. Ann. Physik **31** (1887) p. 983.
- [Her77] J. HERMANSON: *Final-state symmetry and polarization effects in angle-resolved photoemission spectroscopy*. Solid State Commun. **22** (1977) p. 9.
- [Him78] F. J. HIMPSEL and W. STEINMANN: *Angle-resolved photoemission from the NaCl (100) face*. Phys. Rev. B **17** (1978) p. 2537.
- [Hoc99] M. HOCHSTRASSER; N. GILMAN; R. F. WILLIS; F. O. SCHUMANN; J. G. TOBIN and E. ROTENBERG: *Photoemission study of Fermi surfaces of pseudomorphic Co, Ni, and Co_xNi_{1-x} films on Cu(100)*. Phys. Rev. B **60** (1999) p. 17030.
- [Hua94] F. HUANG; M. T. KIEF; G. J. MANKEY and R. F. WILLIS: *Magnetism in the few-monolayers limit: A surface magneto-optic Kerr-effect study of the magnetic behavior of ultrathin films of Co, Ni, and Co-Ni alloys on Cu(100) and Cu(111)*. Phys. Rev. B **49** (1994) p. 3962 and references therein.
- [Hüf96] S. HÜFNER: *Photoelectron Spectroscopy*, vol. 82 of *Springer Series in Solid-State Sciences*. 2 edn. (Springer-Verlag Berlin Heidelberg New York, 1996).
- [Hul21] A. W. HULL: *X-Ray Crystal Analysis of Thirteen Common Metals*. Phys. Rev. **17** (1921) p. 571.
- [Hut01] Y. HUTTEL; S. GALLEGRO; M. C. MUÑOZ and M. C. ASENSIO: *New electronic states close to the Fermi edge in the c(2×2)MnCu(100) surface alloy*. Surf. Sci. **482-485** (2001) p. 540.
- [Iwa79] M. IWAN; F. J. HIMPSEL and D. E. EASTMAN: *Two-Electron Resonance at the 3p Threshold of Cu and Ni*. Phys. Rev. Lett. **43** (1979) p. 1829.

- [Jay96] J. P. JAY: *On the stability of bcc Co in Co/Fe superlattices an NMR and XRD study.* Zeitschrift f. Physik. b, condensed matter **101** (1996) p. 329.
- [Jes68] W. A. JESSER and J. W. MATTHEWS: *Pseudomorphic Deposits of Cobalt on copper.* Philos. Mag. **17** (1968) p. 471 and references therein.
- [Joh80] B. JOHANSSON and N. MÅRTENSSON: *Core-level binding-energy shifts for metallic elements.* Phys. Rev. B **21** (1980) p. 4427.
- [Kev83] S. D. KEVAN: *Observation of a new surface state on Cu(001).* Phys. Rev. B **28** (1983) p. 2268.
- [Kev85] S. D. KEVAN; N. G. STOFFEL and N. V. SMITH: *Surface states on low-Miller-index copper surfaces.* Phys. Rev. B **31** (1985) p. 3348.
- [Kie93] M. T. KIEF and W. F. EGELHOFF JR.: *Growth and Structure of Fe and Co thin films on Cu(111), Cu(100), and Cu(110): A comprehensive study of metastable film growth.* Phys. Rev. B **47** (1993) p. 10785.
- [Kim97] S. H. KIM; K. S. LEE; H. G. MIN; J. SEO; S. C. HONG; T. H. RHO and J. S. KIM: *Subsurface growth of Ni atoms deposited on a Cu(001) surface.* Phys. Rev. B **55** (1997) p. 7904.
- [Kit85] C. KITTEL: *Introduction to Solid State Physics.* 10 edn. (John Wiley and sons New York, 1985).
- [Koe99] K. KOEPERNIK and H. ESCHRIG: *Full-potential nonorthogonal local-orbital minimum-basis band-structure scheme.* Phys. Rev. B **59** (1999) p. 1743.
- [Kou63] J. S. KOUVEL and J. S. KASPER: *Long-range antiferromagnetism in disordered Fe-Ni-Mn alloys.* J. Phys. Chem. Solids **24** (1963) p. 529.
- [Kut92] W. KUTZELNIGG: *Einführung in die theoretische Chemie*, vol. 1. 2 edn. (VCH Weinheim, 1992).
- [Leh97] C. LEHMANN; S. SINNING; P. ZAHN; H. WONN and I. MERTIG: *Fermi surfaces.* <http://www.physik.tu-dresden.de/~fermisur/> (1997).
- [Lin80] S. A. LINDGREN and L. WALLDÉN: *Photoemission of electrons at the Cu(111)/Na interface.* Solid State Commun. **34** (1980) p. 671.
- [Lin96] M. LINDROOS and A. BANSIL: *A Novel Direct Method of Fermi Surface Determination Using Constant Initial Energy Angle-Scanned Photoemission Spectroscopy.* Phys. Rev. Lett. **77** (1996) p. 2985.

- [Lin01] M. LINDROOS; J. AVILA; M. E. DÁVILA; Y. HUTTEL; M. C. ASENSIO and A. BANSIL: *Angle-scanned photoemission spectrum from Cu(100): theory vs experiment*. Surf. Sci. **482-485** (2001) p. 718.
- [Loe96] S. LOEBUS; R. COURTHS; S. V. HALILOV; H. GOLLISCH and R. FEDER: *Bulk and surface electronic states of ordered Cu₃Au(001): an angle-resolved photoemission investigation*. Surface Review and Letters **3** (1996) p. 1749.
- [Man97] G. J. MANKEY; K. SUBRAMANIAN; R. L. STOCKBAUER and R. L. KURTZ: *Observation of a Bulklike Fermi Surface for a Monolayer of Ni on Cu(001)*. Phys. Rev. Lett. **78** (1997) p. 1146.
- [Mas92] T. B. MASSALSKI, (ed.): *Binary alloy phase diagrams*. 2 edn. (ASM international, 1992).
- [Mie75] A. R. MIEDEMA; R. BOOM and F. R. DE BOER: *On the formation of solid alloys*. J. Less Common Met. **41** (1975) p. 283.
- [Mie76] A. R. MIEDEMA: *On the formation of solid alloys. II*. J. Less Common Met. **46** (1976) p. 67.
- [Mol00] S. L. MOLODTSOV; S. V. HALILOV; V. D. P. SERVEDIO; W. SCHNEIDER; S. DANZENBÄCHER; J. J. HINAREJOS; M. RICHTER and C. LAUBSCHAT: *Cooper Minima in the Photoemission Spectra of Solids*. Phys. Rev. Lett. **85** (2000) p. 4184.
- [Mor86] V. L. MORUZZI; P. M. MARCUS; K. SCHWARZ and P. MOHN: *Ferromagnetic phases of bcc and fcc Fe, Co, and Ni*. Phys. Rev. B **34** (1986) p. 1784.
- [Mor88] V. L. MORUZZI; P. M. MARCUS and P. C. PATTNAIK: *Magnetic transition in bcc vanadium, chromium, manganese, and iron*. Phys. Rev. B **37** (1988) p. 8003.
- [Mor89] V. L. MORUZZI; P. M. MARCUS and J. KÜBLER: *Magnetovolume instabilities and ferromagnetism versus antiferromagnetism in bulk fcc iron and manganese*. Phys. Rev. B **39** (1989) p. 6957.
- [Mor99] E. G. MORONI; G. KRESSE and J. HAFNER: *Coherent epitaxy and magnetism of face-centred-cubic Fe films on Cu(100)*. J. Phys.: Condens. Matter **11** (1999) p. L35.
- [Mül95] S. MÜLLER; P. BAYER; C. REISCHL; K. HEINZ; B. FELDMANN; H. ZILLGEN and M. WUTTIG: *Structural Instability of Ferromagnetic fcc Fe Films on Cu(100)*. Phys. Rev. Lett. **74** (1995) p. 765 and references therein.

- [Nog96] A. NOGUERA; S. BOUARAB and H. DREYSSE: *Very thin Mn films on fcc Co(001)*. J. Magn. Mater **156** (1996) p. 21.
- [Noh94] H. P. NOH; T. HASHIZUME; D. JEON; Y. KUK and T. S. H. P. PICKERING: *Structure of the Mn-induced Cu(100)c(2×2) surface*. Phys. Rev. B **50** (1994) p. 2735.
- [Nou99] F. NOUVERTNÉ; U. MAY; M. BAMMING; A. RAMPE; U. KORTE; G. GÜNTHERODT; R. PENTCHEVA and M. SCHEFFLER: *Atomic exchange processes and bimodal initial growth of Co/Cu(001)*. Phys. Rev. B **60** (1999) p. 14382.
- [O'B93] W. L. O'BRIEN; J. ZHANG and B. P. TONNER: *Local magnetic properties and magnetic ordering of the two-dimensional surface alloy c(2×2)Mn/Cu(001)*. J. Phys.: Condens. Matter **5** (1993) p. L515.
- [O'B94a] W. L. O'BRIEN and B. P. TONNER: *Enhanced magnetic moment and magnetic ordering in MnNi and MnCu surface alloys*. J. Appl. Phys. **76** (1994) p. 6468.
- [O'B94b] W. L. O'BRIEN and B. P. TONNER: *Surface-enhanced magnetic moment and ferromagnetic ordering of Mn ultrathin films on fcc Co(001)*. Phys. Rev. B **50** (1994) p. 2963.
- [O'B95] W. L. O'BRIEN and B. P. TONNER: *Magnetic properties of Mn/Cu(001) and Mn/Ni(001)c(2×2) surface alloy*. Phys. Rev. B **51** (1995) p. 617.
- [Ort92] J. E. ORTEGA and F. J. HIMPSEL: *Quantum well states as mediators of magnetic coupling in superlattices*. Phys. Rev. Lett. **69** (1992) p. 844.
- [Ort93] J. E. ORTEGA; F. J. HIMPSEL; G. J. MANKEY and R. F. WILLIS: *Quantum-well states and magnetic coupling between ferromagnets through a noble-metal layer*. Phys. Rev. B **47** (1993) p. 1540.
- [Owe56] J. OWEN; M. BROWNE; W. D. KNIGHT and C. KITTEL: *Electron and Nuclear Spin Resonance and Magnetic Susceptibility Experiments on Dilute Alloys of Mn in Cu*. Phys. Rev. **102** (1956) p. 1501.
- [Pam01] C. PAMPUCH; O. RADER; R. KLÄSGES and C. CARBONE: *Evolution of the electronic structure in epitaxial Co, Ni, and Cu films*. Phys. Rev. B **63** (2001) p. 153409.
- [Pap85] D. A. PAPACONSTANTOPOULOS: *Handbook of Band structure of Elemental Solids* (Plenum Press New York, 1985).
- [Pea67] W. P. PEARSON: *A Handbook of Lattice Spacing and Structures of Metals and Alloys* (Pergamon Press, 1967).

- [Pen80] J. B. PENDRY: *Reliability factors for LEED calculations*. J. Physics C **13** (1980) p. 937.
- [Pla90] W. PLATOW; U. BOVENSIEPEN; P. POULOPOULOS; M. FARLE; K. BABERSCHKE; L. HAMMER; S. WALTER; S. MÜLLER and K. HEINZ: *Structure of ultrathin Ni/Cu(001) films as a function of film thickness, temperature, and magnetic order*. Phys. Rev. B **59** (1990) p. 12641 and references therein.
- [Plu79] E. W. PLUMMER and W. EBERHARDT: *Magnetic surface states on Ni(001)*. Phys. Rev. B **20** (1979) p. 1444.
- [Plu82] E. W. PLUMMER and W. EBERHARDT: *Angle-resolved photoemission as a tool for the study of surfaces*. Adv. Chem. Phys. **49** (1982) p. 533.
- [Pri85] G. A. PRINZ: *Stabilization of bcc Co via Epitaxial Growth on GaAs*. Phys. Rev. Lett. **54** (1985) p. 1051.
- [Rad97a] O. RADER; W. GUDAT; C. CARBONE; E. VESCOVO; S. BLÜGEL; R. KLÄSGES; W. EBERHARDT; M. WUTTIG; J. REDINGER and F. J. HIMPSEL: *Electronic structure of two-dimensional magnetic alloys: $c(2\times 2)$ Mn on Cu(100) and Ni(100)*. Phys. Rev. B **55** (1997) p. 5404.
- [Rad97b] O. RADER; E. VESCOVO; M. WUTTIG; D. D. SARMA; S. BLÜGEL; F. J. HIMPSEL; A. KIMURA; K. S. AN; T. MIZOKAWA; A. FUJIMORI and C. CARBONE: *Correlation satellite driven by reduced dimensionality*. Europhys. Lett. **39** (1997) p. 429.
- [Rea76] G. E. READ: *Probing surface properties with adsorbed metal monolayers*. J. Vac. Sci. & Tech. **13** (1976) p. 603.
- [Ric89] M. RICHTER and H. ESCHRIG: *Spin polarized relativistic LCAO formalism: fundamentals and first results*. Solid State Commun. **72** (1989) p. 263.
- [San91] A. SANTONI; L. J. TERMINELLO; F. J. HIMPSEL and T. TAKAHASHI: *Mapping the Fermi surface of graphite with a display-type photoelectron spectrometer*. Appl. Phys. A **52** (1991) p. 299.
- [Sch90] C. M. SCHNEIDER; P. BRESSLER; P. SCHUSTER; J. KIRSCHNER; J. J. DE MIGUEL and R. MIRANDA: *Curie temperature of ultrathin films of fcc-cobalt epitaxially grown on atomically flat Cu(100) surfaces*. Phys. Rev. Lett. **64** (1990) p. 1059.
- [Sch91] F. SCHEURER: *Evidence of epitaxial growth of bcc Co on Cr(100)*. Surf. Sci. **245** (1991) p. 175.

- [Sch96] P. SCHIEFFER; C. KREMBEL and G. GEWINNER: *Initial growth and structure of Mn on Ag(100): formation of a superficial alloy*. Solid State Commun. **97** (1996) p. 757.
- [Sch97] F. SCHILLER: *The growth of Vanadium and Manganese on Cu(001) studied by Auger- and Photoelectron diffraction*. Master's thesis, Technische Universität Dresden (1997).
- [Sch01] F. SCHILLER: *The electronic structure of the $c(2\times 2)$ Mn/Au(001) surface: band structure and Fermi surface investigations* (2001). Unpublished.
- [She95] J. SHEN; J. GIERGIEL and J. KIRSCHNER: *Growth and morphology of Ni/Cu(100) ultrathin films: An in situ study using scanning tunneling microscopy*. Phys. Rev. B **52** (1995) p. 8454.
- [Shi95] E. L. SHIRLEY; L. J. TERMINELLO; A. SANTONI and F. J. HIMPEL: *Brillouin-zone-selection effects in graphite photoelectron angular distributions*. Phys. Rev. B **51** (1995) p. 13614.
- [Sie82] H. SIEGBAHN and L. KARLSSON: *Encyclopedia of physics, vol. XXXI: Corpuscles and radiation in matter I*, chap. Photoelectron spectroscopy (Springer-Verlag, Berlin, Heidelberg, New York, 1982), p. 224.
- [Smi76] R. J. SMITH; J. ANDERSON and G. J. LAPEYRE: *Adsorbate Orientation Using Angle-Resolved Polarization-Dependent Photoemission*. Phys. Rev. Lett. **37** (1976) p. 1081.
- [Smi85] N. V. SMITH: *Phase analysis of image states and surface states associated with nearly-free-electron band gaps*. Phys. Rev. B **32** (1985) p. 3549.
- [Spi99] D. SPIŠÁK and HAFNER: *Electronic and magnetic structure of Mn-Ni alloys in two and three dimensions*. J. Phys.: Condens. Matter **11** (1999) p. 6359.
- [Spi00a] D. SPIŠÁK and HAFNER: *Magnetic structures in ordered and disordered γ -FeMn alloys: Ordering due to disorder*. Phys. Rev. B **61** (2000) p. 11569.
- [Spi00b] D. SPIŠÁK and HAFNER: *Strain-induced tetragonal distortion in epitaxial Ni-films grown on Cu(001)*. J. Phys.: Condens. Matter **12** (2000) p. L139.
- [Ste88] D. A. STEIGERWALD; I. JACOB and W. F. EGELHOFF JR.: *Structural Study of the Epitaxial Growth of fcc-Fe Films, Sandwiches, and superlattices on Cu(100)*. Surf. Sci. **202** (1988) p. 472.

- [Stö92] J. STÖHR: *NEXAFS Spectroscopy*, vol. 25 of *Springer Series in Surface Sciences* (Springer Verlag Berlin, 1992).
- [Tam88] E. TAMURA; S. BLÜGEL and R. FEDER: *On the determination of surface antiferromagnetism by low-energy electron diffraction*. *Solid State Commun.* **65** (1988) p. 1255.
- [Teo98] C. M. TEODORESCU; J. CHROST; H. ASCOLANI; J. AVILA; F. SORIA and M. C. ASENSIO: *Growth of Epitaxial Co Layers on Sb-Passivated GaAs(110) Substrates*. *Surface Review and Letters* **5** (1998) p. 279.
- [Thi81] P. THIRY: *La photoémission angulaire dans les solides*. Ph.D. thesis, Université Pierre et Marie Curie Paris (1981).
- [Tho95] U. THOMANN; G. RANGELOV and T. FAUSTER: *Angular distributions of VUV photoelectrons from Cu(001)*. *Surf. Sci.* **331-333 B** (1995) p. 1283.
- [Tis94] M. TISCHER; D. ARVANITIS; T. YOKOYAMA; T. LEDERER; L. TRÖGER and K. BABERSCHKE: *Temperature dependent MCXD measurements of thin Ni films on Cu(001)*. *Surf. Sci.* **307-309** (1994) p. 1096.
- [Tob92] J. G. TOBIN; G. D. WADDILL and D. P. PAPPAS: *Giant X-Ray Absorption Dichroism in Magnetic Ultrathin Films of Fe/Cu(001)*. *Phys. Rev. Lett.* **68** (1992) p. 3642.
- [Too96] R. TOOMES; A. THEOBALD; R. LINDSAY; T. GEISSEL; O. SCHAFF; R. DIDSZHUN; D. P. WOODRUFF; A. M. BRADSHAW and V. FRITZSCHE: *Photoelectron diffraction determination of the structure of the Cu(100)c(2×2)-Mn surface phase*. *J. Phys.: Condens. Matter* **8** (1996) p. 10231.
- [Val33] S. VALENTINER and G. BECKER: *Suszeptibilität und elektrische Leitfähigkeit von Kupfer-Mangan Legierungen*. *Z. Physik* **80** (1933) p. 735.
- [vdK95] R. G. P. VAN DER KRAAN and H. VAN KEMPEN: *Growth of Mn on Cu(100) studied by STM: the c(2×2) and pgg(4×2) ordered surface alloys*. *Surf. Sci.* **338** (1995) p. 19.
- [vdL92] G. VAN DER LAAN and I. W. KIRKMAN: *The 2p absorption spectra of 3d transition metal compounds in tetrahedral and octahedral symmetry*. *J. Phys.: Condens. Matter* **4** (1992) p. 4189.
- [vdM85] D. VAN DER MAREL; C. WESTRA and G. A. SAWATZKY: *Electronic structure of Mn impurities in noble metals*. *Phys. Rev. B* **31** (1985) p. 1936.

- [Wan87] Z. Q. WANG; Y. S. LI; C. K. C. LOK; J. QUINN and F. JONA: *Atomic and Electronic structure of a surface alloy- Comparison with bulk alloys*. Solid State Commun. **62** (1987) p. 181.
- [WE90] J. W.F. EGELHOFF: *X-Ray Photoelectron and Auger Electron Forward Scattering: A New Tool for Surface Crystallography*. Crit. Rev. in Sol. St. and Mat. Sci. **16** (1990) p. 213.
- [Win86] P. L. WINCOTT; N. B. BROOKES; D. S. L. LAW and G. THORNTON: *Relativistic effects on the surface electronic structure of Cu(001): Observation of a spin-orbit-gap surface state*. Phys. Rev. B **33** (1986) p. 4373.
- [Wor00] D. WORTMANN; S. HEINZE; G. BIHLMAYER and S. BLÜGEL: *Interpreting STM images of the MnCu/Cu(100) surface alloy*. Phys. Rev. B **62** (2000) p. 2862.
- [Wu88] S. C. WU; S. H. LU; Z. Q. WANG; C. K. C. LOK; J. QUINN; Y. S. LI; D. TIAN and F. JONA: *Cu{001}c(2×2)-Pd: An ordered surface alloy*. Phys. Rev. B **38** (1988) p. 5363.
- [Wu89] S. C. WU; C. K. C. LOK; J. SOKOLOV; J. QUINN; Y. S. LI; D. TIAN and F. JONA: *Surface state and surface resonance at the center of the surface Brillouin zone $\bar{\Gamma}$ of Cu{001}*. Phys. Rev. B **39** (1989) p. 13218.
- [Wut93a] M. WUTTIG; T. FLORES and C. C. KNIGHT: *Structure and growth of Mn on Ni(100)*. Phys. Rev. B **48** (1993) p. 12082.
- [Wut93b] M. WUTTIG; Y. GAUTHIER and S. BLÜGEL: *Magnetically Driven Buckling and Stability of Ordered Surface Alloys: Cu(100)c(2×2)Mn*. Phys. Rev. Lett. **70** (1993) p. 3619.
- [Wut93c] M. WUTTIG; C. C. KNIGHT; T. FLORES and Y. GAUTHIER: *LEED structure determination of two ordered surface alloys: Cu(100)-c(2×2)Mn and Ni(100)-c(2×2)Mn*. Surf. Sci. **292** (1993) p. 189.
- [Wut93d] M. WUTTIG and J. THOMASSEN: *Structure determination for Fe films on Cu(100)*. Surf. Sci. **282** (1993) p. 237.
- [Wut96] M. WUTTIG; S. JUNGHANS; T. FLORES and S. BLÜGEL: *Comment on "Structure of the Mn-induced Cu(100)c(2×2) surface"*. Phys. Rev. B **53** (1996) p. 7551.
- [Xho92] P. XHONNEUX and E. COURTENS: *Direct correlation between the structure and magnetism of thin epitaxial Fe on Cu(100)*. Phys. Rev. B **46** (1992) p. 556.

[Yeh85] J. J. YEH and I. LINDAU: *Atomic subshell photoionization cross section and asymmetry parameters: $1 \leq Z \leq 103$* . At. D. and Nucl. Data Tables **32** (1985) p. 1.

[Zan92] A. ZANGWILL: *Physics at Surfaces* (Cambridge Univ. Press, 1992).

Acknowledgements

Last but not least, I would like to thank all colleagues who have taken part to perform and to refer this work.

An erster Stelle möchte ich Prof. Dr. C. Laubschat für die Betreuung während dieser Doktorarbeit danken, dies gilt besonders, weil während dieser Arbeit keine Seltenerdverbindungen untersucht wurden.

An zweiter Stelle möchte ich mich für die Bereitschaft von Prof. Dr. W.-D. Schneider für eines der Zweitgutachten bedanken.

Igualmente agradezco a Prof. Dr. E. García Michel por su disposición como referee de este trabajo.

Für seine Hilfe und vor allem moralische Unterstützung bei der Bewältigung der alltäglichen Probleme und dem “Aushandeln” von Meßzeiten danke ich Herrn Dr. S. Molodtsov. Weiterhin Dank für die kritische Durchsicht des Manuskripts dieser Arbeit!

I would like to express my appreciations to Dr. S. Halilov for calculating nearly all the systems I was asking for and for answering all my boring questions.

Al doctor Y. Huttel por las medidas de los sistemas de multicapas que hicimos juntos en el L.U.R.E, quedándonos los días y noches. Suerte con tu nuevo trabajo en Madrid.

Quiero también agradecer toda la ayuda profesional prestada por el Dr. J. J. Hinarejos en los tiempos cuando la SCIENTA todavía no funcionaba como debía. Besonders möchte ich noch Herrn Dr. M. Heber danken, insbesondere für seine Hilfe bei der Suche nach allen Rechtschreib- und Grammatikfehlern. Dank gilt auch allen anderen Mitgliedern der Arbeitsgruppe: S. Danzenbächer, S. Wieling, V. Servedio, W. Schneider und M. Finken als auch Frau Richter und Frau Spiller für die Übernahme vieler administrativer Aufgaben. Den Herren Ing. E. Erler und V. Fischer gilt mein Dank für Ihre Hilfe bei der Herstellung und Vorbereitung von Bauteilen, die für den Betrieb der Apparaturen unerlässlich waren.

Weiterer Dank gilt der Arbeitsgruppe von Prof. Dr. H. Eschrig und insbesondere Herrn Dr. M. Richter für die Nutzung der von ihnen entwickelten LCAO und FPLO Programmpakete und das von ihrer Seite entgegengebrachte Interesse.

Furthermore I want to acknowledge the support by all people during my measurements at LURE and BESSY. Muchas gracias a Virginia y Marta, a Nicolás por su buen humor y sus mails, y como no, a los jefes Dr. M. C. Asensio y Dr. J. Ávila por ofrecerme la posibilidad de medir en Orsay. Thanks to Dr. A. Ionov for

his interest and help during my stay at BESSY and here in Dresden. Thanks to all colleagues from the IFF group of the IFW Dresden for the good collaboration during all SCIENTA measurements, above all to Dr. R. Hübel, C. Dürr, and C. Grazioli: Without their help some experiments would not have been possible. Hopefully I did not forget to mention somebody involved in this work, if this is the case, thanks to you too.

Zum Schluß möchte ich noch der Deutschen Forschungsgemeinschaft (Projekt: LA 655/6) und dem DAAD für finanzielle Unterstützung danken.

Technische Universität Dresden

October 2001

Erklärung

Hiermit versichere ich, daß ich die vorliegende Arbeit ohne unzulässige Hilfe Dritter und ohne Benutzung anderer als der angegebenen Hilfsmittel angefertigt habe; die aus fremden Quellen direkt oder indirekt übernommenen Gedanken sind als solche kenntlich gemacht. Die Arbeit wurde bisher weder im Inland noch im Ausland in gleicher oder ähnlicher Form einer anderen Prüfungsbehörde vorgelegt.

Die Dissertation wurde im Institut für Oberflächenphysik und Mikrostrukturphysik unter der wissenschaftlichen Betreuung von Prof. Dr. C. Laubschat angefertigt.

Hiermit erkenne ich die Promotionsordnung vom 20. März 2000 an.

Dresden, 25. Oktober 2001

Frederik Schiller

Curriculum vitae

Name:	Frederik Schiller
Address:	Hauptstr. 100 D-08144 Voigtsgrün
Date and place of birth:	21. October 1971 in Zwickau
Family status:	single
1978-1986	Polytechnische Oberschule Hirschfeld
1986-1990	Spezialschule math.-naturwiss.-techn. Richtung Chemnitz
1990-1991	community service
1991-1997	Study of physics at the TU Dresden
1994-1995	Study abroad at the Universidad Autónoma de Madrid
1996-1997	Diplomarbeit at Instituto de Ciencia de Materiales de Madrid (ICMM-CSIC) and at Laboratoire pour l'Utilisation du Rayonnement Electromagnétique (L.U.R.E.) in Orsay
from 1998	PhD student in the group of Prof. Dr. C. Laubschat at the TU Dresden

Publications

1. F. SCHILLER, B. HERREROS, G. LIFANTE: *Optical characterization of vapor Zn-diffused waveguides in lithium niobate.*, J. Opt. Soc. Am. A **14** (1997), p. 425
2. F. SCHILLER: *The growth of Vanadium and Manganese on Cu(001) studied by Auger- and Photoelectron Diffraction*, Diplomarbeit angefertigt am Institut für Oberflächen- und Mikrostrukturphysik der TU Dresden 1997
3. F. SCHILLER, Y. HUTTEL, J. AVILA, M.C. ASENSIO: *Growth and magnetic properties of copper on Cu(100)c(2×2)-Mn surface alloy.*, Surf. Sci. **433-435** (1999), p. 434
4. Y. HUTTEL, F. SCHILLER, J. AVILA, M.C. ASENSIO: *Electronic and structural properties of Mn/Cu superstructures.*, Phys. Rev. B **61** (2000), p. 4948
5. F. SCHILLER, Y. HUTTEL, S. HALILOV, J. AVILA, M.C. ASENSIO, C. LAUBSCHAT: *Influence of the substrate on the energy position of the 3d-spin-majority band of c(2×2)MnX(001) (X=Cu,Co) surface compounds.*, Proc., 16. International Colloquium on Magnetic Films and Surfaces Natal (Brasil), (2000), p. 136,
6. F. SCHILLER, S. DANZENBÄCHER, C. LAUBSCHAT: *Behaviour of manganese derived 3d-states in c(2×2) and pgg(4×2) Mn/Cu(001)*, Surf. Sci. **482** (2001), p. 442

Congress participations

1. International Vacuum Conference 14, ICC Birmingham (United Kingdom) 1998, talk: Y. HUTTEL, F. SCHILLER, J. AVILA, M.C. ASENSIO: *Surface magnetism and superstructure of Mn c(2×2)/ Cu(100)*
2. DPG Frühjahrstagung 1999 in Münster (Germany), talk: F. SCHILLER, Y. HUTTEL, J.J. HINAREJOS, J. AVILA, M.C. ASENSIO, C. LAUBSCHAT: *Electronic and magnetic properties of the Mn/Cu/c(2×2)Mn/Cu(001) multilayer system*
3. Journées Surfaces et Interfaces, LURE, Paris (France) 1999, poster: Y. HUTTEL, F.SCHILLER, J. AVILA, M.C. ASENSIO: *Structures atomique et électromagnétique de multicouches Mn/Cu/Mn/Cu*

4. 18th European Conference on Surface Science (ECOSS), Vienna (Austria) 1999, talk: S. DANZENBÄCHER, S. MOLODTSOV, F. SCHILLER, K. KOEPERNIK, Y. TOMM, C. LAUBSCHAT: *Electronic structure of low dimensional solids: pristine and Cs intercalated TaSe₂*
5. DPG Frühjahrstagung 2000 in Regensburg (Germany), talk: F. SCHILLER, Y. HUTTEL, S. DANZENBÄCHER, J. AVILA, M.C. ASENSIO, S. HALILOV, C. LAUBSCHAT: *The electronic structure of the $c(2\times 2)MnX/fcc-X(001)$ surface alloys ($X=Cu, Co, Fe$)*
6. DPG Frühjahrstagung 2000 in Regensburg (Germany), talk: S. DANZENBÄCHER, S. MOLODTSOV, F. SCHILLER, K. KOEPERNIK, Y. TOMM, C. LAUBSCHAT: *Elektronische Struktur von reinem und Cs interkaliertem TaSe₂*
7. 16th International Colloquium on Magnetic Films and Surfaces (ICMFS), Natal (Brazil) 2000, poster: F. SCHILLER, Y. HUTTEL, S. HALILOV, J. AVILA, M.C. ASENSIO, C. LAUBSCHAT: *Influence of the substrate on the energy position of the 3d-spin-majority band of $c(2\times 2)MnX(001)$ ($X=Cu, Co$) surface compounds*
8. 19th European Conference on Surface Science (ECOSS), Madrid (Spain), 2000, talk: F. SCHILLER, Y. HUTTEL, S. HALILOV, J. AVILA, M.C. ASENSIO, C. LAUBSCHAT: *Electronic Structure of the $c(2\times 2)MnX/fcc-X$ ($X=Cu, Fe, Co, Ni$) surfaces and Effects to their Fermi Surfaces*
9. American Physical Society (APS) March 2001 Meeting, Seattle (USA), 2001, talk: S.V. HALILOV, F. SCHILLER, C. LAUBSCHAT: *Two-dimensional magnetic $c(2\times 2)$ Mn alloys: surface states and Fermi surface*
10. 20th European Conference on Surface Science (ECOSS), Krakow (Poland), 2001, poster: M. HEBER, F. SCHILLER, S. L. MOLODTSOV, Y. KUCHERENKO, C. LAUBSCHAT: *Surface effects in α - and β -Ce metal*
11. 20th European Conference on Surface Science (ECOSS), Krakow (Poland), 2001, poster: M. HEBER, F. SCHILLER, C. LAUBSCHAT: *Geometric and electronic structure of $Mg(0001)/W(110)$*

Diese Arbeit wurde mit $\text{\LaTeX} 2_{\epsilon}^2$ gesetzt.

² $\text{\LaTeX} 2_{\epsilon}$ ist eine Erweiterung von \LaTeX . \LaTeX ist eine Makropaket für \TeX . \TeX ist eingetragenes Warenzeichen der the American Mathematical Society und als solches gesetzlich geschützt.